AN ABSTRACT OF THE DISSERTATION OF

Aaron J. Fillo for the degree of Doctor of Philosophy in Mechanical Engineering presented on December 16, 2019.

Title: Assessing Mass Diffusion Modeling in Premixed Flames

Abstract approved: _____

Kyle E. Niemeyer

Implementing multicomponent diffusion in numerical combustion studies is computationally expensive due to the challenges involved in computing diffusion coefficients. As a result, mixture-averaged diffusion treatments or simpler methods are used to avoid these costs. However, the accuracy and appropriateness of the mixture-averaged diffusion model has not been verified for three-dimensional turbulent premixed flames. This study evaluates the role of multicomponent mass diffusion for a range of premixed, laminar and turbulent hydrogen, n-heptane, and toluene flames, representing a range of fuel Lewis numbers. Secondary Soret and Dufour effects are neglected to isolate the impact of mass diffusion from thermal diffusion effects. Direct numerical simulation (DNS) of these flames is performed by implementing the Stefan–Maxwell equations in the DNS code NGA. A low-memory, semi-implicit algorithm decreases the computational expense of inverting the full multicomponent ordinary diffusion array while maintaining simulation accuracy and stability. The algorithm is demonstrated to be stable, and verified against one-dimensional premixed hydrogen flames in Cantera. A priori analysis shows significant errors in the diffusion flux vectors for mixture-averaged diffusion in regions of high flame curvature. These errors seem to distort local transport, impacting viscous dissipation and altering global flame statistics such as the normalized turbulent flame speed by modifying the average internal flame structure. In general, these results demonstrate that mixture-averaged diffusion may not fully capture the complexity of full multicomponent diffusion.

Assessing Mass Diffusion Modeling in Premixed Flames

by
Aaron J. Fillo

A DISSERTATION

submitted to

Oregon State University

in partial fulfillment of
the requirements for the
degree of

Doctor of Philosophy

Presented December 16, 2019
Commencement June 2020

Doctor of Philosophy dissertation of Aaron J. Fillo presented on December 16, 2019.

APPROVED:

Major Professor, representing Mechanical Engineering

Head of the School of Mechanical, Industrial, and Manufacturing Engineering

---

Dean of the Graduate School

I understand that my dissertation will become part of the permanent collection of Oregon State University libraries. My signature below authorizes release of my dissertation to any reader upon request.

Aaron J. Fillo, Author

ACKNOWLEDGEMENTS

This material is based upon work supported by the National Science Foundation under Grant Nos. 1314109-DGE and CBET-1761683. This research used resources of the National Energy Research Scientific Computing Center, a DOE Office of Science User Facility supported by the Office of Science of the U.S. Department of Energy under Contract No. DE-AC02-05CH11231, as well as the Extreme Science and Engineering Discovery Environment (XSEDE), which is supported by National Science Foundation grant number ACI-1548562.

I would like to thank Dr. Guillaume Blanquart for openly sharing NGA and for access to his computing cluster HOTH as well as for hosting me as a visiting researcher at The California Institute of Technology, and Dr. Peter Hamlington for providing guidance and direction throughout my program. Dr. Kyle Niemeyer, thank for giving me an opportunity to join the NRG Lab, and for helping to guide me through the trials and tribulations of graduate school.

To my friends and family thank you for being patient with me. I would rather have been with you than working. To my wife Alex, you have been my partner though this challenging process and I cannot thank you enough.

CONTRIBUTION OF AUTHORS

Dr. Jason Schlup is a co-author on the manuscripts presented in Chapters 2 and 3 and assisted with algorithm development, data interpretation, and writing. Guillaume Beardsell is a co-author on the manuscript presented in Chapter 2 and assisted with data interpretation. Dr. Guillaume Blanquart is a co-author on the manuscripts presented in Chapters 2 and 3 and assisted with algorithm development, data interpretation, and writing. Dr. Peter Hamlington is a co-author on the manuscript presented in Chapter 4 and assisted with data interpretation and editing. Dr. Kyle Niemeyer is a co-author on the manuscripts presented in Chapters 2, 3 and 4 and appendices A and B and assisted with data interpretation, writing, and editing.

TABLE OF CONTENTS

TABLE OF CONTENTS (Continued)

Page

LIST OF FIGURES

Figure Page

LIST OF FIGURES (Continued)

Figure Page

LIST OF FIGURES (Continued)

Figure Page

Figure Page

LIST OF TABLES

LIST OF TABLES (Continued)

Table Page

LIST OF APPENDIX FIGURES

Figure Page

LIST OF SYMBOLS

Greek Symbols

α	Mixture thermal diffusivity	m^2/s
$\boldsymbol{\tau}$	Viscous stress tensor	$\mathrm{kg}/(\mathrm{m\,s})$
$\boldsymbol{\Theta}_k$	Residual of the species transport equation at the previous sub-iteration	
Δ	Denotes change	
δ_t	Turbulent flame width	m
$\delta_{i,j}$	Dipole moment	$\mathrm{C\,m}$
$\dot{\omega}$	Species source term	$\mathrm{kg}/(\mathrm{m}^2\,\mathrm{s})$
$\dot{\omega}_T$	Temperature source term	$\mathrm{K\,m/s}$
ϵ	Viscous dissipation rate	
η	Kolmogorov length scale	m
κ	Wavenumber	$\mathrm{rad/m}$
κ'^2	Modified wavenumber	$\mathrm{rad/m}$
μ	Mean value	
∇	Differential	$1/\mathrm{m}$
ν	Kinematic viscosity	m^2/s
ω	Vorticity	$\mathrm{rad/s}$
ϕ	Equivalence ratio	Dimensionless
ρ	Mixture density	kg/m^3

LIST OF SYMBOLS (Continued)

τ	Time scale	s
τ_{eddy}	Eddy turn over time	s
$\tilde{\chi}_T$	Temperature scalar gradient	K/m
$\tilde{\chi}_Y$	Species scalar gradient	1/m

Latin Symbols

$\mathbf{u}_c$	Mixture-averaged correction velocity	m/s
$\mathcal{D}_{ji}$	Binary diffusion coefficient between the ith and jth species	m/s
C	Convection source term	
Diff	Diffusion source term	
I	Identity matrix	Dimensionless
J	Preconditioner matrix	
j	Species mass flux	$\text{kg}/(\text{m}^2\,\text{s})$
Y	Chemical source term	
A	Area	m^2
A_{force}	Turbulent forcing coefficient	1/s
c_p	Constant-pressure specific heat	$\text{J}/(\text{kg}\,\text{K})$
D	Diffusion coefficient	m/s
h	Specific enthalpy	J/kg
L	Spanwise domain length	m
l	Integral length	m
L^1	L^1 error norm	
L^2	L^2 error norm	

LIST OF SYMBOLS (Continued)

L^∞	L^∞ error norm	
p	Hydrodynamic pressure	atm
P_o	Thermodynamic pressure	atm
R	Universal gas constant	J/(kg K)
s	Standard deviation	
S_L	Laminar flame speed	m/s
S_T	Turbulent flame speed	m/s
T	Temperature	K
t	Time	s
T_{ad}	Adiabatic flame temperature	K
u	Velocity	m/s
u'	Turbulent velocity fluctuations at integral scale	m/s
V	Volume	m^3
W	Mixture molecular weight	kg/mol
W_i	Species molar mass	kg/mol
X	Mole fraction	Dimensionless
x	Spatial coordinate	m
Y	Species mass fraction	Dimensionless
Ka	Karlovitz number	Dimensionless
Le	Lewis number	Dimensionless
Re	Reynolds number	Dimensionless
Re_t	Turbulent Reynolds number	Dimensionless

LIST OF SYMBOLS (Continued)

Subscripts

η	Denotes Kolmogorov scale
b	Denotes burnt mixture
F	Denotes flame
u	Denotes unburnt mixture
lam	Denotes laminar flame value
max	Denotes maximum value in vector or matrix
peak	Denotes value at peak fuel consuption rate
ref	Denotes reference value
sub	Denotes sub-iterations

Superscripts

$*$	Denotes evaluation at half time-step
MA	Denotes mixture-averaged diffusion model
MC	Denotes multicomponent diffusion model

Other Notation

$\angle$	Denotes angle between vectors
$\langle\cdot\rangle$	Denotes mean value

For Mom, Kevy, and Kissa...

You have helped me reach this point, through action and in memory. You inspire my love of science and encourage my passion for sharing that love with other.

"*The Guide says there is an art to flying,"... "or rather a knack. The knack lies in learning how to throw yourself at the ground and miss.*"

Douglas Adams

Chapter 1: Introduction

Turbulence is chaotic in nature and spans a tremendous spatial range. In general, turbulent vortices cascade in size starting from large energy-containing structures—which can be as large as planets—down to energy-dissipating structures on the micro-scale or smaller [1, 2]. At these smallest scales, coupled interactions between thermal, molecular, and momentum diffusion dissipate turbulent kinetic energy [1–3]. This dissipation can be reversed in chemically reacting flows such as turbulent flames, where energy released during combustion can generate turbulence through the interaction of chemical reactions and dissipation processes [3]. The complex interaction of turbulence and chemistry couples the conservation of mass, momentum, and energy with the conservation of chemical species at diffusion length scales [3].

Practical combustion devices, such as internal combustion and gas turbine engines, are primarily driven by the turbulent premixed or partially premixed combustion of hydrogen and hydrocarbon-based fuels [4]. These systems often operate at elevated temperatures and pressures, raising significant challenges for experimental studies [5, 6]. For example, practical measurement tools capable of withstanding a combustion environment can be expensive and can introduce significant bias into an experiment [6, 7]. Moreover, while optical measurement techniques can alleviate much of these biases, they require optical access to the flame, which may require fundamentally altering the flow configuration and limit the practical application of these methods [5–7]. Finally, turbulence and chemistry within a flame are sensitive to short time scales, much faster than experimental methods can capture, and as a result practical measurements of combustion processes are inherently average quantities and fail to provide instantaneous measurements with high spatial fidelity [6]. Thus, while experimental studies of combustion can provide valuable insight into combustion physics, they can not sufficiently characterise the complex turbulence-chemistry interactions present in these flows.

Alternatively, direct numerical simulation (DNS) studies turbulent flows by solving the governing equations at a fine-enough resolution to directly simulate turbulence without models [8–10]. DNS is often referred to as a “virtual experiment” and simulates

turbulence at high-fidelity down to the dissipation length scales. As a result, DNS is computationally expensive, requiring thousands of CPU cores running for days to simulate a small spatial domain for a relatively short time. Thus, while it would be computationally cost prohibitive to simulate an entire engine, for example, DNS can be paired with other simulation methods or experiments to investigate a wide range of turbulent phenomena. Moreover, because of its high temporal and spatial resolution, DNS provides a highly resolved reference data and is often used to develop and verify turbulence closure models used in other turbulence modeling approaches such as large-eddy simulation (LES) and Reynolds-averaged Navier–Stokes (RANS) simulation [11–13].

However, the DNS of turbulent combustion suffers from three primary limitations. First, large energy-containing turbulent structures act as a source of turbulent kinetic energy into the system, and these are often too large to be simulated in the DNS of turbulent reacting flows. Capturing the smallest turbulent scales—without incurring prohibitive costs—generally limits DNS of reacting flows to small domains, e.g., on the order of millimeters to centimeters [9]. As a result, these large-scale sources of turbulence must be modeled through turbulence-forcing methods, otherwise dissipation will dominate and damp out turbulence in the domain [14, 15]. Second, due to the high computational expense associated with evaluating finite rate chemistry, DNS of turbulent combustion with detailed chemistry can be computationally cost prohibitive even for small domains [8–10]. Detailed chemical kinetic models can contain tens to hundreds of chemical species, and hundreds to thousands of elementary chemical reactions, resulting in a dense system of differential equations [16, 17]. Thus, to alleviate these high computational costs, reduced chemical kinetic models are often used to approximate detailed chemistry [9]. Third, the presence of numerous chemical species gives rise to multicomponent mass and thermal diffusion, which significantly increases computational complexity [18–21]. As a result of this increased complexity, a range of diffusion approximations are used to reduce the computational expense associated with these diffusion processes [18, 22, 23]. While the turbulent forcing and multicomponent thermal diffusion assumptions have been well characterised for use in the DNS of turbulent combustion, the impact of multicomponent mass diffusion and chemical kinetic model reduction on these simulations is not fully understood [8–10, 16–19, 24].

Another factor relevant to DNS of turbulent reacting flows is the choice of chemical kinetic model, and particularly the impact of using a reduced kinetic model. Though

this topic has only been investigated by one or two studies [25], its analysis is outside the primary scope of this work. Appendix A provides an initial assessment on the impact of reduced chemical models on turbulent combustion.

Multicomponent mass transport is critical to the understanding of combustion physics as the diffusion of mass, heat, and momentum occur in parallel in turbulent reacting flows [20, 26]. Moreover, the coupling of turbulence and chemistry during the combustion processes can locally impact the flame's structure, causing it to curve and forming steep, multi-directional gradients in the temperature and scalar fields [3]. These strong, highly variable gradients can cause large diffusion fluxes, which increase mass transport through the flame front and may further impact flame structure and dynamics [3]. However, implementing full multicomponent mass diffusion transport in DNS can be memory-intensive and computationally expensive. This is because evaluating the diffusion fluxes depends on numerous spatial gradients and requires point-wise knowledge of the multicomponent diffusion coefficient matrix, which scales in size with the number of chemical species squared [20, 27]. While several approximations attempt to reduce the complexity of diffusion modeling, including (in order of increasing complexity) the unity Lewis number, constant non-unity Lewis number [28], and mixture-averaged assumption [20, 23], to my knowledge the accuracy and appropriateness of these assumptions has not been evaluated relative to full multicomponent diffusion transport.

Finally, while efficient multicomponent transport models do exist, namely those developed by Ern and Giovalgigli [29–31] and Ambikasaran and Narayanaswamy [32], they focus primarily on reducing the computational cost of determining the multicomponent diffusion coefficients but do not reduce the large memory requirements associated with evaluating the diffusion fluxes themselves. Motivated by the dearth of affordable computational tools for evaluating full multicomponent mass diffusion, a fast, stable, low-memory algorithm is needed to implement full multicomponent transport in DNS. Moreover, as demonstrated by the lack of available data from simulations using multicomponent transport, a thorough evaluation of the impact of multicomponent transport turbulent combustion is needed to evaluate the accuracy and appropriateness of existing diffusion approximations.

1.1 Motivation

An improved method for implementing multicomponent mass diffusion in DNS for three-dimensional reacting flows is currently needed. This is motivated by the importance of mass diffusion in understanding the fundamental physics and chemistry at the smallest scales of turbulent combustion. These motivations can be summarized as a need to:

- Eliminate assumptions used in DNS,
- Evaluate the limitations of existing diffusion approximations relative to full multi-component mass diffusion, and
- Understand the impact of multicomponent diffusion on the underlying physics of turbulent combustion.

This research has broad implications for the greater combustion community. For DNS to be considered a true "virtual experiment" it should rely on the smallest number of assumptions or approximations as possible. Thus, developing and implementing a model for multicomponent mass diffusion would eliminate the need for long standing diffusion assumptions and enable a more-correct evaluation of the complex physics at play in turbulent combustion. More generally, improved diffusion modeling would enable the development of better closure models for LES and RANS, which do not currently include multicomponent diffusion effects. Finally, low-memory algorithms are not limited to diffusion modeling and could be implemented for a wide range of numerical schemes to improve performance and reduce temporary memory requirements.

1.2 Objectives

The primary objectives of this work are to develop and implement a fast, low-memory, and stable algorithm for implementing multicomponent transport in DNS, and evaluate the accuracy and appropriateness of the existing diffusion approximations relative to full multicomponent mass diffusion. More specifically, this study will focus on these six objectives:

1. Develop and implement a memory-efficient rearrangement of the floating-point operations associated with evaluating multicomponent diffusion in the low Mach number reacting-flow equations.

2. Develop and implement a fast and stable semi-implicit algorithm for implementing multicomponent diffusion in DNS.

3. Demonstrate the accuracy and stability of the proposed semi-implicit algorithm for use in the DNS of premixed, turbulent combustion in the moderate-to-high Karlovitz number regime.

4. Assess the accuracy of the mixture-averaged diffusion approximation relative to multicomponent diffusion for premixed, turbulent combustion in the moderate-to-high Karlovitz number regime.

5. Assess the impact of the mixture-averaged diffusion approximation on the turbulent flame speed and global flame statistics relative to multicomponent diffusion for premixed, turbulent combustion in the moderate-to-high Karlovitz number regime.

6. Assess the impact of mixture-averaged and multicomponent diffusion modeling on the average internal flame structure of premixed, turbulent combustion in the moderate-to-high Karlovitz number regime.

1.3 Outline of Thesis

In this dissertation I present the development and implementation of a fast, low-memory, stable algorithm for modeling multicomponent transport in DNS and assess the impact of multicomponent transport on the complex chemistry and physics present in turbulent combustion. In Chapter 2 I briefly review relevant studies and existing methods for modeling diffusion in DNS. I then present the proposed algorithm for implementing multicomponent diffusion into the DNS code NGA [33, 34], demonstrate the method's performance and accuracy, and comprehensively assess its computational costs. In Chapter 3 I assess the accuracy of mixture-averaged diffusion fluxes relative to full multicomponent mass diffusion in unsteady laminar and turbulent flames of three fuels, and evaluate the impact of that error on global flame statistics. In Chapter 4 I assess the impact of diffusion modeling on the turbulent transport and flame structure to better understand the underlying physics present in turbulent combustion.

Finally, in Chapter 5 I present general conclusions for this work, and discuss their context within the reviewed literature. To help provide further insight on the relative accuracy of existing DNS assumptions, in Appendix A I present a preliminary assessment of the impact of chemical kinetic model reduction on the relative accuracy of DNS for premixed turbulent flames. In addition, in Appendix B I present LIB-LAB: The Library Laboratory, an educational video series focused on communicating academic research to a K-12 audience using evidence-based teaching practices. While Appendices A and B fall outside the primary scope of this dissertation, they are relevant to the continued improvement of DNS tools and broad communication of this work.

A fast, low-memory, and stable algorithm for implementing multicomponent transport in direct numerical simulations

Aaron J. Fillo, Jason Schlup, Guillaume Beardsell, Guillaume Blanquart, and Kyle E. Niemeyer

Journal of Computational Physics
In print, 2019.
https://doi.org/10.1016/j.jcp.2019.109185

Chapter 2: A fast, low-memory, and stable algorithm for implementing multicomponent transport in direct numerical simulations

Implementing multicomponent diffusion models in reacting-flow simulations is computationally expensive due to the challenges involved in calculating diffusion coefficients. Instead, mixture-averaged diffusion treatments are typically used to avoid these costs. However, to our knowledge, the accuracy and appropriateness of the mixture-averaged diffusion models has not been verified for three-dimensional turbulent premixed flames. In this study we propose a fast, efficient, low-memory algorithm and use that to evaluate the role of multicomponent mass diffusion in reacting-flow simulations. Direct numerical simulation of these flames is performed by implementing the Stefan–Maxwell equations in NGA. A semi-implicit algorithm decreases the computational expense of inverting the full multicomponent ordinary diffusion array while maintaining accuracy and fidelity. We first verify the method by performing one-dimensional simulations of premixed hydrogen flames and compare with matching cases in Cantera. We demonstrate the algorithm to be stable, and its performance scales approximately with the number of species squared. Then, as an initial study of multicomponent diffusion, we simulate premixed, three-dimensional turbulent hydrogen flames, neglecting secondary Soret and Dufour effects. Simulation conditions are carefully selected to match previously published results and ensure valid comparison. Our results show that using the mixture-averaged diffusion assumption leads to a 15 % under-prediction of the normalized turbulent flame speed for a premixed hydrogen-air flame. This difference in the turbulent flame speed motivates further study into using the mixture-averaged diffusion assumption for DNS of moderate-to-high Karlovitz number flames.

Keywords: Turbulent flames; Direct numerical simulation; Multicomponent diffusion; Mixture-averaged diffusion

2.1 Introduction

Implementing full multicomponent mass diffusion transport in direct numerical simulation (DNS) can be memory intensive and computationally expensive. This is because calculating diffusion fluxes requires point-wise knowledge of the multicomponent diffusion coefficient matrix, which scales with the number of chemical species squared [20]. The unity Lewis number, non-unity Lewis number, and mixture-averaged diffusion assumptions have been used to reduce the costs associated with mass diffusion by approximating the full diffusion coefficient matrix as a constant scalar value, a constant vector, and a matrix diagonal, respectively. In addition, several approaches further reduce the system's complexity by approximating multicomponent diffusion processes in terms of equivalent Fickian processes, such as those used by Warnatz [35] and Coltrin et al. [36]. However, to our knowledge, the accuracy and appropriateness of these assumptions have not been evaluated in turbulent reacting flows against multicomponent diffusion transport due to its high computational expense and a dearth of affordable computing tools.

As further motivation for this study, Lapointe and Blanquart [22] recently investigated the impact of differential diffusion on simulations using unity and nonunity Lewis number approximations. They reported that methane, n-heptane, iso-octane, and toluene flames have similar normalized turbulent flame speeds and fuel burning rates when neglecting differential diffusion, but flames using the nonunity Lewis number approximation underpredict the normalized flame speed when including differential diffusion due to reduced burning rates [22]. Building on these results, Burali et al. [23] evaluated the relative accuracy of the nonunity Lewis number assumption relative to mixture-averaged diffusion for lean, unstable hydrogen/air flames; lean, turbulent n-heptane/air flames; and ethylene/air coflow diffusion flames. They demonstrated that the relative error associated with the nonunity Lewis number assumption could be minimized with careful selection of the Lewis number vector for a wide range of flames [23]. Similarly, Schlup and Blanquart [18] examined the impact of multicomponent thermal diffusion on DNS of turbulent, premixed, high-Karlovitz hydrogen/air flames. They showed that simulations using the mixture-averaged thermal diffusion assumption underpredict the normalized flame speeds compared with results from simulations using full multicomponent thermal diffusion. In addition, including multicomponent thermal diffusion results in increased production of chemical source terms in regions of high positive curvature [18]. These

observed discrepancies in similar flame simulations with different diffusion models warrant a detailed investigation of the fundamental transport phenomena involved.

While data are sparse from three-dimensional reacting-flow simulations with multicomponent transport, several groups have investigated the effects of multicomponent transport in simpler configurations. These studies include one-dimensional [31, 37–41] and two-dimensional flames [19, 42, 43] at various unburnt conditions. These works compared the multicomponent model with various levels of diffusion and transport property models, from constant Lewis number to mixture-averaged properties. In general, prior studies found some errors between multicomponent and mixture-averaged formulations for simplified hydrogen/air and methane/air flame configurations, such as unstretched laminar flames. However, these studies did not assess flames where diffusion effects may be more important, such as two- and three-dimensional, unsteady laminar and turbulent flames. Moreover, advancing clean and efficient combustion technology requires incorporating realistic fuel chemistry in large-scale turbulent simulations relevant to practical applications. Thus, there is a clear need for a computationally efficient algorithm capable of modeling full multicomponent diffusion transport [44].

The studies by Lapointe and Blanquart [22], Burali et al. [23], and Schlup and Blanquart [18] each took care to isolate the diffusion assumptions in question by neglecting higher-order terms that may affect diffusion transport. For example, with the exception of Schlup and Blanquart [18], these studies neglected Soret and Dufour diffusion, as it would be difficult to determine the direct cause of an observed effect when including both molecular and thermal diffusion. However, despite this methodical approach, the results of these studies were presented with reference to mixture-averaged diffusion, rather than full multicomponent diffusion. This further highlights the need for a computationally efficient method for implementing full multicomponent transport, and a subsequent examination of the differences between its "true" results and those resulting from the approximations conventionally used.

In this direction, several studies have examined the impact of full multicomponent transport on simplified three-dimensional flame configurations. Giovangigli [19] demonstrated that multicomponent Soret effects significantly impact a wide range of laminar hydrogen/air flames. Specifically, they noted that multicomponent Soret effects influence laminar flame speeds and extinction stretch rates for flat and strained premixed flames, respectively. For high-pressure systems, Borchesi and Bellan [45] developed and analyzed

a multi-species turbulent mixing model for large-eddy simulations. They focused on turbulent crossflow mixing of a five-species combustion-relevant mixture of n-heptane, O_2, CO_2, N_2, and H_2O. The multi-species transport model significantly improves the accuracy and fidelity of the solution throughout the mixing layer; however, this study only considered non-reacting flows and, as a result, did not assess the impact of multicomponent transport on the chemistry inherent in turbulent combustion. In addition, these simulations implement a simplified diffusion model to approximate multicomponent diffusion but do not directly solve the diffusion terms present in the generalized conservation equations for species and energy [46].

Motivated by the dearth of affordable three-dimensional multicomponent transport models, Ern and Giovangigli [29–31] developed the computationally efficient Fortran library EGLIB for accurately determining transport coefficients in gas mixtures. More recently, Ambikasaran and Narayanaswamy [32] proposed an efficient algorithm to compute multicomponent diffusion velocities, which scales linearly with the number of species. This significantly reduces computational cost compared with previous methods that directly invert the Stephan–Maxwell equations and thus scale with the number of species cubed. Although both libraries reduce the computational cost of determining the multicomponent diffusion coefficients, they do not provide a method for reducing the resulting large memory requirements for multidimensional simulations.

Overall, these prior studies provide compelling evidence that multicomponent transport is important and can affect the accuracy of combustion models. However, none assessed how multicomponent transport impacts three-dimensional turbulent systems with detailed chemistry. In this article, we demonstrate and analyze an efficient, dynamic algorithm that reduces the computational expense of calculating the multicomponent diffusion fluxes. We demonstrate the approach is accurate and stable for a wide range of time-step sizes. In addition, we present a comprehensive assessment of the numerical costs associated with this method. To verify the proposed algorithm we present one-dimensional freely propagating, laminar hydrogen/air flames and compare with results from Cantera. Finally, we simulate three-dimensional, turbulent, premixed, hydrogen/air flames. As a preliminary comparison of the mixture-averaged and multicomponent diffusion models, we perform an a posteriori assessment of how the choice of diffusion model impacts the turbulent statistics of the three-dimensional hydrogen simulation.

2.2 Governing equations

This section presents the low-Mach number reacting Navier–Stokes equations used in this study. In addition, this section outlines the method used to determine the mass diffusion fluxes for both the mixture-averaged and multicomponent approaches, abbreviated here as MA and MC, respectively.

2.2.1 Low Mach-number equations

In this work we solve the variable-density, low-Mach number, reacting-flow equations [33, 34]. The conservation equations are

$$\frac{\partial \rho}{\partial t} + \nabla \cdot (\rho \mathbf{u}) = 0 \,, \tag{2.1}$$

$$\frac{\partial \rho \mathbf{u}}{\partial t} + \nabla \cdot (\rho \mathbf{u} \otimes \mathbf{u}) = -\nabla p + \nabla \cdot \boldsymbol{\tau} \,, \tag{2.2}$$

$$\frac{\partial \rho T}{\partial t} + \nabla \cdot (\rho \mathbf{u} T) = \nabla \cdot (\rho \alpha \nabla T) + \rho \dot{\omega}_T - \frac{1}{c_p} \sum_i c_{p,i} \mathbf{j}_i \cdot \nabla T + \frac{\rho \alpha}{c_p} \nabla c_p \cdot \nabla T \,, \tag{2.3}$$

$$\frac{\partial \rho Y_i}{\partial t} + \nabla \cdot (\rho \mathbf{u} Y_i) = -\nabla \cdot \mathbf{j}_i + \dot{\omega}_i \,, \tag{2.4}$$

where ρ is the mixture density, $\mathbf{u}$ is the velocity vector, p is the hydrodynamic pressure, $\boldsymbol{\tau}$ is the viscous stress tensor, T is the temperature, α is the mixture thermal diffusivity, $c_{p,i}$ is the constant-pressure specific heat of species i, c_p is the constant-pressure specific heat of the mixture, $\mathbf{j}_i$ is the diffusion flux of species i, Y_i is the mass fraction of species i, and $\dot{\omega}_i$ is the production rate of species i. In Equation (2.3), the temperature source term $\dot{\omega}_T$ is given by

$$\dot{\omega}_T = -c_p^{-1} \sum_i h_i(T) \dot{\omega}_i \,, \tag{2.5}$$

where $h_i(T)$ is the specific enthalpy of species i as a function of temperature. The density is determined from the ideal gas equation of state

$$\rho = \frac{P_o W}{RT} \,, \tag{2.6}$$

where P_o is the thermodynamic pressure, R is the universal gas constant, and W is the mixture molecular weight determined via $W = \left(\sum_i^N Y_i / W_i \right)^{-1}$, where W_i is the molar

mass of the ith species and N is the number of species.

The diffusion fluxes are calculated with either the mixture-averaged [20] or multi-component [27] models, which are both based on Boltzmann's equation for the kinetic theory of gases [27, 47]. The baro-diffusion term is commonly neglected in reacting-flow simulations under the low Mach-number approximation [48]. We have also neglected thermal diffusion because our objective in this work is to investigate the impact of mass diffusion models; Schlup and Blanquart [18, 49] previously explored the effects of thermal diffusion modeling.

2.2.2 Mixture-averaged (MA) species diffusion flux

The ith species diffusion flux for the mixture-averaged diffusion model is related to the species gradients by a Fickian formulation and is expressed as

$$\mathbf{j}_i = -\rho D_{i,m} \frac{Y_i}{X_i} \nabla X_i + \rho Y_i \mathbf{u}_c' \,, \tag{2.7}$$

where X_i is the ith species mole fraction, $D_{i,m}$ is the ith species mixture-averaged diffusion coefficient as expressed by Bird et al. [20]:

$$D_{i,m} = \frac{1 - Y_i}{\sum_{j \neq i} X_j / \mathcal{D}_{ji}} \,, \tag{2.8}$$

where $\mathcal{D}_{ji}$ is the binary diffusion coefficient between the ith and jth species. Finally, $\mathbf{u}_c'$ is the correction velocity used to ensure mass continuity:

$$\mathbf{u}_c' = \sum_{i=1}^{N} D_{i,m} \frac{Y_i}{X_i} \nabla X_i \,. \tag{2.9}$$

The expression for species diffusion flux can be re-stated in terms of mass fraction Y_i as

$$\mathbf{j}_i = -\rho D_{i,m} \left(\nabla Y_i - Y_i \sum_{k=1}^{N} \nabla Y_k \frac{W}{W_k} \right) + \rho Y_i \mathbf{u}_c' \,, \tag{2.10}$$

where $D_{i,m}$ corresponds to the ith element of the diagonal mixture-averaged diffusion coefficient matrix, defined herein as $\boldsymbol{D}^{\mathrm{MA}}$.

2.2.3 Multicomponent (MC) species diffusion flux

The multicomponent diffusion model for the ith species diffusion flux is

$$\mathbf{j}_i = \frac{\rho Y_i}{X_i W} \sum_{k=1}^{N} W_k D_{ik} \nabla X_k \,, \tag{2.11}$$

where D_{ik} is the ordinary multicomponent diffusion coefficient (computed using the `MCMDIF` subroutine of CHEMKIN II [50] with the method outlined by Dixon–Lewis [21]). Equation (2.11) can be restated in terms of mass fraction as

$$\mathbf{j}_i = \rho \sum_{k} -D_{ik}^{\mathrm{MC}} \nabla Y_k \,, \tag{2.12}$$

where

$$D_{ik}^{\mathrm{MC}} = -\frac{W_i}{W} \left[D_{ik} - \frac{W}{W_k} \left(\sum_j D_{ij} Y_j \right) \right] \,. \tag{2.13}$$

The diagonal of the ordinary multicomponent diffusion matrix, D_{ii}, is zero. As will be shown later, the $\boldsymbol{D}^{\mathrm{MC}}$ matrix is singular with a kernel of dimension one. Interestingly, the vector of species mass fractions is in the kernel:

$$\sum_{k=1}^{N} D_{ik}^{\mathrm{MC}} Y_k = -\frac{W_i}{W} \left[\left(\sum_k D_{ik} Y_k \right) - \left(W \sum_k \frac{Y_k}{W_k} \right) \left(\sum_j D_{ij} Y_j \right) \right] = 0 \,. \tag{2.14}$$

This property will be important later (in Section 2.3.4) for the stability analysis.

The multicomponent diffusion coefficients, thermal conductivities, and thermal diffusion coefficients are computed by solving a system of equations defined by the L matrix, composed of nine sub-matrices:

$$\begin{bmatrix} \mathbf{L}^{00,00} & \mathbf{L}^{00,10} & 0 \\ \mathbf{L}^{10,00} & \mathbf{L}^{10,10} & \mathbf{L}^{10,01} \\ 0 & \mathbf{L}^{01,10} & \mathbf{L}^{01,01} \end{bmatrix} \begin{bmatrix} \mathbf{a}_1^{00} \\ \mathbf{a}_1^{10} \\ \mathbf{a}_1^{01} \end{bmatrix} = \begin{bmatrix} 0 \\ \mathbf{X} \\ \mathbf{X} \end{bmatrix} \,, \tag{2.15}$$

where the right-hand side is composed of the one-dimensional mole fraction arrays $\mathbf{X}$. Based on this system of equations, the inverse of the $\mathbf{L}^{00,00}$ block provides the multicom-

ponent diffusion coefficients:

$$D_{ij} = X_i \frac{16T}{25P} \frac{W}{W_j} (q_{ij} - q_{ii}) \ , \tag{2.16}$$

where

$$\mathbf{q} = \left(\mathbf{L}^{00,00} \right)^{-1} \ . \tag{2.17}$$

The $\mathbf{L}^{00,00}$ sub-matrix block is given by

$$L_{ij}^{00,00} = \frac{16T}{25P} \sum_{k=1}^{N} \frac{X_k}{W_i \mathcal{D}_{ik}} \left\{ W_j X_j (1 - \delta_{i,k}) - W_i X_i (\delta_{i,j} - \delta_{j,k}) \right\} \ , \tag{2.18}$$

where $\delta_{i,j}$ is the reduced dipole moment corresponding to the ith component of the vector of dipole moments.

2.3 Methods

As discussed previously, multicomponent mass diffusion has not yet been incorporated into three-dimensional turbulent flame simulations due to its high computational expense. This section presents the discretized equations, numerical algorithm, and preconditioner proposed. The method is based on the semi-implicit time-marching scheme for species mass-fraction fields proposed by Savard et al. [34].

2.3.1 Multicomponent model implementation

This work was completed using the structured, multi-physics, and multi-scale finite-difference code NGA [33, 34]. NGA can solve a wide range of problems, including laminar and turbulent flows [51–53], constant- and variable-density flows [15, 33, 54], large-eddy simulation [52, 55], and DNS [15, 54, 56]. NGA discretely conserves mass, momentum, and kinetic energy with an arbitrarily high-order spatial accuracy [33].

NGA's variable-density flow solver uses both spatially and temporally staggered variables, storing all scalar quantities (ρ, P, T, Y_i) at the volume centers and velocity components at their respective volume faces [33, 57]. The convective term in the species transport equation is discretized using the bounded, quadratic, upwind-biased, interpola-

tive convective scheme (BQUICK) [58]. The diffusion source term is discretized using a second-order centered scheme and the variables are advanced in time using a second-order semi-implicit Crank–Nicolson scheme [59].

An iterative procedure is applied to fully cover the nonlinearities in the Navier–Stokes equations and the species diffusion terms. Prior studies demonstrated this iterative process to be critically important for stability and accuracy [33, 34, 59, 60]. Savard et al. [34] fully detailed the numerical algorithm sequence; we summarize this method here. This summary is independent of the preconditioning strategy employed in NGA, to which propose modifications in Section 2.3.2.

The algorithm for advancing one time step follows, using a uniform time-step size Δt. The density, pressure, and scalar fields are advanced from time level $t^{n+1/2}$ to $t^{n+3/2}$, and the velocity fields are advanced from time t^n to t^{n+1}, where t^n is the current time. Each iteration (i.e., time step) consists of Q sub-iterations and follows this procedure:

0. Upon convergence of the previous time step, the algorithm stores the density ($\rho^{n+1/2}$), pressure ($P^{n+1/2}$), velocity fields ($\mathbf{u}^n$), and scalar fields ($\mathbf{Y}^{n+1/2}$), where $\mathbf{Y}$ represents the vector of species mass fractions $(Y_1, \ldots, Y_N)$. The solutions for pressure, species mass fraction, and momentum from the previous time step are used as an initial guess for the iterative procedure:

$$P_0^{n+3/2} = P^{n+1/2} \ , \ \mathbf{Y}_0^{n+3/2} = \mathbf{Y}^{n+1/2} \ , \text{ and } \ (\rho\mathbf{u})_0^{n+1} = (\rho\mathbf{u})^n \ . \tag{2.19}$$

An Adams–Bashforth prediction evaluates the initial density:

$$\rho_0^{n+3/2} = 2\rho^{n+1/2} - \rho^{n-1/2} \ , \tag{2.20}$$

which ensures that the continuity equation is discretely satisfied at the beginning of the iterative procedure.

1. For the sub-iterations $k = 1, \ldots, Q$, the semi-implicit Crank–Nicolson method advances the scalar fields in time [33, 59]:

$$\begin{aligned} \rho_k^{n+3/2}\mathbf{Y}_{k+1}^{n+3/2} &= \rho^{n+1/2}\mathbf{Y}^{n+1/2} + \Delta t\left(\mathbf{C}_k^* + \mathbf{Diff}_k^* + \mathbf{\Omega}_k^*\right) \\ &+ \frac{\Delta t}{2}\left(\frac{\partial \mathbf{C}}{\partial \mathbf{Y}} + \frac{\partial \mathbf{Diff}}{\partial \mathbf{Y}} + \frac{\partial \mathbf{\Omega}}{\partial \mathbf{Y}}\right)_k^{n+1} \cdot \left(\mathbf{Y}_{k+1}^{n+3/2} - \mathbf{Y}_k^{n+3/2}\right) \ , \end{aligned} \tag{2.21}$$

where $\mathbf{Diff} = -\nabla \cdot \mathbf{j}_i$ and $\mathbf{Y}_k^*$, $\mathbf{C}_k^*$, $\mathbf{Diff}_k^*$, and $\mathbf{\Omega}_k^*$ are the mass fraction, convection, diffusion, and chemical terms evaluated on the mid-point (or half time-step) scalar field Y_k^*:

$$\mathbf{Y}_k^* = \frac{\mathbf{Y}^{n+1/2} + \mathbf{Y}_k^{n+3/2}}{2} \, . \tag{2.22}$$

To simplify the discrete notations for spatial differentiation, the operators corresponding to the convective and diffusive terms in Equation (2.4) are written as $\mathbf{C}$ and $\mathbf{Diff}$, respectively [34]. $\frac{\partial \mathbf{C}}{\partial \mathbf{Y}}$ and $\frac{\partial \mathbf{Diff}}{\partial \mathbf{Y}}$ are the Jacobian matrices corresponding to the convective and diffusive terms with respect to the species mass fractions, respectively. $\mathbf{C}$ and $\frac{\partial \mathbf{C}}{\partial \mathbf{Y}}$ are functions of the density and velocity, while $\mathbf{Diff}$ and $\frac{\partial \mathbf{Diff}}{\partial \mathbf{Y}}$ are functions of the density, diffusivity, and molar weight. They are consistently updated at each sub-iteration [34].

2. The density field, $\rho_{k+1}^{n+3/2}$, is evaluated from the new scalar fields using Equation (2.6). We do not rescale the scalar fields as proposed by Shunn et al. [60]. However, upon convergence of the sub-iterations, this method is equivalent to the density treatment they proposed [34].

3. The momentum equation is advanced in time using a similar semi-implicit Crank–Nicolson method for the scalar fields as described by Savard et al. [34].

4. A Poisson equation is then solved for the fluctuating hydrodynamic pressure using a combination of HYPRE [33, 61], BICGSTAB[62], and/or FFTW [63]. The predicted velocity field is then updated.

5. Upon convergence of the sub-iterations, the solutions are updated.

The procedure summarized above becomes equivalent to the fully implicit Crank–Nicolson time-integration scheme upon convergence of the sub-iterations [59].

2.3.2 Preconditioning

We expand the above numerical procedure to incorporate multicomponent diffusion by modifying the time-marching step for species mass fraction fields. Specifically, this method modifies the treatment of the mass-diffusion source term in the species mass fraction fields. All other intermediate steps are unchanged.

2.3.2.1 Preconditioning iterative method

For simpler implementation, Equation (2.21) is solved in its residual form:

$$\begin{aligned}&\left[\rho_k^{n+3/2}\mathbf{I}-\frac{\Delta t}{2}\left(\frac{\partial \mathbf{C}}{\partial \mathbf{Y}}+\frac{\partial \mathbf{Diff}}{\partial \mathbf{Y}}+\frac{\partial \mathbf{\Omega}}{\partial \mathbf{Y}}\right)_k^{n+1}\right]\cdot\left(\mathbf{Y}_{k+1}^{n+3/2}-\mathbf{Y}_k^{n+3/2}\right)\\&=\rho^{n+1/2}\mathbf{Y}^{n+1/2}-\rho_k^{n+3/2}\mathbf{Y}_k^{n+3/2}+\Delta t\left(\mathbf{C}_k^{n+1}+\mathbf{Diff}_k^{n+1}+\mathbf{\Omega}_k^{*}\right)\ .\end{aligned}\tag{2.23}$$

This equation can be restated as

$$\mathbf{Y}_{k+1}^{n+3/2}=\mathbf{Y}_k^{n+3/2}-\Delta t\mathbf{J}^{-1}\cdot\Theta_k\ ,\tag{2.24}$$

where the matrix $\mathbf{J}$ is

$$\mathbf{J}=\rho_k^{n+3/2}\mathbf{I}-\frac{\Delta t}{2}\left(\frac{\partial \mathbf{C}}{\partial \mathbf{Y}}+\frac{\partial \mathbf{Diff}}{\partial \mathbf{Y}}+\frac{\partial \mathbf{\Omega}}{\partial \mathbf{Y}}\right)_k^{n+1}\tag{2.25}$$

and the vector

$$\mathbf{\Theta}_k=\frac{\rho_k^{n+3/2}\mathbf{Y}_k^{n+3/2}-\rho^{n+1/2}\mathbf{Y}^{n+1/2}}{\Delta t}-\left[\mathbf{C}_k^{n+1}+\mathbf{Diff}_k^{n+1}+\mathbf{\Omega}_k^{*}\right]\tag{2.26}$$

is the residual of the species transport equation at the previous sub-iteration, which asymptotes to zero as the sub-iterations fully converge.

Written in its residual form, the time advancement of the species transport equations described here resembles the standard preconditioned Richardson-type iterative method [34, 64], where the matrix $\mathbf{J}$ acts as a preconditioner. The choice of $\mathbf{J}$ as a preconditioner is arbitrary and only affects the convergence characteristics of the iterative method [34]. For example,

$$\mathbf{J}=\rho_k^{n+3/2}\mathbf{I}\tag{2.27}$$

is equivalent to the fully explicit integration of the convective, diffusive, and chemical source terms in the species transport equations. Alternatively,

$$\mathbf{J}=\rho_k^{n+3/2}\mathbf{I}-\frac{\Delta t}{2}\left(\frac{\partial \mathbf{C}}{\partial \mathbf{Y}}+\frac{\partial \mathbf{Diff}}{\partial \mathbf{Y}}+\frac{\partial \mathbf{\Omega}}{\partial \mathbf{Y}}\right)_k^{n+1}\tag{2.28}$$

is equivalent to fully implicit integration of the convective, diffusive, and chemical source

terms [34].

There is a clear tradeoff in selecting the preconditioner. Since preconditioning is applied to each step of the iterative methods, the form of matrix **J** should be optimized for low computational and inversion cost while maintaining strong convergence. The fully explicit preconditioner provides the cheapest option but in our experience results in poor convergence performance, requiring extremely small time steps. Alternatively, the fully implicit preconditioner would provide excellent convergence criteria and unconditional stability; however, the Jacobian matrices for the chemical and diffusion source terms are typically dense [20, 50, 65]. Thus, constructing a fully implicit preconditioner is prohibitively expensive for large kinetic models.

To achieve strong convergence while maintaining a low-cost form for the preconditioner, we propose an approximation of the diffusion Jacobian that lies between the fully implicit and fully explicit extremes: a semi-implicit preconditioner. Savard et al. [34] previously implemented a similar approach for preconditioning the chemical Jacobian.

2.3.2.2 Semi-implicit preconditioner

In Equation (2.28), the Jacobian of the diffusion source term depends on the multicomponent diffusion flux, which is proportional to the multicomponent diffusion coefficient matrix, $\boldsymbol{D}^{\mathrm{MC}}$. However, $\boldsymbol{D}^{\mathrm{MC}}$ is a dense matrix and would be a computationally expensive approximation for the Jacobian. Alternatively, the mixture-averaged diffusion coefficient matrix, $\boldsymbol{D}^{\mathrm{MA}}$, is a simplified approximation of $\boldsymbol{D}^{\mathrm{MC}}$ and thus may provide a reasonable, low-cost approximation of the fully implicit Jacobian.

The mixture-averaged diffusion coefficient matrix, $\boldsymbol{D}^{\mathrm{MA}}$, and the multicomponent diffusion coefficient matrix, $\boldsymbol{D}^{\mathrm{MC}}$, are of a similar order and depend on the underlying species diffusivities. In addition, since $\boldsymbol{D}^{\mathrm{MA}}$ is computed from the local species and temperature values rather than global changes, it is inexpensive to compute. Finally, since $\boldsymbol{D}^{\mathrm{MA}}$ is strictly diagonal and thus inexpensive to invert, it provides a low-cost approximation to the diffusion Jacobian. In practice the approximate diffusion Jacobian is a tri-diagonal block matrix, where each block is the diagonal $\boldsymbol{D}^{\mathrm{MA}}$ matrix. In other words, for each species the part of the Jacobian corresponding to that species is tri-diagonal and described by $\boldsymbol{D}^{\mathrm{MA}}$.

2.3.3 Dynamic memory algorithm

As mentioned previously, high-fidelity simulations with full multicomponent mass diffusion will have a high computational expense. Thus, to facilitate a cost-effective implementation of full multicomponent diffusion we propose a simple dynamic memory algorithm that significantly reduces the computational resources needed for such simulations.

The cost of simulating full multicomponent diffusion comes from evaluating the $\boldsymbol{D}^{\mathrm{MC}}$ matrix. Thus, we can reduce computational cost significantly by limiting the evaluation of $\boldsymbol{D}^{\mathrm{MC}}$ to strictly once per grid-point. (In contrast, a naive implementation would involve repeated and redundant evaluations when calculating the species diffusion flux vector and its gradient.) This is possible because the central-difference scheme used is linear and thus additive and commutative by nature. In other words, the terms in the discretized equation are simply added together, and thus are strictly independent of each other and require no information from the surrounding grid points.

Recognizing this, it follows that the order of addition does not matter so long as all of the appropriate terms are included in the discretization. Thus, we can calculate the $\boldsymbol{D}^{\mathrm{MC}}$ matrix once per grid point, and calculate and store for each species the discrete terms of the discretized scalar field corresponding only to the information available at that grid point. The process then repeats at the next grid point and fills in the remaining information. This approach is simply a memory-efficient rearrangement of the floating-point operations and does not alter the final result. Moreover, this dynamic memory scheme avoids the need to calculate local gradients at each grid point.

In practice, we calculate and store the portions of the enthalpy and species-diffusion source terms (in Equations (2.3) and (2.4), respectively) that can be computed from the information available at the ith grid-point for the $(i-1/2)$ and $(i+1/2)$ flux vectors. For example, the discretized form of the diffusion source term is

$$\begin{aligned}\mathbf{Diff}_i = -\nabla \cdot j_i &= \frac{-j_{i+1/2} + j_{i-1/2}}{\Delta x} \\ &= \Bigg[\left(\rho_i D_i + \rho_{i+1} D_{i+1}\right) \frac{Y_{i+1} - Y_i}{\Delta x} \\ &\quad - \left(\rho_{i-1} D_{i-1} + \rho_i D_i\right) \frac{Y_i - Y_{i-1}}{\Delta x} \Bigg] \frac{1}{2\Delta x^2} \,, \end{aligned} \tag{2.29}$$

where the diffusion source term contributions from the $i-1$, i, and $i+1$ grid points are

$$\text{Source}_{i-1} = \frac{\rho_{i-1} D_{i-1}}{2\Delta x^2} \left(Y_i - Y_{1-i}\right) \ , \tag{2.30}$$

$$\text{Source}_{i} = \frac{\rho_{i} D_{i}}{2\Delta x^2} \left(Y_{i+1} + Y_{i-1} - 2Y_i\right) \ , \text{ and} \tag{2.31}$$

$$\text{Source}_{i+1} = \frac{\rho_{i+1}}{D}_{i+1} 2\Delta x^2 \left(Y_{i+1} - Y_i\right) \ , \tag{2.32}$$

respectively.

At the ith grid point, information on the diffusion coefficients at the $i-1$ and $i+1$ grid points is not available; thus, only the diffusion coefficients for the ith grid point can be stored. However, by recognizing that D_i at the ith grid point is equal to D_{i+1} and D_{i-1} at the $i-1$ and $i+1$ grid points, respectively, it is possible to solve Equation (2.30), Equation (2.31), and Equation (2.32) for the $i+1$, i, and $i-1$ grid points, and store them in their respective memory locations. At the next grid point $(i+1)$ the process repeats and the remaining information for the ith grid point is calculated and added to the previously stored partial solution, thus completing the information needed at the ith grid point. Figure 2.1 summarizes this process; fluxes are located at cell faces while source terms are at cell centers.

This approach reduces the number of $\boldsymbol{D}^{\text{MC}}$ evaluations from once per species per grid point to strictly once per grid point. Finally, it reduces temporary memory requirements from an array sized $n_x \times n_y \times n_z \times N^2$ to a 1×7 array corresponding to only the information needed at the current grid point (i, j, k) and its six surrounding points, where n_x, n_y, and n_z are the numbers of grid points in the x, y, and z directions. This optimizes performance by reducing cache calls for both the species mass fractions and species diffusion coefficients.

The algorithm is most efficient for a structured grid, but the proposed method is easily extendable to finite-volume discretizations on unstructured meshes with scalars located at the cell centers. In such schemes, the diffusion term is written as the sum of fluxes on each cell surface. In turn, these fluxes are written as differences of cell-averaged scalar values. The regrouping of the contributions of the diffusion term to each cell in Equations (2.30)–(2.32) would follow a similar approach.

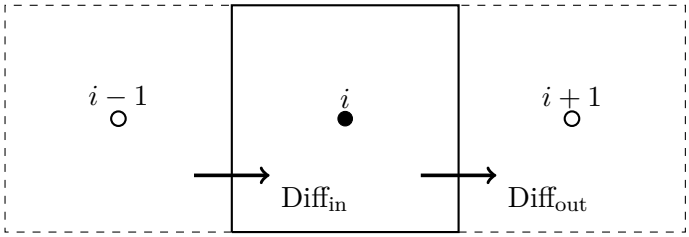

for *i=1:X* **do**
  Calculate diffusion coefficient matrix;
  for *isc=1:N* **do**
    $\text{Flux}(i-1/2)$ += $\text{Diff}_{\text{in},isc}$;
    $\text{Flux}(i+1/2)$ += $\text{Diff}_{\text{out},isc}$;
  end
  $\text{Source}(i)$ += influence from $\text{Diff}(i-1/2)$ and $\text{Diff}(i+1/2)$;
  $\text{Source}(i-1)$ += influence from $\text{Diff}(i-1/2)$;
  $\text{Source}(i+1)$ += influence from $\text{Diff}(i+1/2)$;
end

Figure 2.1: Dynamic algorithm for calculating multicomponent enthalpy and species diffusion source terms. Fluxes are located at cell faces while source terms are at cell centers. N is the number of species.

2.3.4 Method stability

To evaluate the theoretical stability of the proposed treatment of the diffusion source terms, we will perform a one-dimensional von Neumann stability analysis. First, we decompose the vector of species mass fractions into the exact steady-state solution ($\mathbf{Y}^\circ$) and a small perturbation vector. Then, we expand this perturbation in a Fourier series by assuming a solution of the form

$$\mathbf{Y}(x,t) = \mathbf{Y}^\circ(x) + \mathbf{f}(t)e^{i\kappa x} \ , \tag{2.33}$$

where κ is the wavenumber and $\mathbf{f}(t)$ is the time-varying amplitude of the perturbation. Under small deviations from a steady-state solution, we can make the simplifying assumption that

$$\rho_k^{n+3/2} \approx \rho^{n+1/2} = \rho^\circ \ . \tag{2.34}$$

Similarly, all diffusion coefficients are evaluated from the steady-state solution.

From here, we rewrite Equation (2.21) in a point-wise form neglecting both the chemical source term—demonstrated to be stable by Savard et al. [34]—and the convective transport term, which is integrated explicitly in this stability analysis (i.e., not modified by sub-iterations). This transforms the set of N partial differential equations into a set of N ordinary differential equations, where N is the number of species. Equation (2.23) reduces to the form

$$\left(\mathbf{I} + \frac{\Delta t}{2}\boldsymbol{D}^{\mathrm{MA}}\kappa'^2\right)\left(\mathbf{f}_{k+1}^{n+3/2} - \mathbf{f}_k^{n+3/2}\right) = \mathbf{f}^{n+1/2} - \mathbf{f}_k^{n+3/2} - \frac{\Delta t}{2}\boldsymbol{D}^{\mathrm{MC}}\kappa'^2\left(\mathbf{f}_k^{n+3/2} + \mathbf{f}^{n+1/2}\right) \ , \tag{2.35}$$

where κ'^2 is the modified wavenumber, and $\boldsymbol{D}^{\mathrm{MA}}$ and $\boldsymbol{D}^{\mathrm{MC}}$ are the mixture-averaged and multicomponent diffusion coefficient matrices calculated from Equations (2.8) and (2.13), respectively. For the second-order central differencing scheme used, κ'^2 takes the form

$$\kappa'^2 = \frac{2}{\Delta x^2}\left[1 - \cos(\kappa\Delta x)\right] \ . \tag{2.36}$$

While here we apply this to a second-order central difference scheme, the stability analysis holds for any spatial discretization of the diffusion terms in Equation (2.23). In the

present case, the most unstable mode manifests as cell-to-cell oscillations corresponding to $\kappa = \pi/\Delta x$ and $\kappa'^2 = 4/\Delta x^2$.

Recall that $\mathbf{f}^{n+1/2}$ is the value at the previous time step as defined in step 0 of Section 2.3.1 and

$$\mathbf{f}_0^{n+3/2} \equiv \mathbf{f}^{n+1/2} \ . \tag{2.37}$$

Dropping the superscripts for clarity, we can reduce Equation (2.35) to

$$\mathbf{f}_{k+1} = \mathbf{A}\mathbf{f}_0 + \mathbf{B}\mathbf{f}_k \ , \tag{2.38}$$

where

$$\mathbf{A} = \left(\mathbf{I} + \frac{\Delta t}{2}\kappa'^2 \boldsymbol{D}^{\mathrm{MA}}\right)^{-1} \left(\mathbf{I} - \frac{\Delta t}{2}\kappa'^2 \boldsymbol{D}^{\mathrm{MC}}\right) \tag{2.39}$$

and

$$\mathbf{B} = \left(\mathbf{I} + \frac{\Delta t}{2}\kappa'^2 \boldsymbol{D}^{\mathrm{MA}}\right)^{-1} \left(\frac{\Delta t}{2}\kappa'^2 \left(\boldsymbol{D}^{\mathrm{MA}} - \boldsymbol{D}^{\mathrm{MC}}\right)\right) \ . \tag{2.40}$$

Inspecting Equation (2.38), matrix $\mathbf{A}$ is multiplied by the constant value of the previous time step ($\mathbf{f}_0$) and therefore does not contribute to the stability of the sub-iterations. We focus on the properties of the $\mathbf{B}$ matrix, which acts as the amplification/growth factor. Theoretically, the stability of the sub-iterations is ensured if the spectral radius of matrix $\mathbf{B}$, defined as the largest absolute value of the eigenvalues, is less than one:

$$\rho(\mathbf{B}) \leq 1 \ . \tag{2.41}$$

The matrix $\mathbf{B}$ has some interesting properties that deserve further discussion.

First, this matrix is proportional to the difference between the two diffusion matrices $\boldsymbol{D}^{\mathrm{MA}}$ and $\boldsymbol{D}^{\mathrm{MC}}$. Recall that the $\boldsymbol{D}^{\mathrm{MA}}$ is a purely diagonal matrix. Table 2.1 compares the eigenvalues of these matrices on the burned side of the lean hydrogen premixed flames (see Section 2.4.1 for details on the flame). The burned side of the flame is characterized by the largest diffusion coefficients and is expected to be the most unstable location within a flame as far as diffusion is concerned. The two sets of eigenvalues are extremely close, which is expected as the mixture-averaged diffusion model approximates the multi-component diffusion model. As a result, the norm of the difference of the two matrices is expected to be much less than the norm of either matrix. In other words, we anticipate that $\rho(\mathbf{B}) \ll 1$ regardless of the time-step size (Δt) and grid spacing (Δx).

$\boldsymbol{D}^{\mathrm{MC}\dagger}$	$\boldsymbol{D}^{\mathrm{MA}\dagger}$	$\mathbf{B}^{\mathrm{imp}}$	$\mathbf{B}^{\mathrm{exp}}$
0.0000	0.2984	0.0095	0.0000
0.3033	0.3003	0.0096	25.629
0.3053	0.3014	0.0126	25.800
0.3070	0.3023	0.0131	25.945
0.3860	0.4069	0.0163	32.614
0.4644	0.4585	0.0265	39.239
0.4735	0.4672	0.0276	40.012
1.1163	1.0859	0.0450	94.327
1.8968	1.8145	*0.9634*	160.276

Table 2.1: Eigenvalues for the multi-component (left) and mixture-averaged (center-left) diffusion matrices ($\boldsymbol{D}^{\mathrm{MC}}$ and $\boldsymbol{D}^{\mathrm{MA}}$) and absolute values of the eigenvalues for the amplification matrix ($\mathbf{B}$) for the implicit formulation (center-right) and explicit formulation (right) evaluated on the burned side of the lean hydrogen premixed flame (see section 2.4.1). † units are $10^{-3}\,\mathrm{m}^2/\mathrm{s}$. A time-step size of $\Delta t = 10^{-5}\,\mathrm{s}$ was used for $\mathbf{B}$.

One noticeable difference between $\boldsymbol{D}^{\mathrm{MC}}$ and $\boldsymbol{D}^{\mathrm{MA}}$ is the presence of a null eigenvalue for multi-component diffusion. As described in Section 2.2.3, the multi-component matrix is singular, and its kernel is spanned by the species mass fraction matrix, here $\mathbf{Y}^{\circ}$. Consider the special case of $\mathbf{f}_0 = \mathbf{Y}^{\circ}$. Leveraging the fact that $\mathbf{f}_0$ lies in the kernel of $\boldsymbol{D}^{\mathrm{MC}}$, the amplitude at the next sub-iteration will be

$$\mathbf{f}_1 = (\mathbf{A} + \mathbf{B})\,\mathbf{f}_0 = \mathbf{f}_0\ . \tag{2.42}$$

By recursive reasoning, one can show the property holds for all sub-iterations. In other words, this mode is unaffected by the iterative process and remains the same between time steps. This time-invariant mode is nothing more than the steady-state solution $\mathbf{Y}^{\circ}$. To avoid "double counting" in Equation (2.33), the eigenvalue analysis of the matrix $\mathbf{B}$ should be performed on the linear space not including the vector $\mathbf{Y}^{\circ}$.

Table 2.1 provides an example of the eigenvalues of the amplification matrix $\mathbf{B}$ for a time-step size of $\Delta t = 10^{-5}\,\mathrm{s}$. Practically, the eigenvector associated with the largest eigenvalue of $\mathbf{B}$ forms a small angle (~ 0.08 deg) with the species mass fraction vector ($\mathbf{Y}^{\circ}$). Hence, most of it is in the kernel of $\boldsymbol{D}^{\mathrm{MC}}$. Following the previous discussion, this eigenvalue (indicated in italics) should not be considered, and the overall stability

is controlled by the second-largest eigenvalue, in this case 0.0425. As expected, this eigenvalue is much less than unity, thus proving the stability of the iterative procedure. This should be compared to the stability of the explicit formulation obtained by setting $\boldsymbol{D}^{\mathrm{MA}} = 0$ in Eq. (2.40). Under these conditions, the spectral radius of $\mathbf{B}$ becomes

$$\rho(\mathbf{B}) = 2\frac{\Delta t}{\Delta x^2}\rho\left(\boldsymbol{D}^{\mathrm{MC}}\right) \approx 2\frac{\Delta t}{\Delta x^2}\max\left(\boldsymbol{D}^{\mathrm{MA}}\right), \tag{2.43}$$

which resembles a Fourier number. As shown by the large eigenvalue of the explicit-method amplification matrix, $\mathbf{B}^{\mathrm{exp}}$, in Table 2.1, solving the system of equations would not be stable at $\Delta t = 10^{-5}\,\mathrm{s}$ without the proposed implicit formulation. Section 2.5.1 presents an in-depth comparison of this theoretical stability criterion against practical numerical convergence results for a one-dimensional freely propagating flame.

2.4 Test cases

We will evaluate the performance of the proposed iterative method and the relative cost of the implemented memory algorithm in Section 2.5. We base our evaluation on two flow configurations: a one-dimensional, unstretched, laminar flame and a three-dimensional, statistically stationary, turbulent flame; both are premixed hydrogen/air flames. All simulations used the same nine-species hydrogen mechanism of Hong et al. [66] with updated rate constants from the same group [67, 68]. This section describes the configuration and conditions used for the one- and three-dimensional simulations used for this study. C includes additional method verification.

2.4.1 One-dimensional premixed flame

To verify the implementation of the multicomponent mass-diffusion model and evaluate its accuracy, we performed one-dimensional, unstretched (flat), laminar flame simulations and compared these with similar mixture-averaged and multicomponent results computed using Cantera [69]. We selected the one-dimensional flat flame configuration because it restricts all transport to the streamwise direction. As a result, the spanwise fluxes are zero by definition for this geometry. This condition may not hold in a multidimensional flow simulation where the multicomponent diffusion fluxes may be misaligned with the

species gradient vector. This simplified geometry allows us to directly compare the multicomponent mass diffusion model to the commonly used mixture-averaged diffusion model.

The simulations used an unburnt temperature of 298 K and pressure of 1 atm, with an equivalence ratio of $\phi = 0.4$ and inlet velocity equal to the laminar flame speed for all Cantera and NGA cases. The flame was centered in a computational domain comprised of 720 grid points where Δx =15.4 µm. To ensure fidelity in the results, we selected the domain to have at least 20 points through the laminar flame, with the thickness defined using the maximum temperature gradient: $l_F = (T_{\max} - T_{\min})/|\nabla T|_{\max}$. Schlup and Blanquart [18] used an identical configuration to investigate the impact of Soret and Dufour thermal diffusion effects.

We ran the Cantera simulations similarly using both mixture-averaged and multicomponent diffusion models with matching inlet conditions, equivalence ratio, and domain size. The freely-propagating adiabatic flat flame solver (`FreeFlame`) was used with grid refinement criteria for both slope and curvature set to 0.1 and a refinement ratio of 2.0 for 860 grid-points.

2.4.2 Three-dimensional flow configuration

We simulated a three-dimensional, turbulent, premixed, freely propagating flame as a test of the proposed algorithm for multicomponent mass diffusion and to assess the impact of diffusion model choice on global statistics such as the turbulent flame speed. The computational domain consists of inflow and convective outflow boundary conditions in the streamwise direction. The two spanwise directions use periodic boundaries. We set the inflow velocity to the mean turbulent flame speed, which keeps the flame statistically stationary such that turbulent statistics can be collected over an arbitrarily long run time. In the absence of mean shear, we use a linear turbulence-forcing method [14, 15] to maintain the production of turbulent kinetic energy through the flame. We carefully selected the Karlovitz number to fall within the distributed reaction zone regime while avoiding the broken reaction zone regime [70]. Moreover, the computational setup for this case is similar to those of Lapointe et al. [70], Burali et al. [23], and Schlup et at. [18], who studied differential-diffusion effects, local extinction, and flame broadening using the mixture-averaged model and constant non-unity Lewis number assumptions.

Table 2.2: Three-dimensional simulations parameters. Δx is the grid spacing, η_u is Kolmogorov length scale of the unburnt gas, Δt is the simulation time-step size, ϕ is the equivalence ratio, P_0 is the thermodynamic pressure, T_u is the temperature of the unburnt mixture, T_{peak} is the temperature of peak fuel consumption rate in the one-dimensional laminar flame, S_L is the laminar flame speed, $l_F = (T_b - T_u) / |\nabla T|_{\text{max}}$ is the laminar flame thickness, $l = u'^3/\epsilon$ is the integral length scale, u' is the turbulence fluctuations, ϵ is the turbulent energy dissipation rate, Ka_u is the Karlovitz number of the unburnt mixture, Re_t is the turbulent Reynolds number of the unburnt mixture, and ν_u is the unburnt kinematic viscosity.

Parameter	MA	MC
Domain	$8L \times L \times L$	
L	$190\Delta x$	
Grid	$1520 \times 190 \times 190$	
Δx [m]	4.24×10^{-5}	
η_u [m]	2.1×10^{-5}	
Δt [s]	6×10^{-7}	
ϕ	0.4	
P_0 [atm]	1	
T_{u} [K]	298	
T_{peak} [K]	1190	1180
S_L [m/s]	0.230	0.223
l_F [mm]	0.643	0.631
l/l_F	2	2.04
u'/S_L	18	18.6
$\text{Ka}_u = \tau_F/\tau_\eta$	149	151
$\text{Re}_t = (u'l)/\nu_u$	289	

Table 2.2 provides further details of the computational domain, unburnt mixture, and inlet turbulence. The unburnt temperature and pressure are 298 K and 1 atm, respectively. The inlet equivalence ratio is $\phi = 0.4$, with an unburnt Karlovitz number $\mathrm{Ka}_u = \tau_F/\tau_\eta = 149$, where $\tau_F = l_F/S_L$ is the flame time scale and $\tau_\eta = (\nu_u/\epsilon)^{1/2}$ is the Kolmogorov time scale of the incoming turbulence with unburnt kinematic viscosity ν_u and turbulent energy dissipation ϵ. The unburnt turbulent Reynolds number is $\mathrm{Re}_t = u'l/\nu_u = 289$, where u' is the fluctuation of the mean velocity and l is the integral length scale. The mean inflow velocity at the inlet boundary condition approximately matches the turbulent flame speed so that the flame remains relatively centered in the domain and we can perform arbitrarily long simulations. Once the turbulence has fully developed, we run the simulations for 22 eddy turnover times, $\tau_{\mathrm{eddy}} = k/\epsilon \approx 500\,\mu\mathrm{s}$.

The domain has 1520 points in the streamwise direction and 190 points in both spanwise directions, with a uniform grid size of $\Delta x = l_F/16$. This domain is about $100l_F$ long and $12l_F$ in the spanwise directions. Given the prescribed turbulence intensity, this mesh has a grid spacing equivalent to $\Delta x \approx 2\eta_u$, where η_u is the Kolmogorov length scale for the unburnt region; this resolution improves in the burnt region of the flame. Lapointe et al. [70] previously confirmed the suitability of the selected grid spacing and resolution in the flame front using a mesh refinement study, which found no difference when using this grid spacing compared with half the size. Figure 2.2 shows a two-dimensional schematic of the domain, including the locations of the flame and the forcing region. Figure 2.3 shows a three-dimensional view of the iso-surface of T_{peak} defining the flame front, where T_{peak} is the temperature of peak fuel consumption rate in the one-dimensional laminar flame. The flame surface shows the complex behavior of the flame in the turbulent field.

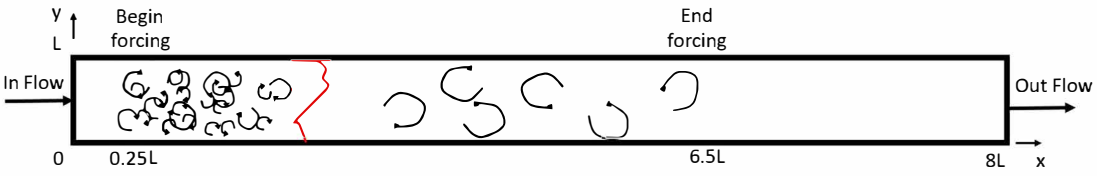

Figure 2.2: Two-dimensional schematic of the three-dimensional flame configuration. Adapted from Burali et al. and Schlup and Blanquart [18, 23]. The red line indicates the approximate location of the flame.

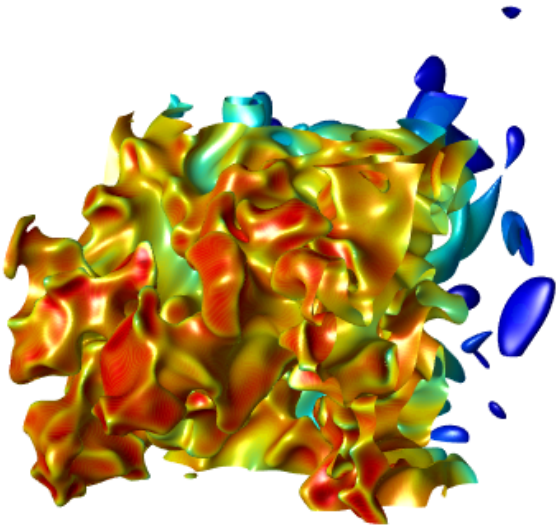

Figure 2.3: Iso-surface of peak temperature colored by OH mass fraction for a three-dimensional turbulent hydrogen/air flame with multicomponent mass diffusion.

2.5 Results and discussion

To start, we present a practical assessment of the method's convergence and stability, by comparing the numerical rate of convergence to the theoretical rate of convergence. Following this demonstration of the proposed method's stability, we verify the accuracy of the method through a posteriori assessment of one-dimensional, unstretched, premixed, laminar flame simulations. Finally, we present a preliminary evaluation of the relative differences between the mixture-averaged and multicomponent diffusion models for the three-dimensional turbulent premixed flame simulations.

2.5.1 Stability analysis results

We use the one-dimensional flame to numerically evaluate the convergence stability of the sub-iterations with respect to time-step size. The simulations for these tests were initialized from a mixture-averaged data file to provide a worst-case scenario for the initial iterative step in converging to the multicomponent solution. While the theoretical

analysis was performed assuming explicit transport of the convective terms and constant density/diffusion coefficients, we performed this test with semi-implicit transport and variable density/diffusion coefficients. This demonstrates the stability of the proposed preconditioner for the semi-implicit multicomponent diffusion transport in a practical numerical simulation. Savard et al. [34] previously showed the numerical stability of the chemical and convective terms, so we do not discuss these terms in detail in this analysis.

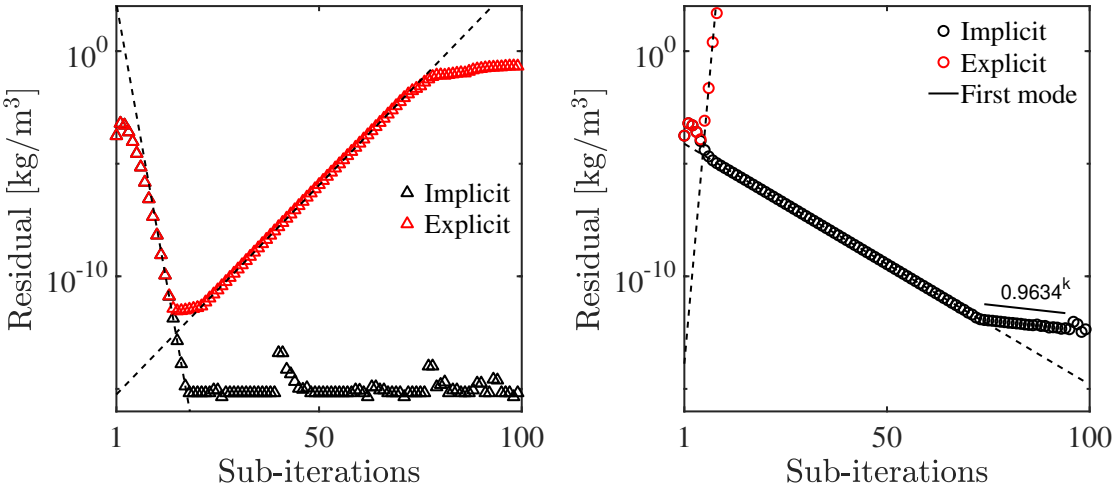

(a) $\Delta t = 10^{-7} s$ (b) $\Delta t = 10^{-5} s$

Figure 2.4: Convergence of the density residual as a function of sub-iteration for the proposed semi-implicit method, for a smaller and larger time-step size. Dashed lines are the spectral radii shown in Figure 2.5 and are determined by numerically fitting an exponential curve to the slope of the density residual

.

We focus on the maximum density residual over the whole domain, because its convergence is controlled by the convergence of all chemical species. Figures 2.4a and 2.4b present the density residuals as a function of sub-iteration, starting from the initial time step, for a small and large time-step size, respectively. For the time-step sizes tested, converging (as opposed to converged) sub-iterations implies a stable simulation, which agrees with behavior shown by Savard et al. [34]. In other words, unless the sub-iterations diverge, the simulation remains stable. As expected, the explicit method diverges quickly even at very small time-step sizes (Figure 2.4a), while the semi-implicit method remains stable up to a time-step size of $\Delta t \leq 1 \times 10^{-5}$ s (Figure 2.4b).

The rate of convergence of the sub-iterations for each of the source terms in Figures 2.4a and 2.4b follows an exponential relationship, i.e., $\text{Res}_k \sim r^k$, where Res_k is the residual of the kth sub-iteration and r is the convergence rate. We compute the numerical convergence rate r by fitting an exponential curve to the slope of the density residuals; the convergence rate is represented by dashed lines in Figure 2.4. Since density is a function of the species mass fractions, its convergence rate should tend towards that of the slowest-converging species mass fraction.

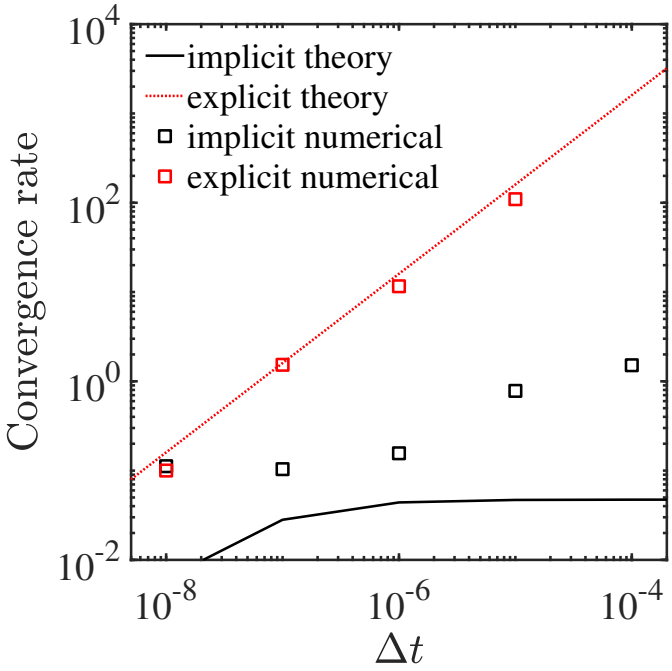

Figure 2.5: Theoretical convergence rate determined from diagonalizing matrix **B** corresponding to the worst-case modified wavenumber for the one-dimensional premixed flame, compared with the numerical convergence rates determined by fitting an exponential curve to the slope of the density residual.

Figure 2.5 compares the results of the theoretical and numerical stability analyses, showing the spectral radius of matrix **B** as a function of the time-step size for the one-dimensional test case. For the explicit scheme, the theoretical and numerical results agree well for the full range of time-step sizes. However, for the implicit scheme, the predicted spectral radius is much smaller than the measured one. The proposed implicit

formulation thus yields a convergence rate that is not limited by diffusion, but rather constrained by other processes that were not considered in the stability analysis, such as chemistry. The predicted convergence rate can nonetheless be observed in the implicit case. As mentioned in Section 2.3.4, the eigenvector associated with the largest eigenvalue of $\mathbf{B}^{\text{imp}}$ in Table 2.1 forms a small angle with $\mathbf{Y}^{\circ}$. Hence, a fraction of the error, albeit tiny, is associated with this eigenvector, which will slowly converge. In Figure 2.4b, the convergence rate for the last sub-iterations of the implicit case closely matches that eigenvalue.

Overall, these results suggest that the theory well-approximates actual stability and provides a practical limit for the numerical stability of the proposed algorithm.

2.5.2 Method verification

To verify the multicomponent model, we compare a posteriori the one-dimensional unstretched species profiles and laminar flame speeds. Figure 2.6 compares the nine species profiles for the steady-state one-dimensional flat flame solutions relative to local mixture temperature for the multicomponent and mixture-averaged models from both NGA and Cantera. The profiles all agree within 1 % at all points, with the exception of N_2. The laminar flame speeds (S_L^o) for these simulations are approximately 23.0 cm/s and 22.3 cm/s for the mixture-averaged and multicomponent diffusion NGA cases, respectively; the laminar flame speeds for both cases agree with those from Cantera within 1 %. The unstretched laminar flame speed is

$$S_L^o = -\frac{\int \rho \dot{\omega}_{\text{H}_2} dx}{\rho_u Y_{\text{H}_2,u}} \,, \tag{2.44}$$

where ρ_u is the unburnt mixture density and $Y_{\text{H}_2,u}$ is the unburnt fuel mass fraction. We attribute the larger difference in the species profile for N_2 to the correction velocity term associated with the mixture-averaged diffusion model, which is weighted by mass fraction and thus can be heavily impacted by differences in N_2 due to its high concentration throughout the flame. The minor differences between the multicomponent species profiles are less than 1 % at all points. The strong agreement between the other eight species profiles for both the NGA and Cantera results verifies the multicomponent model's functionality.

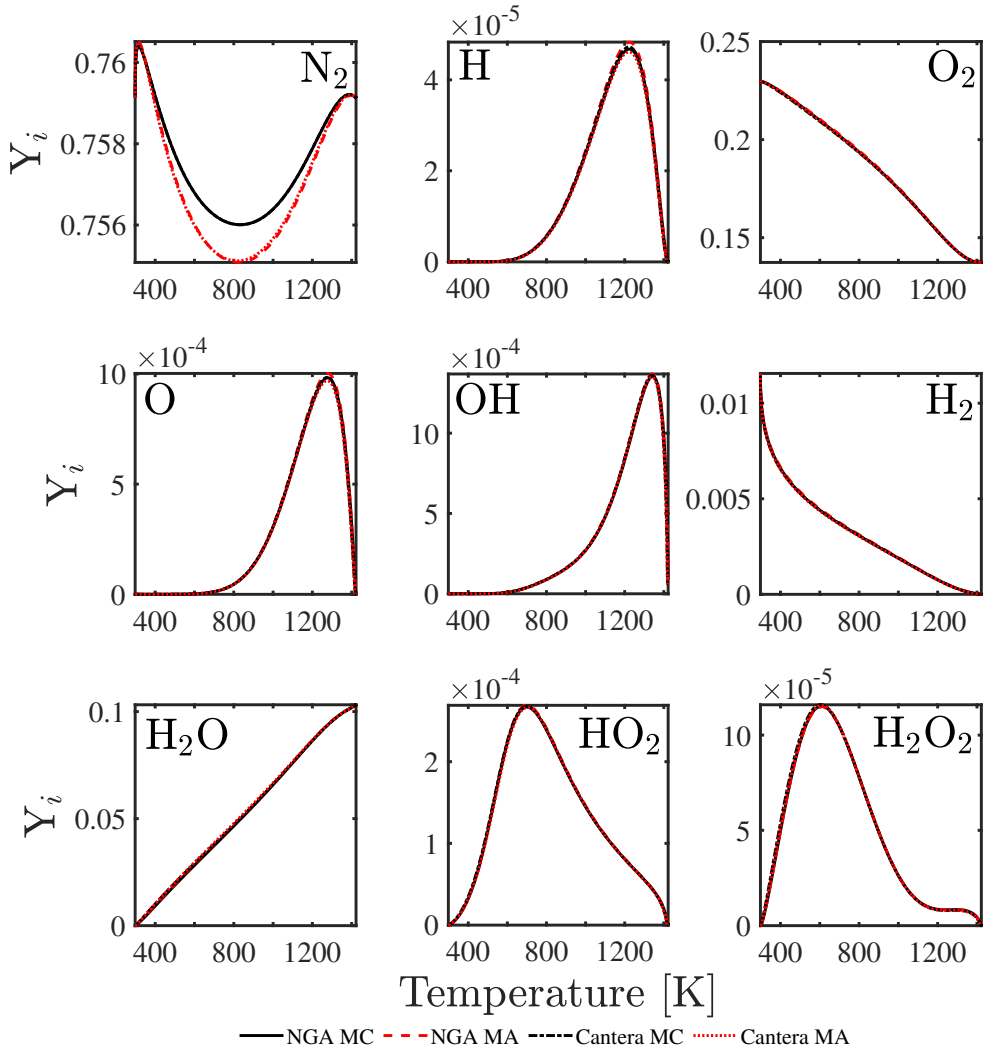

Figure 2.6: A posteriori comparisons of species mass fractions relative to mixture local temperature in a hydrogen/air flame with $\phi = 0.4$ using NGA and Cantera.

2.5.3 Accuracy

With the proposed algorithm's stability limits and functionality verified, we now examine the accuracy for a given stable simulation. We determine the order of accuracy of the method based on the 1D freely propagating flame case by examining the power-law dependence of the error as a function of the time-step size.

Figure 2.7 shows the normalized error for the 1D freely propagating flame case for various time steps. We initialize the simulation using an input flame profile corresponding to a fully converged statistically stationary flame, generated with a time-step size of $\Delta t = 1 \times 10^{-7}$ s and seven sub-iterations. A wall is then set at the simulation inlet, allowing the flame to propagate upstream in the domain. We then let the reference flame propagate for two flame pass-through times to ensure a fully converged freely propagating flame profile free of any initial transients due to the transition from the input stationary flame profile. This reference file then serves as the input for a set of freely propagating flames with time-step sizes ranging 10^{-5}–10^{-7} s and for seven sub-iterations. Finally, we allow these test flames to propagate for an additional flame pass-through time to ensure statistical independence from the initial reference-flame input file.

With the freely propagating flame tests completed, we interpolated the species and density fields to a constant temperature space corresponding to the temperature distribution in the flame region. This interpolation ensures a direct comparison of the species error independent of variation in the temperature space over the range of time-step sizes. We then calculate error as the L^2-norm of the species and density profiles in temperature space, relative to the reference flame profile with $\Delta t = 1 \times 10^{-7}$ s and seven sub-iterations:

$$\text{error} = \sqrt{\frac{\int \left(Y_i - Y_{i,\text{ref}}\right)^2 dT}{\int Y_{i,\text{ref}}^2 dT}} \tag{2.45}$$

and

$$\text{error} = \sqrt{\frac{\int \left(\rho - \rho_{\text{ref}}\right)^2 dT}{\int \rho_{\text{ref}}^2 dT}} \,. \tag{2.46}$$

We selected the species H_2, H_2O, OH, and H to evaluate the accuracy of the method because they represent the reactants, intermediate species, and products present in hydrogen combustion. Density (ρ) is also included to globally assess error, since it depends on all species. As shown in Figure 2.7a, all quantities exhibit second-order

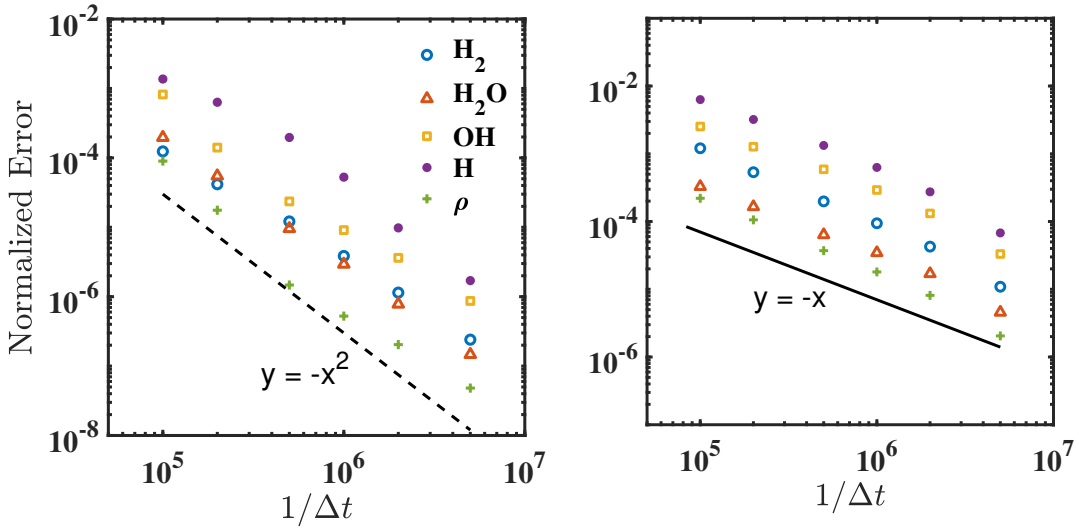

(a) Seven sub-iterations

(b) Four sub-iterations

Figure 2.7: Relative accuracy of the method as a function of time step size for the one-dimensional, freely propagating flame test case with seven sub-iterations. Errors are defined as the absolute difference of their integrated value in temperature space compared with a reference solution obtained for $\Delta t = 1 \times 10^{-7}$ s and seven sub-iterations. Black dashed line corresponds to $y = x^{-2}$.

accuracy in time with seven sub-iterations. The errors corresponding to the L^1- and L^∞-norms are similar in magnitude and also demonstrate second-order accuracy in time with seven sub-iterations.

While the method is fully second-order accurate for seven sub-iterations and above, the solution transitions to first-order accuracy as the number of sub-iterations decreases. Figure 2.7b shows that the solution exhibits first-order accuracy when using four sub-iterations. Between four and seven sub-iterations the solution is second-order accurate for large time-step sizes but transitions to first-order accuracy as the time step size decreases. The range of time-step sizes that achieve second-order accuracy grows until the solution becomes fully second-order accurate at seven sub-iterations for all time-step sizes considered.

To evaluate the absolute magnitude of error associated with the proposed method, as opposed to the order of accuracy (as time step size approaches zero), Figures 2.8a and 2.8b present the temperature as a function of distance and fuel mass fraction as a function of temperature, respectively, for a range of freely propagating flames with several time-step sizes and sub-iterations. The solutions exhibit negligible error in both temperature and fuel mass fractions for the time-step sizes considered, and even when using as few as four sub-iterations; these tests demonstrate the high accuracy and robustness of the proposed method.

2.5.4 Three-dimensional assessment of diffusion flux models

In this section we assess a posteriori the species mass diffusion fluxes in the doubly periodic three-dimensional flames [18, 22, 23]. Differential diffusion effects cause the instabilities found in lean hydrogen/air flames, and at high Karlovitz numbers the turbulence time scales match the order of diffusion time scales.

To assess the impact of the mixture-averaged and multicomponent mass diffusion models on flame chemistry, we compare a posteriori the turbulent and chemistry statistics. We allow the flames to develop in a turbulent flow field, and compute the statistics after the transients from the initial flow and scalar fields have advected through the domain. As an initial assessment, we calculate the effective turbulent flame propagation speeds:

$$S_{\mathrm{T}} = -\frac{\int_V \rho \dot{\omega}_{\mathrm{H}_2} dV}{\rho_u Y_{\mathrm{H}_2,u} L^2} \ . \tag{2.47}$$

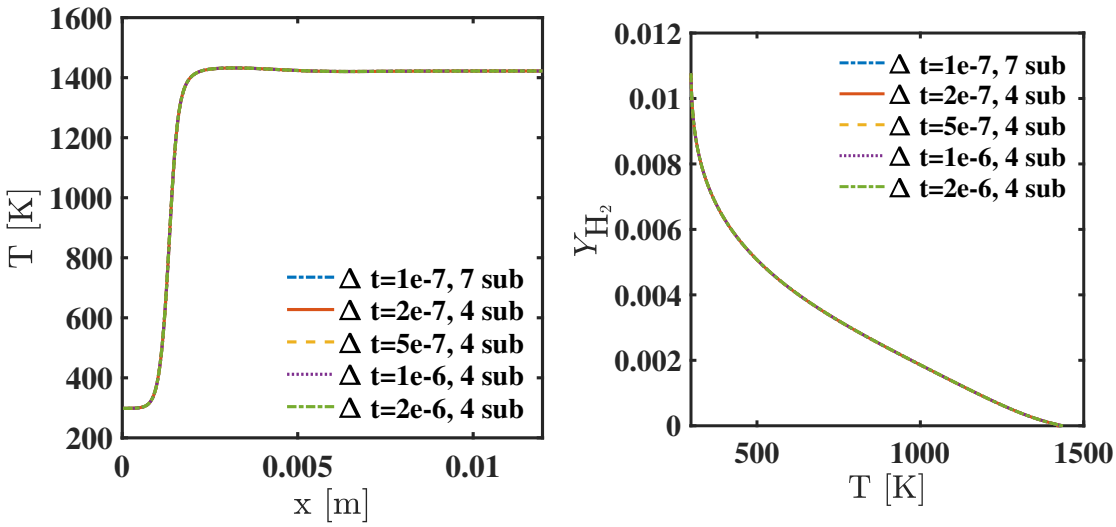

(a) Temperature vs. distance

(b) H_2 mass fraction vs. temperature

Figure 2.8: Impact of time-step size and number of sub-iterations on the accuracy of one-dimensional freely propagating flames.

Figure 2.9 shows the time history of the turbulent flame speed over twenty-two eddy turn-over times (τ_{eddy}). The average normalized flames speeds from the mixture-averaged and multicomponent models differ by 15 %: $S_T^{\text{MA}}/S_L = 29.6$ and $S_T^{\text{MC}}/S_L^0 = 34.7$, respectively. Further study is needed on whether the mixture-averaged diffusion model fully captures the fundamental physics of multicomponent diffusion.

To further assess any differences between the mixture-averaged and multicomponent mass diffusion models, Figure 2.10 presents the means of fuel mass fraction and its source term conditioned on temperature for the full time domain. The differences in the calculated conditional means are small: less than 5.5 %. This agreement also extends into super-adiabatic regions for the hydrogen/air flame; these regions, also called “hot spots”, result from differential diffusion and have been predicted both in theoretical studies [71] and numerical analyses of lean hydrogen/air mixtures [72–74]. However, these small differences in global flame statistics do not explain the 15 % difference observed in the turbulent flame speeds between the mixture-averaged and multicomponent diffusion models. These results raise questions on the appropriateness of the mixture-averaged diffusion assumption for direct numerical simulation and warrants further investigation.

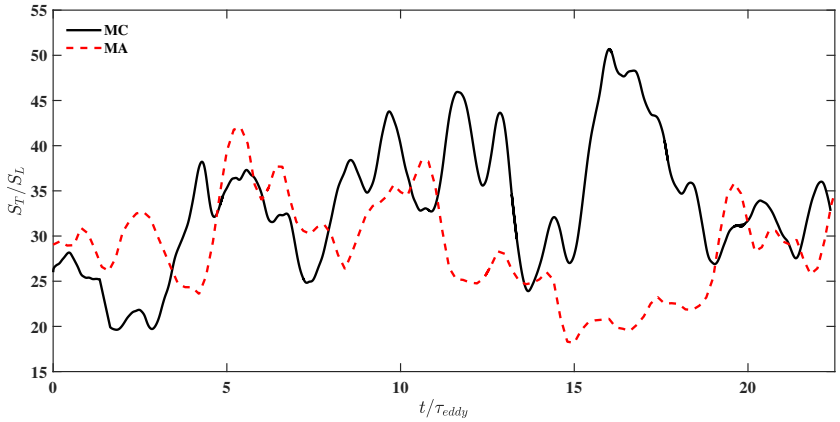

Figure 2.9: Turbulent flame speed history for three-dimensional, freely propagating, premixed, turbulent hydrogen/air flame with $\phi = 0.4$.

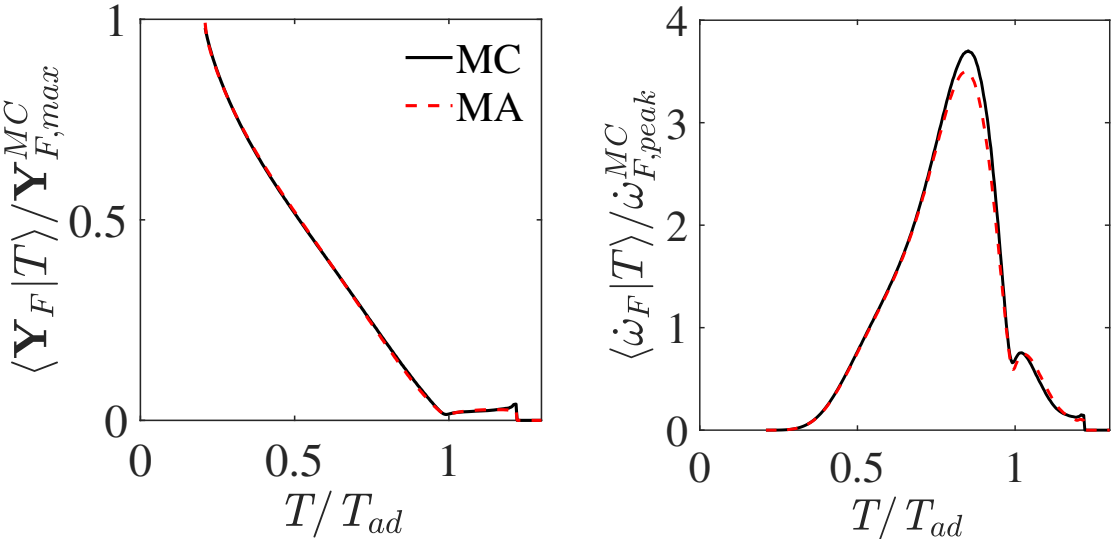

(a) Fuel mass fraction

(b) Fuel chemical source term

Figure 2.10: Conditional means on temperature for the three-dimensional, freely propagating, premixed, turbulent hydrogen/air flame with $\phi = 0.4$.

2.5.5 Computational cost

This section discusses the relative cost for implementing the full multicomponent mass diffusion to provide context for its use. The presented timing comparisons examine how the method scales with both number of chemical species and spatial dimension.

We tested three chemical kinetic models (containing 9 [23], 35 [56, 57], and 172 species [75–77]) in a one-dimensional flat flame simulation to determine the cost of multicomponent mass diffusion over a wide range of model sizes. Figure 2.11 shows the computational time per grid point for computing the diffusion mass fluxes on a desktop workstation using an Intel Xeon-X5660 CPU with a 2.80 GHz clock speed. The presented timings include calculation of both the diffusion coefficients and mass diffusion fluxes for all aspects of the code.

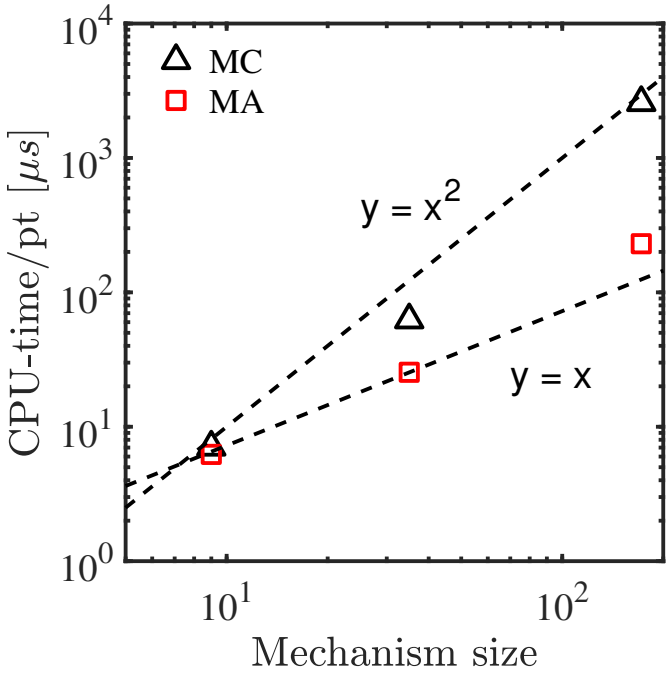

Figure 2.11: Computational time per grid point for computing diffusion coefficients and diffusion mass fluxes using kinetic models with 9, 35, and 172 species; black dashed lines correspond to linear ($y = x$) and quadratic ($y = x^2$) scaling trends respectively. MC and MA stand for multicomponent and mixture-averaged, respectively.

For the tested chemical kinetic models, the mixture-averaged model scales linearly

while the multicomponent model scales quadratically with the number of species. The multicomponent model is more expensive and does take more time per-point for all three test cases. For the largest kinetic model (with 172 species) the multicomponent case is noticeably more expensive than the mixture-averaged model. The increased cost for the multicomponent simulations comes primarily from the CHEMKIN II [50] routine used to determine the ordinary multicomponent diffusion coefficient matrix.

The relevant cost for the proposed method can be split into three primary categories: the costs of calculating the multicomponent diffusion coefficients, calculating the multicomponent diffusion fluxes, and the semi-implicit integration scheme. Since the proposed method for implementing full multicomponent mass diffusion focuses on efficient low-memory calculation of the diffusion fluxes, rather than the multicomponent diffusion coefficients, the cost of CHEMKIN should be considered independently of the proposed algorithm. Moreover, the semi-implicit scheme is the same for the mixture-averaged and multicomponent cases, because both cases use the mixture-averaged diffusion coefficient matrix to approximate the Jacobian for the diffusion source terms. As a result, the two methods have similar implementation and computational expense, with the exception of using CHEMKIN II [50].

To evaluate how the multicomponent model scales with increasing spatial dimension, and evaluate the relative cost of using CHEMKIN II [50], we acquired timings for one- (720 grid points), two- (1888×472 grid points), and three-dimensional ($1520 \times 190 \times 190$ grid points) configurations covering the cases presented in this work, with the additional two-dimensional case matching similar timing tests by Schlup et al. [18]. These timing tests represent an average cost per point and are determined by averaging the timings taken for the 20 time steps, skipping the first and last integrations. Figure 2.12 presents the computational timings for each part of the code for both diffusion models, where "Scalar" includes scalar field calculation; "Diffusion" includes the flux calculation and $\boldsymbol{D}^{\mathrm{MA}}$ calculation for the implicit solver; "Chemistry", "Velocity", and "Pressure" are as named; and "Rest" account for any remaining computations. "Scalar" includes the semi-implicit solver for integrating the diffusion source terms, while the semi-implicit solvers for chemistry and velocity are included in their named categories. To facilitate comparison between the two models, Figure 2.13 presents the total computational time per grid point for both three-dimensional hydrogen simulations as a stacked bar chart broken down by each section of code. We performed these computations on the National

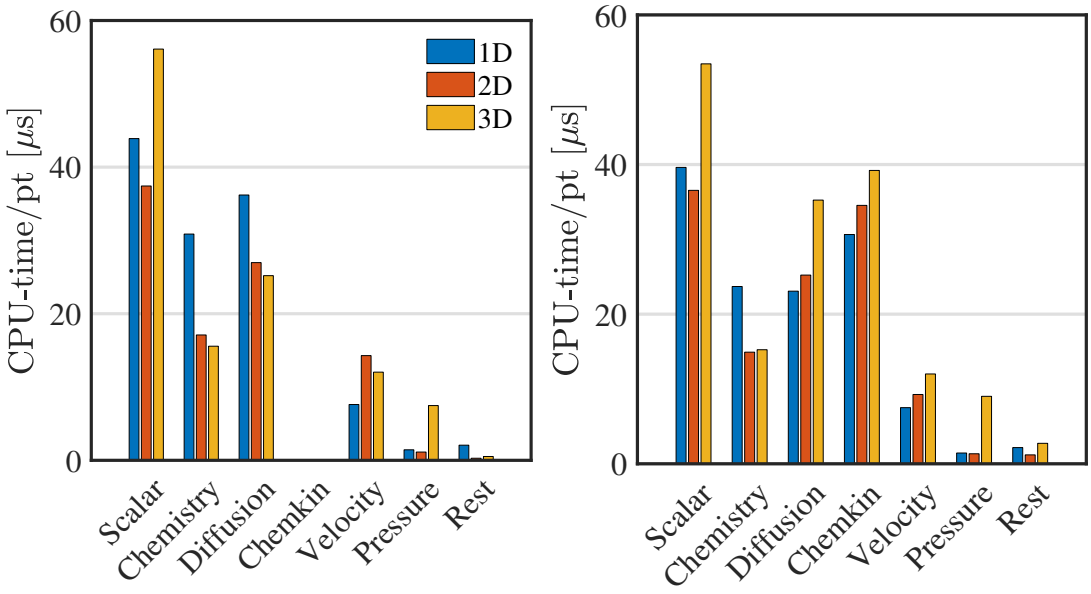

(a) Mixture-averaged model

(b) Multicomponent model

Figure 2.12: Computational time per grid point for each of the three flame configurations: one dimensional (blue), two dimensional (red), and three dimensional (yellow).

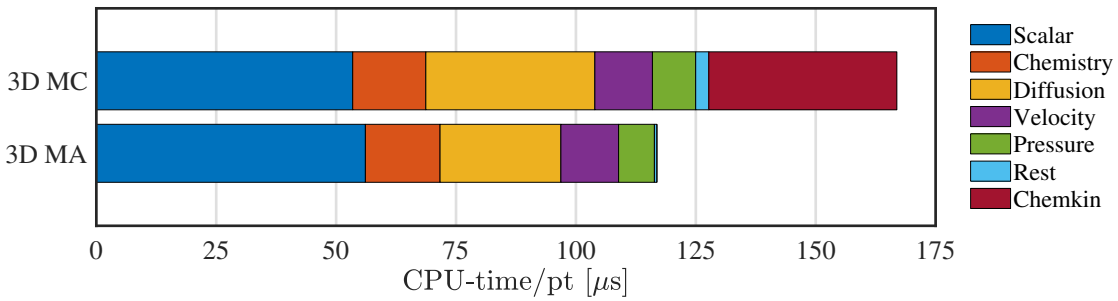

Figure 2.13: Comparison of numerical costs for the three-dimensional hydrogen flame simulations.

Energy Research Scientific Computing Center (NERSC) high-performance computing cluster Cori (Cray XC40) [78].

While much of the code exhibits a similar cost per grid point, regardless of the dimensionality of the problem, the chemistry is more expensive for the one- and two-dimensional cases. This cost increase is due to NGA's structure. NGA was written and optimized for three-dimensional configurations, thus the one- and two-dimensional cases are artificially more expensive, especially in the chemistry calculations [18]. In addition, for three dimensions the cost of the pressure solver increases due to using the HYPRE package [61]. The one- and two-dimensional cases both implement an exact FFT-tridiagonal solver, while HYPRE—used for the three-dimensional cases—is iterative and thus more expensive. Despite the minor increase in cost for the pressure solver in three dimensions, the cost is negligible when considering larger kinetic models (i.e., more than 35 species).

Consistent with Figure 2.11, the cost of calculating "Diffusion" increases with model complexity; recall that $\boldsymbol{D}^{\mathrm{MA}}$ is calculated for both the mixture-averaged and multicomponent solvers. However, the multicomponent diffusion mass flux calculation represents only 21 % of the total simulation time for the three-dimensional case. As expected, the cost of calling CHEMKIN II for the diffusion coefficients is large and accounts for roughly 23 % of the three-dimensional simulation time. Interestingly, the cost of diffusion increases only slightly moving from one dimension to two dimensions. This results from the high efficiency of the dynamic memory-allocation algorithm used to implement this model (see Section 2.3.3). Moreover, the multicomponent diffusion implementation is less expensive than the mixture-averaged model for the one-dimensional case and equivalent in cost for the two-dimensional case. Overall, by reducing memory requirements and optimizing calls to memory, the memory algorithm implemented for the multicomponent model maintains low computational expense.

These results indicate that, for hydrogen-air combustion, the multicomponent model is more expensive than the mixture-averaged model; however, the differences in "Diffusion" costs between the two models are due to the use of CHEMKIN II [50]. Thus, the slowdown could be minimized by implementing a more-efficient package for calculating the mass-diffusion coefficients such as EGLIB [29–31]; however, the total cost of computing mass diffusion fluxes remains notable, even for the mixture-averaged case.

2.6 Summary and future work

This article presents an efficient and stable scheme for implementing multicomponent mass diffusion in reacting-flow DNS with minimal memory expense. The proposed scheme exhibits reasonable computational cost for chemical kinetic models of up to 100 species; this performance could be further improved by implementing a more-efficient method for calculating the multicomponent diffusion coefficient matrix.

The results presented for hydrogen flames suggest that the mixture-averaged mass diffusion model may suffice for DNS of three-dimensional, premixed turbulent flames in the regimes and configurations considered. However, we observed a 15 % difference in the turbulent flame speeds between the two models, though the differences in the conditional means of the fuel source term and mass fraction were negligible. The difference observed in turbulent flame speeds raises questions about using the mixture-averaged model in DNS of turbulent reacting flows. Moreover, the algorithm proposed in this study provides a fast, efficient, method for implementing multicomponent mass diffusion in reacting-flow simulations, which may eliminate the need for the mixture-averaged assumption. However, despite these results, we do not have sufficient data to draw firm conclusions on the accuracy and appropriateness of mixture-averaged assumptions for all flames (i.e., all fuels, configurations, and regimes). Additional data are needed from studies of different fuels—namely large hydrocarbons—and kinetic models with more species. Thus, future work should focus on extending these comparisons to other fuels and flame configurations.

Acknowledgements

This material is based upon work supported by the National Science Foundation under Grant No. 1314109-DGE. This research used resources of the National Energy Research Scientific Computing Center (NERSC), a U.S. Department of Energy Office of Science User Facility operated under Contract No. DE-AC02-05CH11231.

2.7 Availability of material

The figures in this article, as well as the data and plotting scripts necessary to reproduce them, are available openly under the CC-BY license [79]. Furthermore, the full simulation results from NGA are available for the three-dimensional multicomponent [80] and

mixture-averaged [81] hydrogen/air flames.

Assessing the impact of multicomponent diffusion in direct numerical simulations of premixed, high-Karlovitz, turbulent flames

Aaron J. Fillo, Jason Schlup, Guillaume Blanquart, and Kyle E. Niemeyer

In preparation for submission.

Chapter 3: Assessing the impact of multicomponent diffusion in direct numerical simulations of premixed, high-Karlovitz, turbulent flames

Implementing multicomponent diffusion models in numerical combustion studies is computationally expensive; as a result, mixture-averaged diffusion treatments are commonly used to reduce the cost of the numerical simulations. However, the accuracy and appropriateness of mixture-averaged diffusion has not been verified for three-dimensional, turbulent, premixed flames. In this study we evaluated the role of multicomponent mass diffusion in premixed, three-dimensional high Karlovitz-number hydrogen, n-heptane, and toluene flames, representing a range of fuel Lewis numbers. We performed direct numerical simulations of these flames by implementing the Stefan–Maxwell equations in NGA. We also studied a premixed, unstable two-dimensional hydrogen flame due to the importance of diffusion effects in such cases. Our comparison of diffusion flux vectors revealed significant differences of 10–20 % between the mixture-averaged and multicomponent diffusion models in regions of high flame curvature. To evaluate the impact of these differences between the two models, we compared normalized turbulent flame speeds and conditional means of species mass fraction and source term. We found differences of 5–20 % in the mean normalized turbulent flame speeds, which seem to correspond to differences of 5–10 % in the peak fuel source terms. Our results indicate that the mixture-averaged diffusion model may not be sufficient for the DNS of premixed turbulent flames.

Keywords: DNS; Turbulent flames; Diffusion; Multicomponent; Mixture averaged

3.1 Introduction

Mass, heat, and momentum diffuse simultaneously in turbulent reacting flows, affecting local transport and consumption of chemical species at small time and length scales [20, 26]. This coupling of turbulent mixing and heat release during the combustion process can locally impact the flame's structure, curving it and forming steep, multi-directional gradients in the temperature and scalar fields [3]. In these regions of high flame curvature,

mass diffusion transport is most accurately represented by the multicomponent diffusion model, which uses a dense matrix of coupled diffusion coefficients to evaluate the relative transport of each chemical species against the remaining species in the mixture [27].

However, modeling full multicomponent mass diffusion transport in a direct numerical simulation (DNS) can be computationally expensive, caused both by the cost of calculating the diffusion coefficients and the memory required to store the multicomponent diffusion coefficient matrix at every location [82]. As a result, researchers typically use simplified diffusion models to reduce the computational costs associated with calculating the diffusion coefficients [23, 40]. These include, in order of increasing complexity and accuracy, the unity Lewis number, constant non-unity Lewis number [28], and mixture-averaged diffusion assumptions [20]. These models approximate the full multicomponent diffusion coefficient matrix as a constant scalar, a constant vector, and a non-constant diagonal matrix, respectively, reducing the high computational expense associated with numerical combustion studies [18, 20, 22, 23, 27]. In addition, several approaches further reduce the system's complexity by approximating multicomponent diffusion processes in terms of equivalent Fickian processes, such as those used by Warnatz [35] and Coltrin et al. [36]. While these assumptions may be computationally efficient, to our knowledge, the accuracy and appropriateness of the physics they model has not been evaluated against full multicomponent mass diffusion for DNS of three-dimensional turbulent flames at moderate-to-high Karlovitz numbers (e.g., 140–210).

Although few results exist from three-dimensional reacting flow simulations with multicomponent transport, several studies have investigated the effects of multicomponent transport in simpler configurations. These studies include one-dimensional [31, 37–40] and two-dimensional flames [19, 42] of various unburnt conditions. These works compared the multicomponent model with various diffusion and transport property models (from constant Lewis number to mixture-averaged properties). In general, these studies highlighted the importance of differential diffusion effects but only investigated simplified flame configurations where these effects are relatively small, such as unstretched laminar flames.

For example, in evaluating five simplified diffusion models, Coffee and Heimerl [37] observed that laminar flame speed and species profiles are more sensitive to the input values of individual species transport properties than the specific model used, in one-dimensional, steady, laminar, premixed hydrogen flame simulations. They noted that their

findings do not indicate that transport phenomenon or model selection are unimportant, but rather that even low-complexity models can be calibrated by carefully selecting the species transport properties to improve accuracy.

Focusing more on the underlying physics of differential diffusion, Ern and Giovangigli [31] demonstrated that both methane and hydrogen counterflow flames are sensitive to multicomponent transport. Specifially, neglecting multicomponent effects can lead to overpredicting the extinction strain rate, especially in rich hydrogen flames. Similarly, Charentenay and Ern [42] demonstrated that multicomponent transport only moderately affects global flame properties in two-dimensional, low Karlovitz number, premixed hydrogen/oxygen flames, thanks to the smoothing induced by turbulent fluctuations. However, when in highly curved flames or flames with local quenching, such as at moderate-to-high Karlovitz numbers, they concluded that the sufficiently large impact of multicomponent transport justifies its inclusion in accurate DNS.

Despite this evidence that multicomponent transport may impact the accuracy of turbulent premixed DNS, studies of three-dimensional turbulent flames continue to rely on simplified diffusion models and do not consider their accuracy relative to multicomponent diffusion, in complex configurations. Prior evaluations of diffusion models in three-dimensional simulations involved comparing the unity Lewis number, constant but non-unity Lewis number, and mixture-averaged approximations. For example, Lapointe and Blanquart [22] compared the relative accuracy of the unity and non-unity Lewis number assumptions for n-heptane, iso-octane, toluene, and methane flames. The flames simulated using the non-unity Lewis number approximation have lower turbulent flame speeds than similar flames simulated with the unity Lewis number assumption. They attributed these differences to reduced fuel-consumption rates caused by differential diffusion effects [22]. Similarly, Burali et al. [23] compared the non-unity Lewis number assumption to the mixture-averaged diffusion for lean, unstable hydrogen/air flames and lean, turbulent n-heptane/air flames. They demonstrated that using the unity Lewis number assumption underpredicts by 50 % or more the conditional means of the fuel mass fraction and source term, but using the non-unity Lewis number assumption results in much smaller errors, on the order of 3 % or less; both were compared with results using the mixture-averaged assumption [23]. Moreover, Burali et al. [23] demonstrated that the relative error associated with the non-unity Lewis number assumption can be minimized by carefully selecting the Lewis-number vector for a wide range of flames,

including non-premixed turbulent configurations.

These results reinforce previous conclusions that differential-diffusion effects can impact flame dynamics. However, there has not been a detailed investigation of the accuracy and appropriateness of the mixture-averaged diffusion model relative to full multicomponent diffusion for turbulent reacting flows. For high-pressure, non-reacting systems, Borchesi and Bellan [45] developed and analyzed multicomponent species mass flux and turbulent mixing models for large-eddy simulations. They focused on turbulent mixing of a five-species combustion-relevant mixture of n-heptane, oxygen, carbon dioxide, nitrogen, and water. Their multicomponent transport model significantly improves the accuracy and fidelity of the solution throughout the mixing layer. However, as this study was restricted to non-reacting flows, it did not assess the impact of multicomponent transport on the chemistry inherent in turbulent combustion.

Motivated by the observed errors of the mixture-averaged and simpler diffusion models, several groups have developed affordable multicomponent transport models. Ern and Giovangigli [29–31] developed the computationally efficient Fortran library EGLIB for accurately determining transport coefficients in gas mixtures. Ambikasaran and Narayanaswamy [32] proposed an efficient algorithm to compute multicomponent diffusion velocities, which scales linearly with the number of species. Both these methods focus on reducing the computational cost that comes from inverting the dense matrix associated with the Stephan–Maxwell equations. Most recently, Fillo et al. [82] proposed a fast, semi-implicit, low-memory algorithm for implementing multicomponent mass diffusion, which we use here with the DNS code NGA. As a preliminary demonstration of their method, Fillo et al. [82] simulated lean, premixed, three-dimensional turbulent hydrogen/air flames at moderate-to-high Karlovitz numbers using the mixture-averaged and multicomponent diffusion models. In these flames, the mixture-averaged diffusion model underpredicts the peak mean source term and normalized turbulent flame speed by 5.5 % and 15 %, respectively [82].

In addition to mass diffusion, several groups have also investigated the impact of multicomponent Soret and Dufour thermal diffusion effects. In particular, studies have examined the importance of including thermal diffusion in a wide range of flame configurations [18, 19, 30, 31, 37, 39, 83, 84]. For example, Giovangigli [19] demonstrated that multicomponent Soret effects significantly impact a wide range of laminar hydrogen/air flames. Specifically, multicomponent Soret effects influence laminar flame speeds and

extinction stretch rates for flat and strained premixed flames, respectively. Using a mechanistic approach, Yang et al. [83] observed that Soret diffusion of hydrogen radical (H) in premixed hydrogen flames actively modifies its concentration and distribution in the reaction zone. This effect was especially evident in symmetric, twin, counter-flow premixed hydrogen flames, where Soret diffusion increases and decreases individual reaction rates in lean and rich mixtures, respectively. Performing a similar mechanistic approach examining planar and stretched premixed *n*-heptane and hydrogen flames, Xin et al. [84] demonstrated that these chemical kinetic effects result from Soret diffusion diluting or enriching the reactant concentrations in the reaction front, and could substantially impact fuel burning rates—especially in highly stretched flames.

Finally, Schlup and Blanquart [18] examined the impact of multicomponent thermal diffusion in DNS of turbulent, premixed, high-Karlovitz hydrogen/air flames. They observed that simulations using the mixture-averaged thermal diffusion assumption underpredict flame speeds compared with simulations using full multicomponent thermal diffusion. In addition, they observed that including multicomponent thermal diffusion increases local production rates in in regions of high positive curvature [18]. These observed discrepancies in similar flame simulations with different diffusion models warrant a detailed investigation of the fundamental transport phenomena involved. However, while thermal diffusion can be important in some fuel/air mixtures, in this article we focus on mass diffusion, and direct interested readers to the work of Schlup and Blanquart [18], for example, for an investigation of these effects.

The primary objective of this study is to evaluate the accuracy and appropriateness of the mixture-averaged diffusion assumption for use in direct numerical simulations (DNS) of premixed unsteady laminar and turbulent flames. This objective will be realized via an a priori analysis of the orientation and magnitude of the mixture-averaged diffusion flux vector, relative to that of the multicomponent model, for a range of flame configurations. We will further analyze differences between the diffusion models by considering a posteriori results of turbulent flame structures (i.e., species mass fraction and source term profiles). Finally, we will compare the time history and average normalized turbulent flame speeds of hydrogen/air, *n*-heptane/air, and toluene/air flames as a global measure of the differences between the multicomponent and mixture-averaged diffusion models.

The paper is organized as follows: Section 3.2 describes the governing equations, diffusion models, and flow configurations for the simulations. Then, Section 3.3 presents

the results from a priori, a posteriori, and turbulent flame speed analyses. Finally, in Section 3.4 we draw conclusions from the comparisons of the diffusion models.

3.2 Numerical approach

This section describes the governing reacting-flow equations and flow solver used, and briefly discusses the diffusion models to be studied. It also presents the two- and three-dimensional flow configurations used.

3.2.1 Governing equations

We solve the variable-density, low Mach number, reacting flow equations using the finite-difference code NGA [33, 34]. The complete conservation equations are

$$\frac{\partial \rho}{\partial t} + \nabla\cdot(\rho\mathbf{u}) = 0\,, \tag{3.1}$$

$$\frac{\partial \rho\mathbf{u}}{\partial t} + \nabla\cdot(\rho\ \mathbf{u}\otimes\mathbf{u}) = -\nabla p + \nabla\cdot\boldsymbol{\tau} + \mathbf{f}\,, \tag{3.2}$$

$$\frac{\partial \rho T}{\partial t} + \nabla\cdot(\rho\mathbf{u}T) = \nabla\cdot(\rho\alpha\nabla T) + \rho\dot{\omega}_T - \frac{1}{c_p}\sum_i^N c_{p,i}\mathbf{j}_i\cdot\nabla T + \frac{\rho\alpha}{c_p}\nabla c_p\cdot\nabla T\,, \tag{3.3}$$

$$\frac{\partial \rho Y_i}{\partial t} + \nabla\cdot(\rho\mathbf{u}Y_i) = -\nabla\cdot\mathbf{j}_i + \rho\dot{\omega}_i\,, \tag{3.4}$$

where ρ is the mixture density, t is time, $\mathbf{u}$ is the velocity, p is the hydrodynamic pressure, $\boldsymbol{\tau}$ is the viscous stress tensor, $\mathbf{f}$ represents volumetric forces, T is the temperature, α is the mixture thermal diffusivity, $c_{p,i}$ is the constant-pressure specific heat of species i, N is the number of species, c_p is the constant-pressure specific heat of the mixture, and $\mathbf{j}_i$, Y_i , and $\dot{\omega}_i$ are the diffusion flux, mass fraction, and production rate of species i, respectively. In Eq. (3.3), the temperature source term is given by

$$\dot{\omega}_T = \frac{-1}{c_p}\sum_i^N h_i(T)\dot{\omega}_i\,, \tag{3.5}$$

where $h_i(T)$ is the specific enthalpy of species i as a function of temperature. The density is determined from the ideal gas equation of state.

NGA solves Eqs.(3.1)–(3.4) using a numerical scheme second-order accurate in both

space and time [33, 34], using a semi-implicit Crank–Nicolson time integration method [59]. It uses the third-order Bounded QUICK scheme (BQUICK) [58] as the scalar transport scheme. We discuss the diffusion solver in more detail next in Section 3.2.2.

3.2.2 Overview of diffusion models

The diffusion fluxes are calculated using the semi-implicit scheme developed by Fillo et al. [82] with either mixture-averaged [20] or multicomponent [27] models, both of which are based on Boltzmann's equation for the kinetic theory of gases [27, 47]. For this study, we neglect both baro-diffusion and thermal diffusion (Soret and Dufour effects). The baro-diffusion term is commonly neglected in reacting-flow simulations under the low Mach number approximation [48]. We also neglect thermal diffusion because our objective is to investigate the impact of mass diffusion models; Schlup and Blanquart previously explored the effects of thermal diffusion modeling [18].

The species diffusion flux for the mixture-averaged diffusion model (abbreviated by MA hereafter) is related to the species gradient by a Fickian formulation, and is expressed as

$$\mathbf{j}_i^{\mathrm{MA}} = -\rho D_{i,m} \frac{Y_i}{X_i} \nabla X_i + \rho Y_i \mathbf{u}_c \ , \tag{3.6}$$

where X_i is the ith species mole fraction, $D_{i,m}$ is the ith species mixture-averaged diffusion coefficient as expressed by Bird et al. [20]:

$$D_{i,m} = \frac{1 - Y_i}{\sum_{i \neq j}^{N} X_j / \mathcal{D}_{ji}} \ , \tag{3.7}$$

where $\mathcal{D}_{ji}$ is the binary diffusion coefficient of species i and j, and $\mathbf{u}_c$ is the correction velocity used to ensure mass continuity:

$$\mathbf{u}_c = \sum_{i}^{N} D_{i,m} \frac{Y_i}{X_i} \nabla X_i \ . \tag{3.8}$$

Alternatively, the multicomponent diffusion model (abbreviated as MC hereafter), as

presented by Bird et al. [20], calculates the species diffusion flux as

$$\mathbf{j}_i^{\mathrm{MC}} = \frac{\rho Y_i}{X_i W} \sum_{i \neq j}^{N} W_j D_{i,j} \nabla X_j \ , \tag{3.9}$$

where W is the mixture molecular weight, W_j is the molecular weight of the jth species, and $D_{i,j}$ is the ordinary multicomponent diffusion coefficient, which we compute here using the `MCMDIF` subroutine of CHEMKIN II [50] with the method outlined by Dixon–Lewis [21].

Table 3.1: Parameters of the two- and three-dimensional simulations. Δx is the grid spacing, η_u is Kolmogorov length scale in the unburnt gas, Δt is the simulation time step, ϕ is the equivalence ratio,P_0 is the thermodynamic pressure, T_u is the temperature of the unburnt mixture, T_{peak} is the temperature of peak fuel consumption rate in the one-dimensional laminar flame, S_L is the laminar flame speed, $l_F = (T_b - T_u) \,/\, |\nabla T|_{\max}$ is the laminar flame thickness, $l = u'^3/\epsilon$ is the integral length scale, u' is the turbulence fluctuations, ϵ is the turbulent energy dissipation rate, Ka_u is the Karlovitz number in the unburnt mixture, Re_t is the turbulent Reynolds number in the unburnt mixture, and ν_u is the unburnt kinematic viscosity, and A_{force} is the turbulent forcing coefficient used in NGA [15].

	H_2 (2D)		H_2		n-C_7H_{16}		$C_6H_5CH_3$	
	MA	MC	MA	MC	MA	MC	MA	MC
Domain	$4L \times L$		$8L \times L \times L$		$11L \times L \times L$		$11L \times L \times L$	
L	$472\Delta x$		$190\Delta x$		$128\Delta x$		$128\Delta x$	
Grid	1888×472		$1520 \times 190 \times 190$		$1408 \times 128 \times 128$		$1408 \times 128 \times 128$	
Δx [m]	4.24×10^{-5}		4.24×10^{-5}		1.8×10^{-5}		1.8×10^{-5}	
η_u [m]	–		2.1×10^{-5}		9.0×10^{-6}		9.1×10^{-6}	
Δt [s]	5×10^{-6}		6×10^{-7}		6×10^{-7}		6×10^{-7}	
ϕ	0.4		0.4		0.9		0.9	
P_0 [atm]	1		1		1		1	
T_{u} [K]	298		298		298		298	
T_{peak} [K]	1190	1180	1190	1180	1270	1230	1420	1420
S_L [cm/s]	23.0	22.3	23.0	22.3	35.1	37.3	34.3	34.4
l_F [mm]	0.643	0.651	0.643	0.631	0.390	0.385	0.410	0.420
l/l_F	–		2	2.04	1.1		1.1	
u'/S_L	–		18	18.6	18	16.9	17	16.9
$\mathrm{Ka}_u = \tau_F/\tau_\eta$	–		149	151	220	207	200	204
$\mathrm{Re}_t = (u'l)/\nu_u$	–		289		190		175	
A_{force} [1/s]	–		973.05		4730		4333	

3.2.3 Flow configuration

We used three flow configurations in this work. The first is a one-dimensional, unstretched (flat), laminar, hydrogen/air flame with an unburnt temperature of 298 K, pressure of 1 atm, and equivalence ratio of $\phi = 0.4$. To ensure the flame remained centered in the computational domain, comprised of 720 grid points where Δx =15.4 µm, we set the inlet velocity as equal to the laminar flame speed:

$$S_L^o = -\frac{\int \rho \dot{\omega}_{\mathrm{H_2}} dx}{\rho_u Y_{\mathrm{H_2},u}} \ , \tag{3.10}$$

where ρ_u is the unburnt mixture density and $Y_{\mathrm{H_2},u}$ is the unburnt fuel mass fraction. We selected the grid spacing to ensure at least 20 points through the laminar flame, with the thickness defined using the maximum temperature gradient: $l_F = (T_{\max} - T_{\min})/|\nabla T|_{\max}$. Schlup and Blanquart [18] used an identical configuration to investigate the impact of Soret and Dufour thermal diffusion effects.

For the second and third configurations, we selected multidimensional cases where diffusion modeling may be particularly important. The second configuration considered is a two-dimensional domain used to study unsteady, freely propagating lean hydrogen/air flames [18, 23]. The third configuration is a doubly-periodic, turbulence-in-a-box configuration we used to study three-dimensional statistically stationary hydrogen/air, n-heptane/air, and toluene/air flames [18, 22, 23]. The selected fuels also span a range of Lewis numbers: $\mathrm{Le}_{\mathrm{H_2}} = 0.3$, $\mathrm{Le}_{\mathrm{C_6H_5CH_3}} = 2.5$, and $\mathrm{Le}_{\mathrm{C_7H_{16}}} = 2.8$. This allows us to evaluate if the relative strength of mass diffusivity relative to thermal diffusivity affects a flame's sensitivity to multicomponent diffusion. For example, the low Lewis number of hydrogen can result in differential diffusion effects, which cause the instabilities found in lean hydrogen/air flames. Further, we selected the turbulence timescales at the high Karlovitz numbers considered to match the order of magnitude of the diffusion time scales, such that diffusion may interact with turbulence. All three configurations have been used in previous studies, and so we provide only a brief overview here.

3.2.3.1 Two-dimensional flow configuration

The two-dimensional analysis is performed using a hydrogen/air mixture with a nine-species, 54-reaction chemistry model from Hong et al. [66–68] (forward and backward reactions are counted separately). The domain has inlet and convective outlet boundaries in the streamwise direction and periodic boundaries in the spanwise direction. The inlet velocity boundary condition is fixed at the mean effective burning velocity, such that the unstable flame remains statistically stationary in the domain. The mean effective burning velocity, S_{eff}^{2D}, is defined as

$$S_{\text{eff}}^{2D} = -\frac{\int_A \rho \dot{\omega}_{\text{H}_2} dA}{\rho_u Y_{\text{H}_2,u} L} \,, \tag{3.11}$$

where L is the spanwise dimension of the computational domain. This velocity boundary condition allows the simulation to run for an arbitrary length of time to collect statistics.

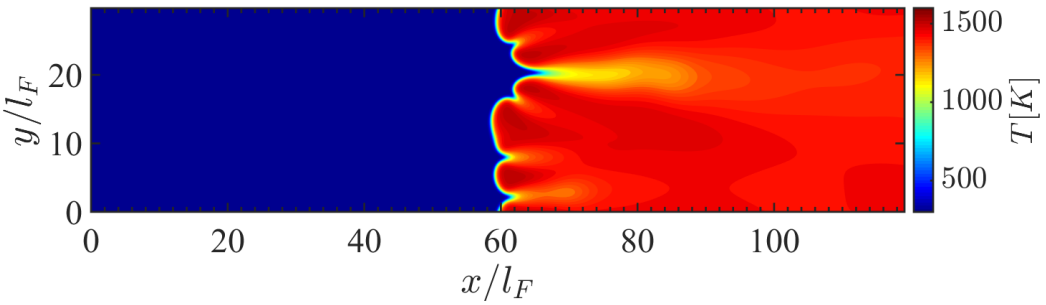

Figure 3.1: Temperature contour for the two-dimensional freely propagating unsteady hydrogen/air flame obtained with the multicomponent diffusion model.

Table 3.1 includes details of the computational domain. The unburnt mixture has an equivalence ratio of $\phi = 0.4$, unburnt temperature of $T_u = 298\,\text{K}$, and unburnt pressure of $p_o = 1\,\text{atm}$. The initial scalar and velocity figures are generated by perturbing a flat, two-dimensional flame profile, using two sinusoidal modes defined by

$$x_{F,0} = E + A \sum_{i=1,2} \cos\left(2\pi k_i \frac{y}{H}\right) \tag{3.12}$$

where $x_{F,0}$, is the initial flame position, E is the average flame position, $A = 10^{-4}\,\text{m}$ is

the amplitude, $k_1 = 20$ and $k_2 = 30$ are two coprime modes, y is the vertical coordinate, and H is the height of the domain [23]. Schlup et al. [18] and Burali et al. [23] used the same set of disturbance parameters to to initially perturb the flame asymmetrically and trigger Darrieus–Landau instabilities. Figure 3.1 shows an example temperature contour with a representative unsteady flame clearly visible.

3.2.3.2 Three-dimensional flow configuration

Three fuel/air mixtures are simulated in the three-dimensional configuration: $\phi = 0.4$ hydrogen/air, $\phi = 0.9$ *n*-heptane/air, and $\phi = 0.9$ toluene/air. The hydrogen/air mixture uses the same chemical-kinetic model as in the two-dimensional case [66–68]. The *n*-heptane/air mixture uses the reduced kinetic model described by Savard et al. [85] consisting of 35 species and 217 reactions. Finally, the toluene/air mixture uses the 47-species, 290-reaction kinetic model of Bisetti et al. [56].

Table 3.1 gives the details of the computational domains used for the three-dimensional simulations. The domains consist of inflow and convective outflow boundary conditions in the streamwise direction, and periodic boundaries in the two spanwise directions. The inflow velocity is the mean turbulent flame speed, which keeps the flame statistically stationary such that turbulent statistics can be collected over an arbitrarily long run time. In the absence of mean shear, a linear turbulence forcing method [14, 15] maintains the production of turbulent kinetic energy through the flame.

Table 3.1 also provides details on the unburnt mixture, corresponding one-dimensional flames, and inlet turbulence. The unburnt temperatures and pressures for all cases are 298 K and 1 atm, respectively. Table 3.1 gives the definitions of the Karlovitz number, Ka_u, and turbulent Reynolds number, Re_t, where $\tau_F = l_F/S_L$ is the flame time scale and $\tau_\eta = (\nu_u/\epsilon)^{1/2}$ is the Kolmogorov time scale of the incoming turbulence.

3.3 Results and discussion

This section presents a priori results for the one-dimensional flat hydrogen/air flame and two-dimensional, unsteady, premixed hydrogen/air flame, as well as a priori and a posteriori results for the three-dimensional, turbulent, premixed fuel/air flames of hydrogen, *n*-heptane, and toluene.

3.3.1 A priori diffusion flux comparison

Mass, momentum, and heat diffusion are strongly coupled processes in reacting flows, and as a result isolating the causes of observed effects can be difficult. To overcome this challenge we compared the diffusion models with an "a priori" analysis that calculates the mass-diffusion flux vectors for each method using identical scalar gradient fields. (In other words, we compare the diffusion flux vectors before any physical effects influence the flow—any observed differences later will ultimately grow from any initial differences here.) By calculating the mass diffusion fluxes in this way, we isolate the effects of the diffusion model on the resulting diffusion vectors from any time evolution of the reacting flow field. To assess disagreement between the mixture-averaged and multicomponent diffusion models, we evaluate the relative orientation and magnitude of the diffusion flux vectors they produce.

3.3.1.1 One-dimensional flame

Figure 3.2 compares the a priori diffusion fluxes for the one-dimensional, flat, hydrogen/air flame relative to the local mixture temperature. As expected, the flux profiles for the mixture-averaged and multicomponent cases match in shape and magnitude. However, the mixture-averaged model underpredicts the maximum flux magnitude for the hydrogen radical (H) by approximately 40 %. Similarly, the mixture-averaged model underpredicts molecular hydrogen and (H_2) and hydroxyl radical OH fluxes by approximately 18 %, and the oxygen radical (O) by 16 %. These differences are substantial but agree with previous results for one-dimensional premixed hydrogen/air flames [31, 42].

These errors disrupt mass continuity by locally altering the equivalence ratio in regions of high mass-diffusion flux. This effect is clear when considering the correction velocity, which is based on the mole and mass fractions of the species. As a result, it lumps a large portion of the correction for mass continuity into the N_2 mass flux, which the mixture-averaged model overpredicts by 40 %. The correction velocity is not correcting for the errors in the mixture-averaged model; rather, it simply ensures mass continuity is maintained despite the errors.

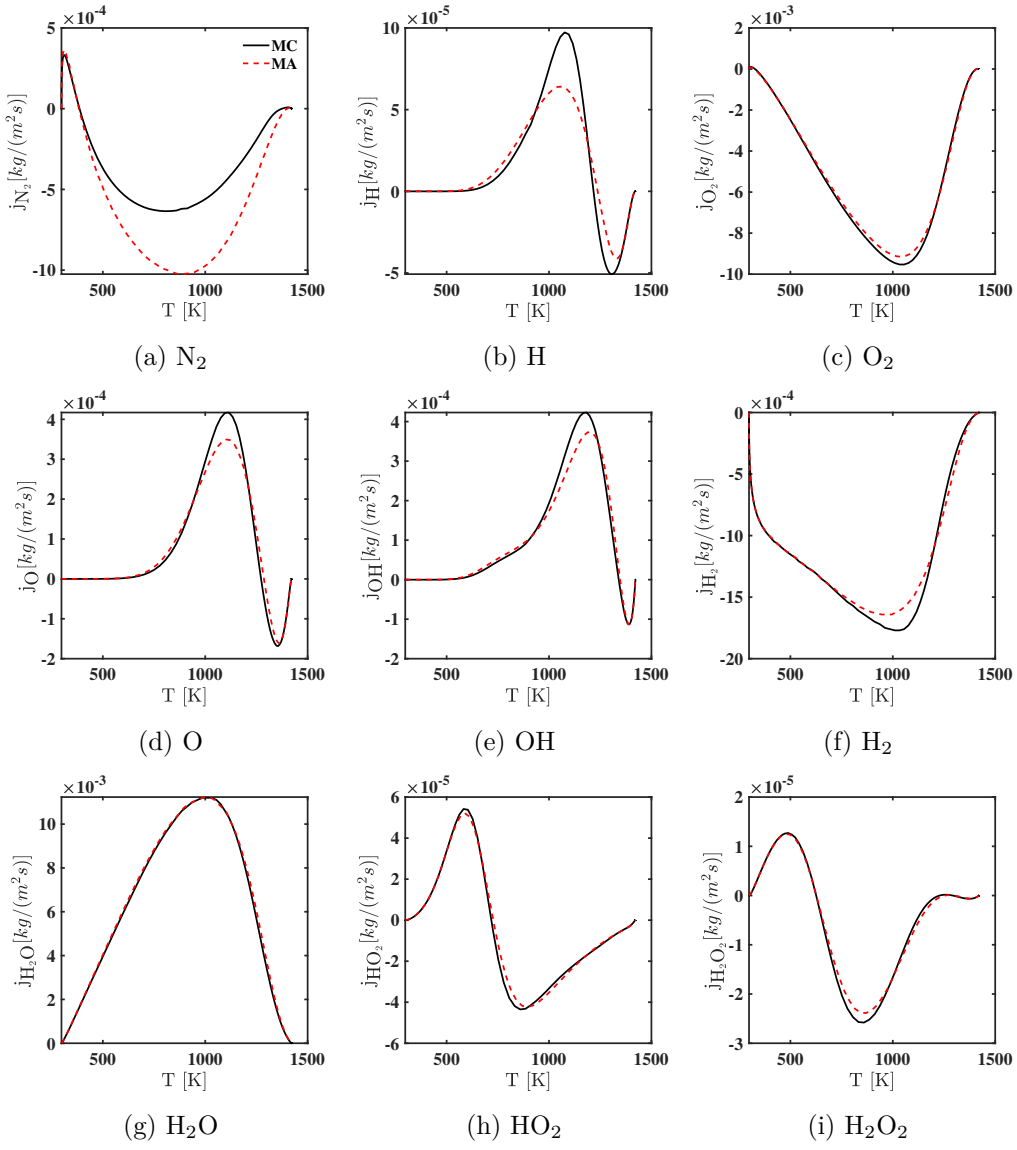

Figure 3.2: A priori comparisons of mass diffusion fluxes relative to mixture local temperature in a one-dimensional hydrogen/air flame at $\phi = 0.4$.

3.3.1.2 Multi-dimensional flames

We next performed an a priori assessment of the species mass diffusion fluxes in the multi-dimensional flames. However, because of the added degrees-of-freedom in multi-dimensional flows, we now investigate the relative angles of the flux vectors with respect to the species gradient vector to assess the relative direction of mass flux, in addition to the flux magnitudes. As demonstrated in Eq. (3.7), the mixture-averaged flux vector for a given species is based on the gradient of that species and, as a result, should be strictly anti-parallel to its gradient. In contrast, in Eq. (3.9), the multicomponent flux of a given species is based on the net influence of the remaining species (but not itself) and thus may not necessarily align with its own gradient. Differential diffusion may misalign the species gradient and multicomponent diffusion flux vectors in regions of high flame curvature where strong gradients can exist in multiple directions.

As a qualitative assessment, Figure 3.3 shows two-dimensional slices of fuel mass fraction, fuel mass diffusion flux, and flux-vector angle relative the species gradient vector from the turbulent hydrogen/air flame for the mixture-averaged and multicomponent models. For this assessment an angle of π corresponds to alignment between the flux and species gradient vectors while smaller angles show misalignment. To help highlight small scale differences between the two diffusion models, we also present the log of the mass diffusion flux field. The location of the flame is indicated by isolines of $T = T_{\text{peak}} - 300\,\text{K}$ (red) and $T = T_{\text{peak}} + 300\,\text{K}$ (white) included on the fields of fuel mass fraction.

Qualitatively, the angles shown in Figures 3.3g and 3.3h are in good agreement between the mixture-averaged and multicomponent models. At the far left of both figures the relative angle is zero at the inlet of the domain. In this region fuel has not been consumed and so the fuel mass fraction is approximately constant and gradients are small; as a result the magnitude of the mass flux in this region is at or near zero. This is confirmed by Figures 3.3e and 3.3f where values of $\log_{10}(\text{j}_{\text{H}_2}) \leq -30$ at the inlet of the domain correspond to flux magnitudes of $1 \times 10^{-30}\,\text{kg}/(\text{m}^2\,\text{s})$ or less. At the far right of Figures 3.3g and 3.3h the relative angles for both models are roughly constant and at π, anti-parallel to the species gradient vector. In this region fluxes are small but non-zero as residual fuel is present in small concentrations—as a result, scalar gradients are small. Finally, although the flux angle appears to deviate from π in small regions throughout the flame for both the mixture-averaged and multicomponent flames, these deviations

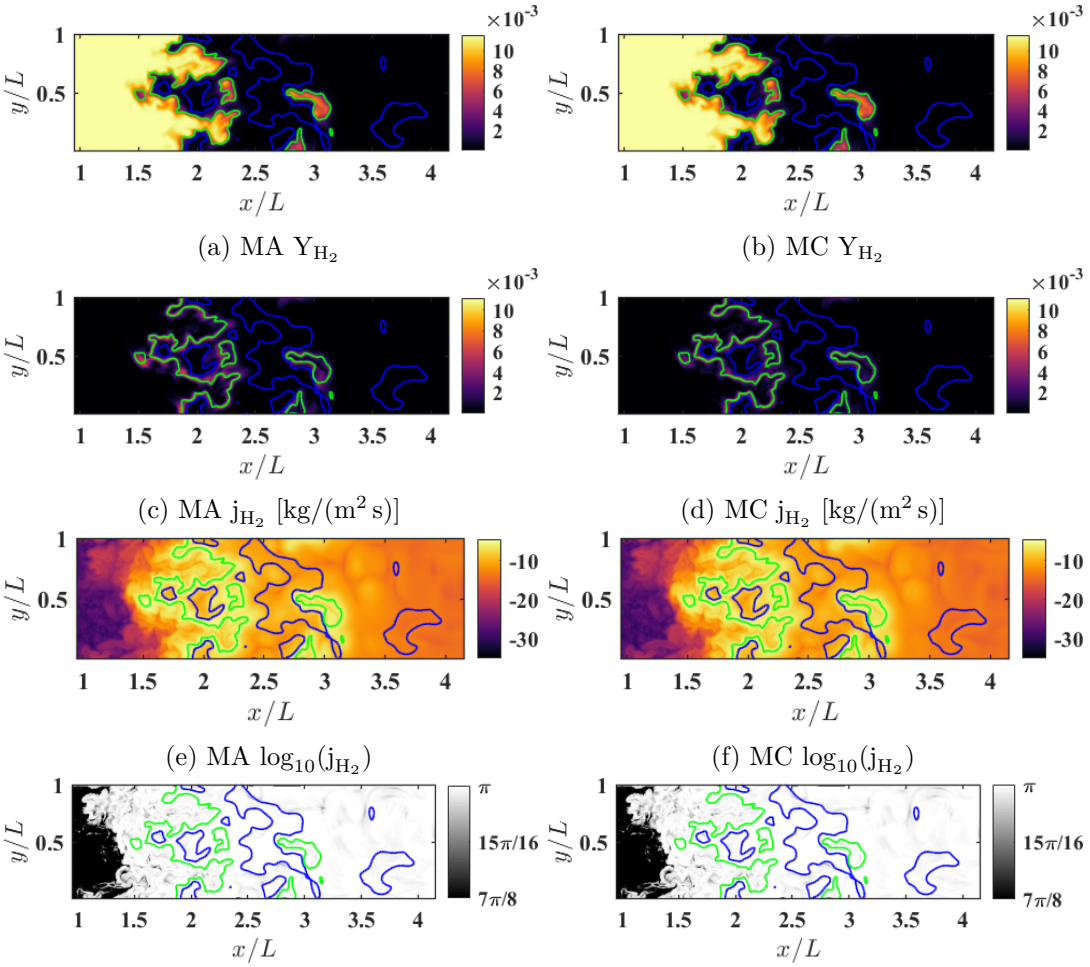

(a) MA Y_{H_2} (b) MC Y_{H_2}

(c) MA j_{H_2} [kg/(m^2 s)] (d) MC j_{H_2} [kg/(m^2 s)]

(e) MA $\log_{10}(j_{H_2})$ (f) MC $\log_{10}(j_{H_2})$

(g) MA $\nabla Y_{H_2} \angle j_{H_2}$ (h) MC $\nabla Y_{H_2} \angle j_{H_2}$

Figure 3.3: Fields of fuel mass fraction (a, b), fuel mass diffusion flux (c, d), log of the fuel mass diffusion flux (e, f), and angle between fuel mass flux and species gradient vectors (g, h) for one time step of the hydrogen-air turbulent premixed flame for the mixture-averaged (MA) and multicomponent (MC) diffusion cases. Shown are domain cross-sections through the midplane. The red and white lines correspond to isosurfaces of $T_u = T_{\text{peak}} - 300\,\text{K}$ and $T_b = T_{\text{peak}} + 300\,\text{K}$, respectively, and represent the inflow and outflow surfaces of the flame front.

correspond to areas where the flux magnitude is locally very small, approaching zero. Furthermore, the relative angle of the flux vector is consistently π in regions of high species gradients, such as through the flame front, and agrees well between the two models. The angles between the mass-flux and gradient vectors agree similarly well for all species and flame configurations considered.

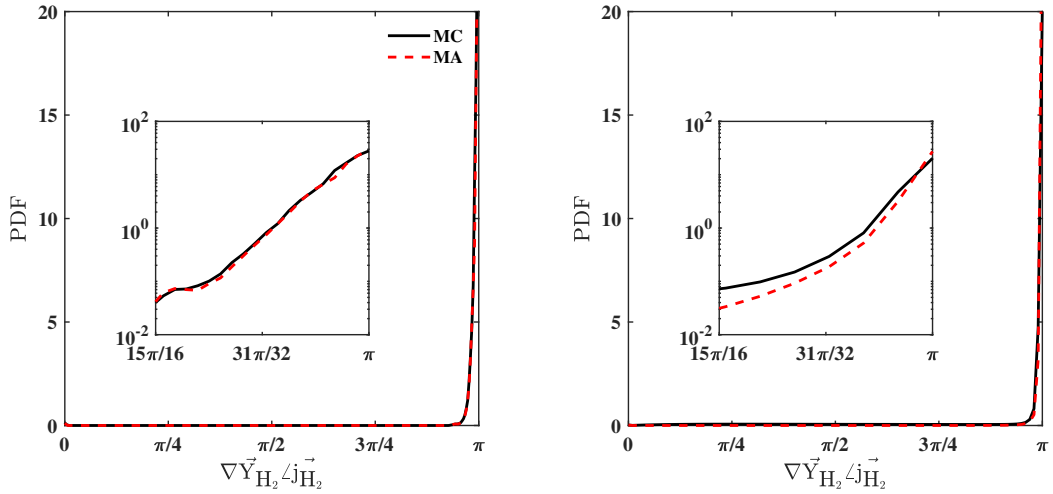

(a) Two-dimensional (b) Three-dimensional

Figure 3.4: A priori assessment of the mixture-averaged and multicomponent models comparing the PDFs of the angle between species flux vectors and species gradient vectors for the two-dimensional unsteady (a) and three-dimensional turbulent (b) hydrogen/air flames. The inset plots use a semi-log scale on the vertical axis.

To confirm our qualitative observations of the relative direction of the flux vector, Figure 3.4 shows the probability density function (PDF) of the angles between the H_2 diffusion flux vectors and the species gradient vectors for the two-dimensional unsteady and three-dimensional turbulent hydrogen flames. This quantitatively measures the alignment of the vectors to compare the multicomponent and mixture-averaged models. We only consider points in the domain for which the species diffusion flux magnitude is at least 10 % of the peak species diffusion flux magnitude, to emphasize the region where diffusion is important. For both the two- and three-dimensional hydrogen flames, both the mixture-averaged and multicomponent diffusion models have maximum PDF values

at an angle of π, anti-parallel to the species gradient vector; this is expected and indicates that mass diffusion occurs primarily in the direction of negative species gradient (i.e., from high to low concentration). We attribute small deviations of the mixture-averaged angle away from π to the velocity correction term in Eq. (3.6).

The two-dimensional unsteady flame exhibits negligible differences in the angles separating the species diffusion flux and gradient vectors; but this agreement does not extend to the three-dimensional turbulent flame. In this case, the angle PDF is roughly 50 % higher for the multicomponent model. Although this difference between the two models is large, it is tempered by the tiny magnitude of the PDFs away from π. For both cases these vectors show a clear preferential alignment at π, with the magnitude of the PDF dropping to much less than one for angles smaller than $63\pi/64$. Figure 3.5 shows that the three-dimensional turbulent n-heptane/air and toluene/air flames show similar differences.

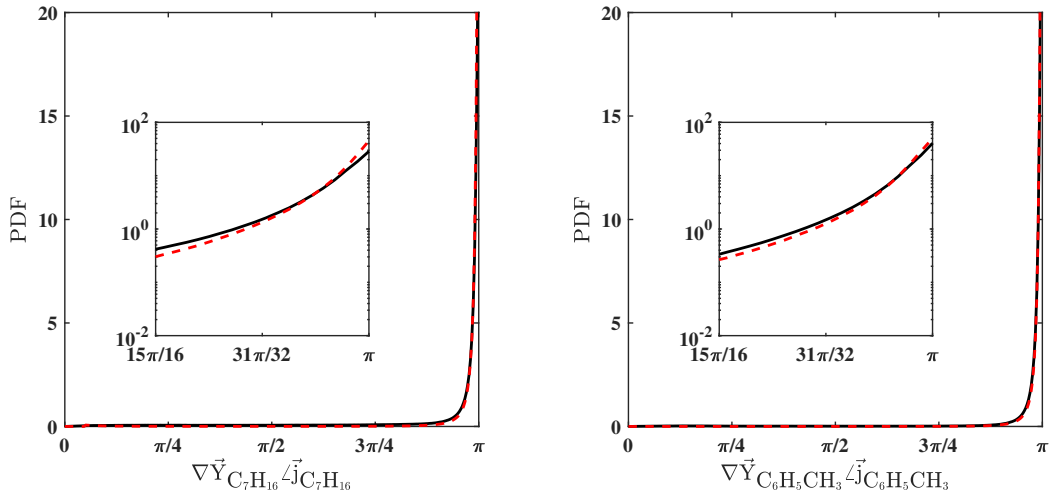

(a) n-C_7H_{16} (b) $C_6H_5CH_3$

Figure 3.5: A priori assessment of the mixture-averaged and multicomponent models comparing the PDFs of the angle between species flux vectors and species gradient vectors for the three-dimensional turbulent n-heptane/air (b) and toluene/air (a) flames. The inset plots for are semi-log scale on the y axis.

To better show where the two models deviate in the domain, Figure 3.6 presents

contours of the point-wise difference between the fuel diffusion-flux magnitudes between the models, normalized by the peak multicomponent fuel diffusion-flux magnitude. These contour plots provide a reference for the physical location of peak differences between the mixture-averaged and multicomponent models within the flame.

Examining Figure 3.6, in all cases the highest differences between the two models occur in regions of high flame curvature where the species gradient field is strong and highly variable. To more-concisely discuss these differences across multiple species and flame configurations, Table 3.2 presents the mean and standard deviations of the angles between the mixture-averaged and multicomponent diffusion fluxes, as well as relative L^1, L^2, and L^∞ error norms of the differences in magnitude of these diffusion fluxes. We calculated these statistics in regions where species diffusion is strong, i.e., the diffusion flux magnitude is greater than 10 % of the peak diffusion flux magnitude. The relative L^1, L^2, and L^∞ error norms measure the modal, mean, and maximum error, respectively, for the diffusion flux magnitude of species i and are defined as

$$L^1\left(\mathbf{j}_i^{\mathrm{MA}}\right) = \frac{\sum_{n=1}^{N_p} \left|\left|\mathbf{j}_i^{\mathrm{MA}}\right| - \left|\mathbf{j}_i^{\mathrm{MC}}\right|\right|}{\sum_{n=1}^{N_p} \left|\mathbf{j}_i^{\mathrm{MC}}\right|}\,, \tag{3.13}$$

$$L^2\left(\mathbf{j}_i^{\mathrm{MA}}\right) = \sqrt{\frac{\sum_{n=1}^{N_p} \left(\left|\mathbf{j}_i^{\mathrm{MA}}\right| - \left|\mathbf{j}_i^{\mathrm{MC}}\right|\right)^2}{\sum_{n=1}^{N_p} \left|\mathbf{j}_i^{\mathrm{MC}}\right|^2}}\,, \text{ and} \tag{3.14}$$

$$L^\infty\left(\mathbf{j}_i^{\mathrm{MA}}\right) = \frac{\sum_{n=1}^{N_p} \max\left(\left|\mathbf{j}_i^{\mathrm{MA}}\right| - \left|\mathbf{j}_i^{\mathrm{MC}}\right|\right)}{\sum_{n=1}^{N_p} \max\left(\left|\mathbf{j}_i^{\mathrm{MC}}\right|\right)}\,, \tag{3.15}$$

where N_p is the number of points in the domain.

As observed in Table 3.2, a majority of the mixture-averaged diffusion flux vectors match the multicomponent diffusion flux vectors within a mean angle, $\mu_\angle$, of 0.06 rad for the turbulent cases, with negligible differences for the two-dimensional case. The exception is the diffusion flux of H_2O for the hydrogen/air turbulent flame with a mean angle of 0.12 rad. As expected, the turbulent cases show larger (albeit still small) values of $\mu_\angle$. Additionally, the standard deviations of the angle between the diffusion fluxes, $s_\angle$, are small and generally the same order as the mean angles themselves.

Finally, Table 3.2 shows that the magnitudes of the diffusion fluxes agree well through-

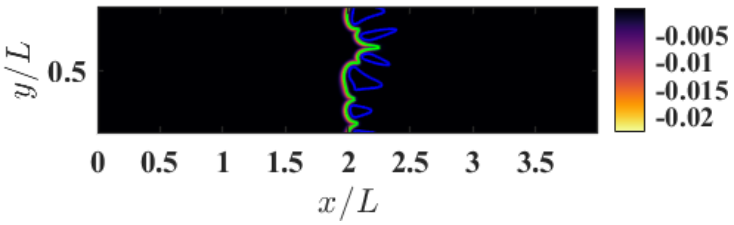

(a) Two-dimensional H_2

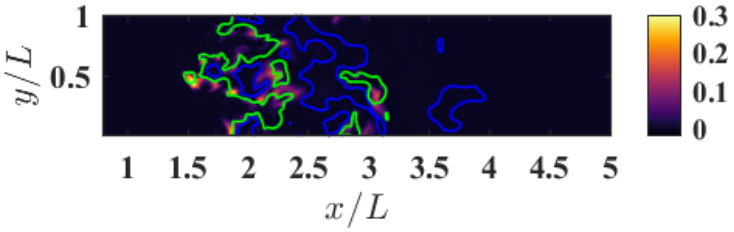

(b) Three-dimensional H_2

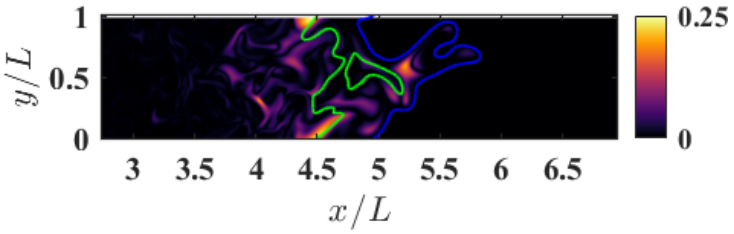

(c) n-C_7H_{16}

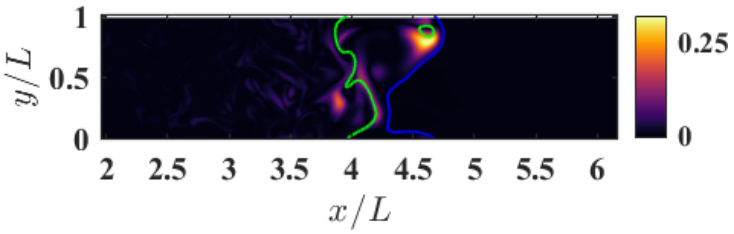

(d) $C_6H_5CH_3$

Figure 3.6: Local difference of mixture-averaged and multicomponent mass diffusion fluxes normalized by peak multicomponent mass diffusion flux, $((\mathrm{j_{MA}} - \mathrm{j_{MC}})/\max(\mathrm{j_{MC}}))$. Shown are domain cross-sections through the midplane. The red and white lines correspond to isosurfaces of $T_u = T_{\mathrm{peak}} - 300\,\mathrm{K}$ and $T_b = T_{\mathrm{peak}} + 300\,\mathrm{K}$, respectively, and represent the inflow and outflow surfaces of the flame front.

Table 3.2: Statistical quantities of the mixture-averaged and multicomponent diffusion models for a representative set of major, radical, and product species. The mean ($\mu_\angle$) and standard deviation ($s_\angle$) of the angles between the mixture-averaged and multicomponent flux vectors, as well as relative L^2 error norms (Eq. (3.14)).

	$\mu_\angle$ [rad]	$s_\angle$ [rad]	$L^1\left(\mathbf{j}_i^{\mathrm{MA}}\right)$	$L^2\left(\mathbf{j}_i^{\mathrm{MA}}\right)$	$L^\infty\left(\mathbf{j}_i^{\mathrm{MA}}\right)$
2D unsteady hydrogen					
H_2	2.7×10^{-5}	2.1×10^{-4}	2.8×10^{-2}	2.6×10^{-2}	2.2×10^{-2}
H	5.7×10^{-5}	1.4×10^{-6}	3.8×10^{-2}	3.5×10^{-2}	2.8×10^{-2}
OH	2.4×10^{-4}	3.2×10^{-5}	1.2×10^{-2}	1.0×10^{-2}	8.7×10^{-3}
H_2O	7.4×10^{-3}	2.1×10^{-4}	4.2×10^{-2}	4.0×10^{-2}	4.1×10^{-2}
3D hydrogen					
H_2	3.3×10^{-2}	7.3×10^{-2}	1.5×10^{-1}	2.1×10^{-1}	3.4×10^{-1}
H	2.5×10^{-2}	5.1×10^{-3}	1.4×10^{-1}	2.1×10^{-1}	4.2×10^{-1}
OH	7.1×10^{-4}	1.4×10^{-4}	1.6×10^{-1}	2.2×10^{-1}	4.0×10^{-1}
H_2O	1.5×10^{-1}	7.3×10^{-3}	1.8×10^{-1}	2.5×10^{-1}	4.6×10^{-1}
3D *n*-heptane					
n-C_7H_{16}	4.8×10^{-2}	4.7×10^{-2}	1.7×10^{-1}	2.2×10^{-1}	4.1×10^{-1}
H	2.7×10^{-2}	5.7×10^{-2}	1.5×10^{-1}	2.0×10^{-1}	3.9×10^{-1}
OH	6.0×10^{-2}	5.9×10^{-2}	1.7×10^{-1}	2.3×10^{-1}	4.1×10^{-1}
CO_2	4.8×10^{-3}	1.3×10^{-3}	1.5×10^{-1}	2.0×10^{-1}	3.3×10^{-1}
3D toluene					
$C_6H_5CH_3$	6.1×10^{-2}	5.1×10^{-2}	2.2×10^{-1}	2.8×10^{-1}	4.7×10^{-1}
H	1.4×10^{-2}	4.8×10^{-2}	1.8×10^{-1}	2.5×10^{-1}	4.0×10^{-1}
OH	8.6×10^{-3}	2.7×10^{-2}	2.1×10^{-1}	2.7×10^{-1}	4.6×10^{-1}
CO_2	5.9×10^{-3}	2.6×10^{-3}	2.0×10^{-1}	2.5×10^{-1}	3.9×10^{-1}

out much of the domain. The L^2 error norms indicate the average error in the mixture-averaged flux magnitude is on the order of 20 %. However, by definition, the L^2 error norm weights outliers most heavily and so skews the error high. Alternatively, the L^1 error norm weights all points in the domain equally providing a measure of the modal error. Comparing these two values, we can see the error is less than 20 % throughout the domain for most species, with the largest errors occurring in the three-dimensional flame configurations. Finally, examining the L^∞ error norms, the observed differences in Figure 3.6 correspond to large relative errors, on the order of 30–50 % in regions of high flame curvature for each of the three-dimensional flame configurations. The largest errors occur in the *n*-heptane/air and toluene/air flames.

The differences between the two models seem to increase proportionally to the magnitude of the driving species gradient. In Figure 3.6a, showing the lean, two-dimensional, unsteady, laminar, hydrogen/air flame, the mixture-averaged model matches the multicomponent model within 2 percent for the full domain. For this two-dimensional case the species gradient vectors are primarily aligned in the flow-wise direction and roughly constant across the domain. As a result, the scalar gradient fields locally vary a small amount and the mixture-averaged diffusion model matches the multicomponent model well; this is true even near thermal instabilities. In contrast, the lean, three-dimensional, turbulent hydrogen air flame shows significantly larger differences between the models. The equivalence ratio between these two flames matches ($\phi = 0.4$) and so any local increases in the species gradient field are due to an increase in local flame curvature caused by turbulent mixing. In these regions of high-flame curvature, the scalar gradient field is steep, highly variable, and not strictly aligned in the flow-wise direction, and, as a result, mass diffusion may occur in multiple directions. Comparing the definitions of the mixture-averaged and multicomponent diffusion fluxes in Eq. (3.6) and Eq. (3.9), respectively, the strict alignment of the mixture-averaged diffusion flux with its own gradient may overvalue the impact of that gradient and overpredict the mass flux when the gradient vector is large, such as in regions of high flame curvature.

This overprediction of the mixture-averaged diffusion flux is most evident in the turbulent, *n*-heptane/air and toluene/air flames where, in addition to turbulent mixing, the equivalence ratio is much higher at $\phi = 0.9$. Although it is difficult to compare these flames one-to-one due to differences in chemistry, the increased equivalence ratio relative to the lean hydrogen/air flames will result in steeper species gradients through the flame,

since the unburnt fuel mass fractions are much higher in these flames: 0.056 and 0.063 for n-heptane/air and toluene/air, respectively, compared with 0.012 for hydrogen/air. This increase in the unburnt fuel mass fraction, coupled with the presence of turbulent mixing, will increase the magnitude of the species gradients through the flame front relative to the three-dimensional hydrogen flame. Furthermore, the increases in error for the n-heptane and toluene flames over the hydrogen/air flames supports the theory that high species gradients can lead to the mixture-averaged model overpredicting diffusion flux.

Finally, although the reported errors in the predicted flux magnitudes for the mixture-averaged over the multicomponent model may seem significant, it is important to examine these values from the perspective of turbulent scaling. The relative magnitude of both the mixture-averaged and multicomponent mass diffusion fluxes are small: on the order of $5 \times 10^{-3}\,\mathrm{kg/(m^2\,s)}$ or smaller on average for all four simulations, compared to total mass fluxes on the order of $1\,\mathrm{kg/(m^2\,s)}$ or greater. Moreover, the multicomponent and mixture-averaged fluxes consistently show the same order of magnitude for a given species in a point-wise comparison, for most points in the domain. In other words, when comparing any given point in the domain, the expected fluxes for the mixture-averaged and multicomponent fluxes are equivalent from an order of magnitude perspective. This suggests that the over prediction in the mixture-averaged flux calculation may be negligible in comparison to global turbulent flame statistics.

3.3.2 A posteriori comparison of turbulent statistics

To further compare the mixture-averaged and multicomponent diffusion models, we present a posteriori statistics for the three turbulent flame simulations using both mixture-averaged and multicomponent diffusion. In other words, how much does model choice impact global and statistical quantities in a simulation? For this analysis, we allowed the flames to develop in a turbulent flowfield, and computed statistics after removing the initial transients of the input flow and scalar fields. We ran each simulation for at least 20 eddy turnover times ($\tau_{\mathrm{eddy}} = k/\epsilon$ where k is the turbulent kinetic energy) to collect turbulent statistics[1].

[1] In practice we determine τ_{eddy} with the turbulence forcing scheme: $\tau_{\mathrm{eddy}} = 1/2A_{\mathrm{force}}$, where A_{force} is the turbulent forcing coefficient imposed as a parameter in the simulation and developed by Carroll et al. [15].

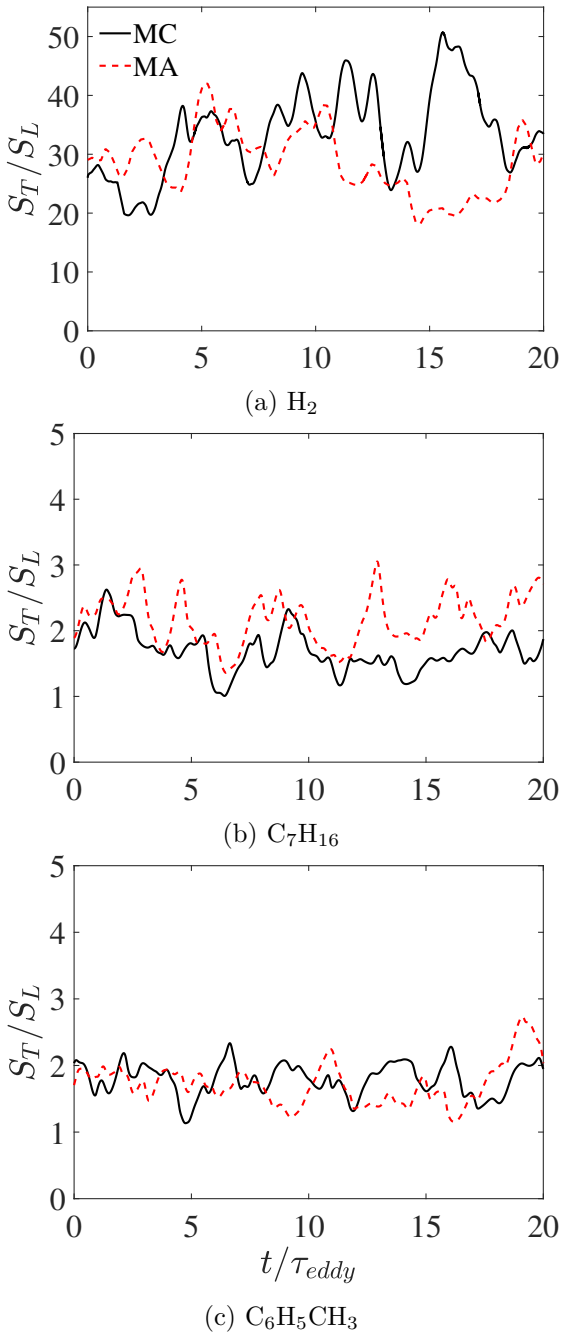

(a) H_2

(b) C_7H_{16}

(c) $C_6H_5CH_3$

Figure 3.7: Time-history of the normalized turbulent flame speed from the turbulent hydrogen/air configuration for both diffusion models.

Figure 3.7 shows the time-history of the turbulent flame speed, S_T, normalized by S_L, defined as

$$S_T = \frac{\int_V \rho \dot{\omega}_{\mathrm{F}}\, dV}{\rho_u Y_{\mathrm{F},u} L} \,, \tag{3.16}$$

where $\omega_{\mathrm{H_2}}$ and Y_F are the fuel source term and mass fraction respectively, rho is the density, L is the span-wise domain width, and V is the volume of the domain. We started the multicomponent and mixture-averaged diffusion models from the same initial data file, and allowed them to evolve in the domain until any initial transients had convected through the domain (approximately $6\tau_{\mathrm{eddy}}$). We then ran each simulation for an additional $20\tau_{\mathrm{eddy}}$ to provide a representative sample of instantaneous flame speeds. Table 3.3 presents the mean turbulent flame speeds of the three fuels, based on the collected samples. While the mixture-averaged model seems to lower the normalized turbulent flame speeds by 13 % and 5 % for the hydrogen and toluene flames, it causes a 20 % higher normalized flame speed for the n-heptane flame. These results do not seem to depend on the Lewis number for each fuel—recall that $\mathrm{Le}_{\mathrm{H_2}} = 0.3$, $\mathrm{Le}_{\mathrm{C_6H_5CH_3}} = 2.5$, and $\mathrm{Le}_{\mathrm{C_7H_{16}}} = 2.8$. The n-heptane/air and toluene/air flames have the most-similar Lewis numbers but differ in error of turbulent flame speed between the diffusion models.

Table 3.3: Mean turbulent flame speed, normalized by unstretched laminar flame speed for three-dimensional turbulent hydrogen/air, n-heptane/air, and toluene/air mixtures, comparing the impact of mixture-averaged and multicomponent diffusion models.

	MC	MA	Difference
H_2	33.9	29.6	13 %
C_7H_{16}	1.70	2.02	20 %
$C_6H_5CH_3$	1.80	1.71	5 %

To better understand the observed differences in the turbulent flame speed, we assess the impact of the diffusion models on flame chemistry via their effects on the average fuel mass fraction and source term. As demonstrated in previous studies, differential diffusion can modify the local equivalence ratio in regions of high flame curvature [3, 22, 70]. We have demonstrated this effect in Table 3.2, by showing that the mixture-averaged diffusion assumption overpredicts the magnitude of the mass diffusion flux in these regions. The increase in mass flux into these regions of high flame curvature may impact local chemistry and modify the fuel source term. Lapointe and Blanquart [22] previously suggested that the normalized turbulent flame speed is proportional to the

product of turbulent flame area and the mean source term, $\dot{\omega}_F$ conditioned on flame temperature:

$$\frac{S_T}{S_L} \propto \frac{A_T}{A} \frac{\langle \dot{\omega}_f | T \rangle}{\dot{\omega}_{F,\text{lam}}} , \tag{3.17}$$

where A_T is the turbulent flame area, A is the cross-sectional area of the domain, and $\dot{\omega}_{F,\text{lam}}$ is the fuel source term in the laminar flame. Moreover, they demonstrated that the area ratio (A_T/A) controls large-scale fluctuations in the flame speed on the order of their mean values, while the normalized mean source term ($\langle \dot{\omega}_f | T \rangle / \dot{\omega}_{F,\text{lam}}$) controls smaller-scale fluctuations [22].

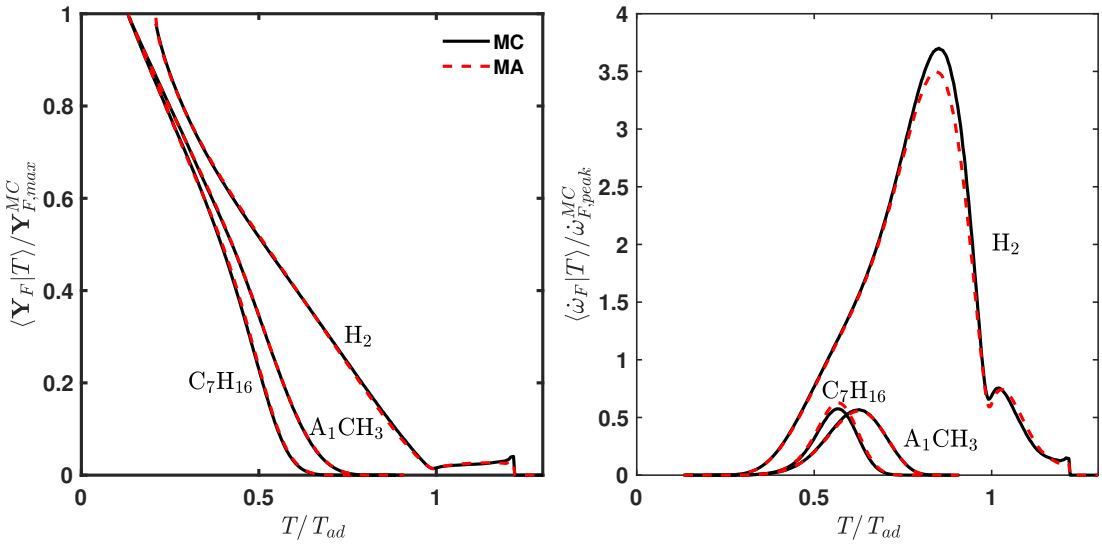

(a) Fuel mass fraction

(b) Fuel source term

Figure 3.8: Turbulent flame structure for the three fuel/air mixtures, showing conditional means of (a) fuel mass fraction and (b) source term as functions of flame temperature normalized by T_{ad}. All plots are normalized by their peak multicomponent values from one-dimensional flat flames.

To evaluate if the observed difference in the diffusion mass fluxes correlate to the observed differences in the normalized turbulent flame speeds between the two models, Figure 3.8 presents the means of the fuel mass fractions and source term, conditioned on temperature and normalized by their respective adiabatic flame temperatures of one-dimensional flames, T_{ad}. The calculated conditional means of the fuel mass fractions

differ by negligible amounts; less than 1 % at all points. This strong agreement between the conditional means of the fuel mass fraction suggests that although local differences in the diffusion mass flux fields do exist between the two models, they do not appear to significantly affect the averaged distribution of reactants in the flame.

In contrast, we observe larger differences for the conditional mean of the fuel source term in Figure 3.8b. At their peaks, the mean source terms for the multicomponent flames are 5.5 % and 1.6 % higher than the mixture-averaged models for the hydrogen and toluene flames, respectively, and 9.4 % lower for *n*-heptane flame. Moreover, away from the peak locations, the conditional means agree within 1 % for the mixture-averaged and multicomponent cases. This agreement also extends into super-adiabatic regions for the hydrogen/air flame. These super-adiabatic regions, also called "hot spots", result from differential diffusion, and have been predicted both in theoretical studies [71] and in numerical analyses of lean hydrogen/air mixtures [72–74].

Comparing the observed differences in the conditional means of the fuel source term with the mean normalized turbulent flame speeds, the results agree well with the proportional relation in Eq. (3.17) given by Lapoint and Blanquart [22]. Specifically, the peak normalized source term is 5.5 % higher for the multicomponent hydrogen/air flame over mixture-averaged, resulting in a 13 % higher normalized flame speed. Alternatively, the peak normalized source term is 9.4 % lower for the multicomponent n-heptane/air flame compared to mixture-averaged, resulting in a 19 % lower normalized flame speed. In all three cases, the error in normalized turbulent flame speed appears proportional to the error in normalized conditional mean by approximately a factor of two. This strong proportional relationship agrees with similar results observed by Lapointe and Blanquart [22]. Moreover, our results demonstrate that, relative to the multicomponent model, the observed errors in the mixture-averaged diffusion flux vectors do impact a posteriori flame statistics. These results raise questions about the appropriateness of the mixture-averaged diffusion assumption for simulations where high flame curvature is present.

3.4 Conclusions

This article compares the mixture-averaged and multicomponent mass diffusion models for premixed two-dimensional, unsteady hydrogen/air and three-dimensional, turbulent

flames, considering hydrogen, n-heptane, and toluene fuel/air mixtures. The methods are compared using both a priori and a posteriori assessments of differences. The a priori analysis indicated that the mixture-averaged model accurately reproduced the relative direction and magnitude of the flux vectors through much of the domain. However, we observed errors as high 50 % in the magnitude of the diffusion flux vector for all three fuels in regions of high flame curvature.

A posteriori analyses indicated that using the mixture-averaged model affects turbulent statistics, such as conditional means of the fuel mass fraction and consumption rates. The observed impact on a posteriori flame statistics is relatively small: the models result in differences of less than 20 % in normalized turbulent flame speed, 10 % in conditional mean of fuel source term, and 1 % in the conditional mean of fuel mass fraction. However, these errors may not fully reflect the impact of using the mixture-averaged diffusion model. Differential diffusion can modify the local species transport in regions of high flame curvature, and the large differences in mass-diffusion flux vectors may have additional impacts beyond turbulent flame speed and fuel source term. Thus, these results warrant further investigation into the appropriateness of using mixture-averaged mass diffusion in the DNS of three-dimensional, premixed turbulent flames at moderate-to-high Karlovitz numbers.

Acknowledgments

This material is based upon work supported by the National Science Foundation under Grant Nos. 1314109-DGE and CBET-1761683. This research used resources of the National Energy Research Scientific Computing Center, a DOE Office of Science User Facility supported by the Office of Science of the U.S. Department of Energy under Contract No. DE-AC02-05CH11231, as well as the Extreme Science and Engineering Discovery Environment (XSEDE), which is supported by National Science Foundation grant number ACI-1548562.

Assessing the impact of diffusion model on the turbulent transport and flame structure of premixed lean hydrogen flames

Aaron J. Fillo, Peter E. Hamlington, and Kyle E. Niemeyer

Under review

Chapter 4: Assessing the impact of diffusion model on the turbulent transport and flame structure of premixed lean hydrogen flames

Diffusion mass transport occurs at chemical and turbulent dissipation length scales in turbulent flames. Thus, multicomponent transport directly affects the dissipation and production of turbulent kinetic energy through the flame front. This study evaluates the impact of multicomponent mass diffusion on the enstrophy budget of premixed, hydrogen-air flames, neglecting secondary Soret and Dufour effects. We performed direct numerical simulations of these flames by implementing the Stefan–Maxwell equations in NGA. We simulated premixed, three-dimensional, turbulent, lean hydrogen flames using the mixture-averaged and multicomponent models. Comparing the enstrophy budgets of these simulated flames, we observed a 15 % difference in the normalized viscous dissipation term through the reaction zone, and up to a 50 % difference in super-adiabatic regions of the flame when comparing mixture-averaged and multicomponent diffusion. To assess the effect of these differences on flame structure, we reconstructed the average local internal structure of the turbulent flame through statistical analysis of the scalar gradient field. Based on this analysis, large differences in viscous dissipation seem to contribute to significant differences in the average local flame structure between the two models.

Keywords: Multicomponent diffusion; Lean hydrogen; DNS; High Karlovitz; Turbulent flame

4.1 Introduction

The average internal flame structure and statistical behavior of vorticity and enstrophy is critical to the evaluating turbulent fluid motion in reacting flows [86–88]. Heat release during the combustion process can form steep gradients in the temperature and scalar fields, increasing the importance of diffusion transport [20]. Prior studies have shown this is especially important in lean hydrogen flames where the Lewis number is much less than unity, leading to thermal-diffusive instabilities in the flame and a strong coupling of turbulence and diffusion transport [18, 72, 73, 87].

Several studies have already examined the importance of including thermal diffusion in a wide range of flame configurations [18, 30, 31, 37, 39, 72, 73, 83, 84]. These studies have thoroughly demonstrated that neglecting thermal diffusion can significantly impact flame properties. For example, studying three-dimensional, premixed, turbulent hydrogen/air flames, Schlup et al. [18] showed that thermal diffusion can increase flame propagation speeds and increase the product chemical source terms in regions of high positive curvature. Studying laminar hydrogen/air flames, Giovangigli [19] demonstrated that multicomponent Soret effects can significantly influence laminar flame speeds and extinction stretch rates for flat and stretched premixed flames, respectively. Thus, thermal diffusion is important in some fuel/air mixtures. However, while several of these studies have evaluated the impact of multicomponent thermal diffusion models on lean hydrogen flame simulations [18, 30, 31, 40, 43], we do not know the impact of full multicomponent mass diffusion on turbulent transport and average flame structure.

The primary objective of this study is to evaluate the impact of the mixture-averaged diffusion assumption on enstrophy transport and the average internal flame structure using data from direct numerical simulations (DNS) of turbulent, premixed, lean hydrogen-air flames. This objective will be achieved in two ways. First, we will analyze the differences in time- and spatially-averaged enstrophy budgets in the DNS using mixture-averaged and multicomponent diffusion models. Second, we will evaluate the impact of these differences on the average local flame structure by evaluating scalar gradient trajectories for the two models and statistically reconstructing the internal flame structures. Based on the results of these analyses, we will assess the accuracy and appropriateness of the mixture-averaged diffusion assumption for use in DNS of turbulent, premixed, lean hydrogen-air flames.

The paper is organized as follows. Section 4.2 describes the governing equations, diffusion models, and flow configuration for the simulations. Then, Section 4.3 presents, in order, an a priori qualitative analysis of the scalar and vorticity magnitude fields, the time- and spatially-averaged enstrophy budgets, and the statistical reconstruction of the average turbulent flame width. Finally, in Section 4.4 we draw conclusions from the comparisons of the diffusion models.

4.2 Numerical approach

This section describes the governing reacting-flow equations, including brief discussions of the diffusion models to be studied. We also present the three-dimensional flow configuration used.

4.2.1 Governing equations

The variable-density, low Mach number, reacting flow equations are solved using the finite-difference code NGA [33, 34]. The conservation equations are

$$\frac{\partial \rho}{\partial t} + \nabla \cdot (\rho \mathbf{u}) = 0 \,, \tag{4.1}$$

$$\frac{\partial \rho \mathbf{u}}{\partial t} + \nabla \cdot (\rho \ \mathbf{u} \otimes \mathbf{u}) = -\nabla p + \nabla \cdot \boldsymbol{\tau} + \mathbf{f} \,, \tag{4.2}$$

$$\begin{aligned} \frac{\partial \rho T}{\partial t} + \nabla \cdot (\rho \mathbf{u} T) = \nabla \cdot (\rho \alpha \nabla T) - \frac{1}{c_p} \sum_i c_{p,i} \mathbf{j}_i \cdot \nabla T \\ + \rho \dot{\omega}_T + \frac{\rho \alpha}{c_p} \nabla c_p \cdot \nabla T \,, \end{aligned} \tag{4.3}$$

$$\frac{\partial \rho Y_i}{\partial t} + \nabla \cdot (\rho \mathbf{u} Y_i) = -\nabla \cdot \mathbf{j}_i + \rho \dot{\omega}_i \,, \tag{4.4}$$

where ρ is the mixture density, $\mathbf{u}$ is the velocity, p is the hydrodynamic pressure, $\boldsymbol{\tau}$ is the viscous stress tensor, $\mathbf{f}$ represents volumetric forces, T is the temperature, α is the mixture thermal diffusivity, $c_{p,i}$ is the constant-pressure specific heat of species i, c_p is the constant-pressure specific heat of the mixture, and $\mathbf{j}_i$, Y_i , and $\dot{\omega}_i$ are the diffusion flux, mass fraction, and production rate of species i, respectively. In Eq. (4.3), the temperature source term is given by

$$\dot{\omega}_T = -c_p^{-1} \sum_i h_i(T) \dot{\omega}_i \,, \tag{4.5}$$

where $h_i(T)$ is the specific enthalpy of species i as a function of temperature. The density is determined from the ideal gas equation of state.

4.2.2 Overview of diffusion models

The diffusion fluxes are calculated using the semi-implicit scheme developed by Fillo et al. [82] with either mixture-averaged [20] or multicomponent [27] models, both of which are based on Boltzmann's equation for the kinetic theory of gases [27, 47]. This study neglects both baro-diffusion and thermal diffusion (i.e., Soret and Dufour effects). The baro-diffusion term is commonly neglected in reacting-flow simulations under the low-Mach-number approximation [48], and we neglected thermal diffusion because our objective is to investigate the impact of mass diffusion models only; Schlup et al. [18] previously explored the effects of thermal diffusion models.

The species diffusion flux for the mixture-averaged diffusion model is related to the species gradient by a Fickian formulation and is expressed as

$$\mathbf{j}_i^{\mathrm{MA}} = -\rho D_{i,m} \frac{Y_i}{X_i} \nabla X_i + \rho Y_i \mathbf{u}_c \ , \tag{4.6}$$

where X_i is the ith species mole fraction and $D_{i,m}$ is the ith species mixture-averaged diffusion coefficient expressed by Bird et al. [20] as

$$D_{i,m} = \frac{1 - Y_i}{\sum_{i \neq j}^{N} X_j / \mathcal{D}_{ji}} \ . \tag{4.7}$$

Here $\mathcal{D}_{ji}$ is the binary diffusion coefficient of species i and j and $\mathbf{u}_c$ is the correction velocity used to ensure mass continuity, given by

$$\mathbf{u}_c = \sum_i D_{i,m} \frac{Y_i}{X_i} \nabla X_i \ . \tag{4.8}$$

Alternatively, the multicomponent diffusion model for the species diffusion flux as presented by Bird et al. [20], and implemented in CHEMKIN II [50], is

$$\mathbf{j}_i^{\mathrm{MC}} = \frac{\rho Y_i}{X_i W} \sum_{i \neq j}^{N} W_j D_{i,j} \nabla X_j \ , \tag{4.9}$$

where W is the mixture molecular weight, W_j is the molecular weight of the jth species, and $D_{i,j}$ is the ordinary multicomponent diffusion coefficient computed using the `MCMDIF` subroutine of CHEMKIN II [50] with the method outlined by Dixon-Lewis [21].

Table 4.1: Parameters of the simulations, where Δx is the grid spacing, η_u is Kolmogorov length scale in the unburnt gas, Δt is the simulation time-step size, ϕ is the equivalence ratio, T_{peak} is the temperature of peak fuel consumption rate in the one-dimensional laminar flame, S_L is the laminar flame speed, $l_F = (T_b - T_u) / |\nabla T|_{\text{max}}$ is the laminar flame thickness, $l = u'^3/\epsilon$ is the integral length scale, u' is the turbulence fluctuations, ϵ is the turbulent energy dissipation rate, Ka_u is the Karlovitz number in the unburnt mixture, Re_t is the turbulent Reynolds number in the unburnt mixture, and ν_u is the unburnt kinematic viscosity.

	MA	MC
Domain	$8L \times L \times L$	
L	$190\Delta x$	
Grid	$1520 \times 190 \times 190$	
Δx [mm]	0.0424	
η_u [m]	2.1×10^{-5}	
Δt [s]	6×10^{-7}	
ϕ	0.4	
P_0 [atm]	1	
T_{u} [K]	298	
T_{peak} [K]	1190	1180
S_L [m/s]	0.230	0.223
l_F [mm]	0.643	0.631
l/l_F	2	2.04
u'/S_L	18	18.6
$\text{Ka}_u = \tau_F/\tau_\eta$	149	151
$\text{Re}_t = (u'l)/\nu_u$	289	

4.2.3 Flow configuration

We used a doubly-periodic domain to model a three-dimensional, premixed, statistically stationary lean hydrogen flame in this study [18, 22, 23]. This configuration is selected because diffusion modeling could be important in accurately simulating the instabilities found in lean hydrogen/air flames due to differential diffusion effects. Further, the turbulence timescales are of the same order of magnitude as diffusion time scales for the selected Karlovitz numbers.

The three-dimensional turbulent flames are simulated using an identical flow configuration as in previous works [18, 23, 57], and therefore only a brief description is provided. The hydrogen/air mixture uses the nine species, 54 reaction chemistry model from Hong et al. [66–68] (forward and backward reactions are counted separately).

The computational domain consists of inflow and convective outflow boundary conditions in the stream-wise direction. In the two span-wise directions, periodic boundaries are used. The inflow velocity is the mean turbulent flame speed, which keeps the flame statistically stationary such that turbulent statistics can be collected over an arbitrarily long run time. Table 4.1 also gives details of these computational domains. In the absence of mean shear, a linear turbulence forcing method [14, 15] is implemented to maintain the production of turbulent kinetic energy through the flame.

The unburnt temperatures and pressures are 298 K and 1 atm, respectively. Table 4.1 provides further details of the computational domain, unburnt mixture, corresponding one-dimensional flame statistics, and inlet turbulence. The definitions of the Karlovitz number, Ka_u, and turbulent Reynolds number, Re_t, are also given in Table 4.1, where $\tau_F = l_F/S_L$ is the flame time scale and $\tau_\eta = (\nu_u/\epsilon)^{1/2}$ is the Kolmogorov time scale of the incoming turbulence.

4.3 Results and discussion

In this section, we first present an a priori assessment of the instantaneous vector and scalar fields. Next, we present a time- and spatially averaged assessment of the enstrophy budget, followed by a statistical reconstruction of the average local flame structure.

4.3.1 A priori results

As an initial assessment of impact of mixture-averaged and multicomponent mass diffusion on flame dynamics, we presets a priori results for the simulated flames. Both simulations are initialized with the same scalar and velocity fields, and run for a single time iteration to evaluate the impact of diffusion on the scalar field, independent of turbulent mixing.

Figure 4.1 shows contours of temperature, hydrogen mass fraction, z-direction velocity, and the logarithm of the total vorticity magnitude, $\omega = [\boldsymbol{\omega} \cdot \boldsymbol{\omega}]^{1/2}$, where $\boldsymbol{\omega} = \nabla \times \mathbf{u}$. The inlet and outlet of the flame front are defined by the isosurfaces, $T_u = T_{\text{peak}} - 300\,\text{K}$ and $T_b = T_{\text{peak}} + 300\,\text{K}$, respectively, where T_{peak} is the temperature of peak fuel consumption rate in the one-dimensional laminar flame. Shown qualitatively in Fig. 4.1, the T_u isosurface is located at the transition point between the preheat and reaction zones, while the T_b isosurface captures the super-adiabatic regions, also called "hot spots", present in lean premixed hydrogen flames. These "hot spots" result from differential-diffusion effects, and have been predicted both in theoretical studies [71] and in numerical analyses of lean hydrogen/air mixtures [72–74].

As expected, the mixture-averaged and multicomponent contours exhibit little difference for a single time step. However, as shown in Fig. 4.2, if we examine the difference of the vorticity magnitude, as an indicator of the relative impact of diffusion model on turbulence transport through the flame, the two cases notably disagree even after only a single time step. Although qualitative, Fig. 4.2 highlights the impact that model selection can have on flame structure and dynamics. On average, these differences can result in a significant and measurable difference in global flame statistics.

4.3.2 Time-averaged results

To assess the impact of the observed differences on vorticity magnitude contours between the mixture-averaged and multicomponent mass diffusion models, we present an a posteriori comparison of the turbulent statistics. We allowed the flames to develop in a turbulent flow field, and computed the statistics after the initial transients of the initial flow and scalar fields had advected through the domain. The presented statistics were gathered over 25 eddy turnover times (τ) for both flames, where $\tau = k/\epsilon \approx 500\,\mu\text{s}$.

For this analysis we use enstrophy (ω^2) transport derived from the momentum equa-

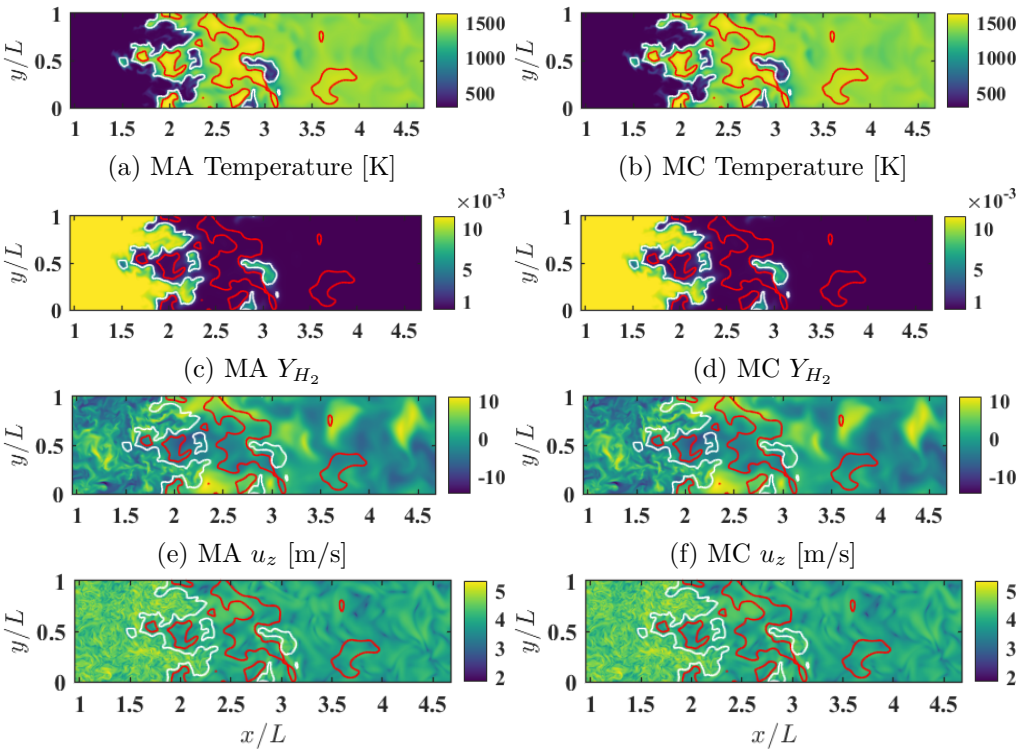

(a) MA Temperature [K]

(b) MC Temperature [K]

(c) MA Y_{H_2}

(d) MC Y_{H_2}

(e) MA u_z [m/s]

(f) MC u_z [m/s]

(g) MA $log_{10}(\omega^2)$

(h) MC $log_{10}(\omega^2)$

Figure 4.1: Fields of temperature T (a, b), fuel mass fraction (c, d), z-direction velocity u_z (e, f), and vorticity magnitude ω^2 (g, h) for one time step of the hydrogen-air turbulent premixed flame for the mixture-averaged (MA) and multicomponent (MC) diffusion cases. Shown are domain cross-sections through the midplane. The black and white lines correspond to isosurfaces of $T_u = T_{\text{peak}} - 300\,\text{K}$ and $T_b = T_{\text{peak}} + 300\,\text{K}$, respectively, and represent the inflow and outflow surfaces of the flame front.

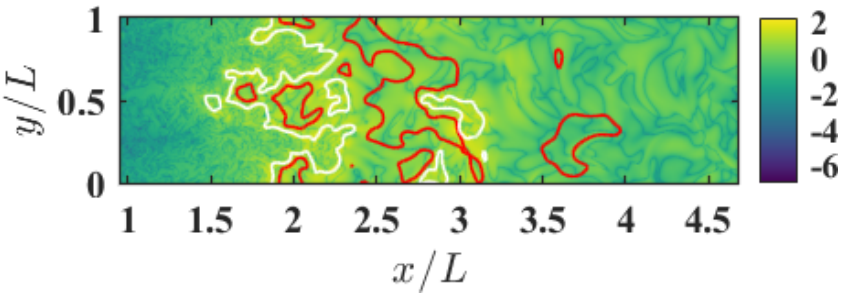

Figure 4.2: Instantaneous difference in vorticity magnitude, $\log_{10}(|\omega^2_{\mathrm{MA}} - \omega^2_{\mathrm{MC}}|)$, between the mixture-averaged and multicomponent diffusion models for a premixed, high-Karlovitz, hydrogen-air flame. Shown is the domain cross-section through the mid-plane. The black and white lines correspond to isosurfaces of $T_u = T_{\mathrm{peak}} - 300\,\mathrm{K}$ and $T_b = T_{\mathrm{peak}} + 300\,\mathrm{K}$, respectively, and represent the inflow and outflow surfaces of the flame front.

tion:

$$\frac{1}{2}\frac{D\omega^2}{Dt} = \boldsymbol{\omega}\cdot(\boldsymbol{\omega}\cdot\nabla)\mathbf{u} - \omega^2(\nabla\cdot\mathbf{u}) + \frac{\boldsymbol{\omega}}{\rho^2}\cdot(\nabla\rho\times\nabla P) + \boldsymbol{\omega}\times\left(\frac{1}{\rho}\nabla\cdot\boldsymbol{\tau}\right) + \boldsymbol{\omega}\cdot\nabla\times\frac{\mathbf{f}}{\rho}\,, \tag{4.10}$$

where $D/Dt = \partial/\partial t + \mathbf{u}\cdot\nabla$ is the material derivative, $\boldsymbol{\tau}$ is the shear force, and $\mathbf{f}$ is the turbulent forcing. Each of the terms on the right-hand side is associated with a specific physical process: vortex stretching, dilatation, baroclinic torque, viscous dissipation, and forcing, respectively. Vortex stretching, viscous dissipation, and forcing are active and constant in low-Mach number, constant-density flows, while dilatation and baroclinic torque arise due to the presence of the flame. Enstrophy can be interpreted as a potential density and measures the kinetic energy corresponding to viscous dissipation. Moreover, while constant, vortex stretching is a convective term and strongly depends on large-scale turbulent fluctuations that are largely insensitive to small-scale differences caused by differential-diffusion effects. In contrast, viscous dissipation is relatively significant throughout the flame at all times and acts at the diffusion length scales directly relevant to this study.

In its dimensional form, dissipation can vary by more than two orders of magnitude through the flame and is proportional to the inverse of the Kolmogorov time scale to the

third power. Given the turbulent cascade, the smallest scales of turbulence result in the scaling

$$\nabla \times \left(\frac{1}{\rho} \nabla \cdot \boldsymbol{\tau} \right) \propto \frac{1}{\tau_\eta^2} \,. \tag{4.11}$$

In the case of high-Karlovitz-number flows, viscous dissipation scales similarly for the enstrophy equation:

$$\boldsymbol{\omega} \cdot \nabla \times \left(\frac{1}{\rho} \nabla \cdot \boldsymbol{\tau} \right) \propto \frac{1}{\tau_\eta^3} \,. \tag{4.12}$$

The same scaling was obtained in the case of homogeneous isotropic turbulence by Tennekes and Lumley [2]. The remaining terms in the enstrophy budget scale similarly as outlined by [88].

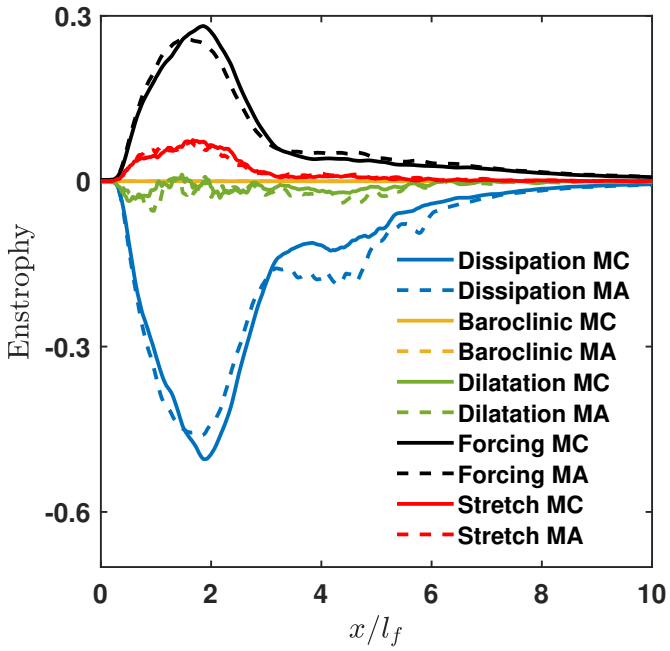

Figure 4.3: Time and spatially (spanwise) averaged enstrophy budgets for multicomponent (MC) and mixture-averaged (MA) diffusion models.

As an initial assessment, Fig. 4.3 shows the normalized time- and spatially averaged enstrophy budgets for the multicomponent and mixture-averaged simulations. Viscous dissipation acts as a significant sink term for both mixture-averaged and multicomponent diffusion cases. Vortex stretching is positive and of similar magnitude for both models,

while dilatation is non-zero and negative, consistent with previous results examining the effects of Lewis number on vorticity and enstrophy transport in turbulent premixed flames [87]. Additionally, turbulent forcing is consistent between the two cases, as expected.

Examining more closely the impact of the diffusion model on the viscous dissipation, the mixture-averaged assumption consistently under-predicts the normalized dissipation rate by as much as 10 % through the flame front when compared with multicomponent mass diffusion. This difference is most evident near the flame inlet, defined as the T_u isosurface in Figs. 4.1 and 4.2, and decreases through the reaction zone. Moreover, despite under-predicting viscous dissipation through the reaction zone, the mixture-averaged model over-predicts viscous dissipation by as much as 50 % in the super-adiabatic regions of the flame. This difference in viscous dissipation between the two diffusion models is significant and may thicken the flame in these super-adiabatic regions.

4.3.3 Flame width and reconstruction

To evaluate the impact of the observed differences in viscous dissipation on global flame structure, we reconstructed the average local internal structure of the turbulent flames. The reconstruction method used here was previously described at length by Hamlington et al. [86], and we refer the reader to that study for details.

The internal structure of the flame is connected to the magnitude of the temperature gradient, $\tilde{\chi} = [\nabla T \cdot \nabla T]^{1/2}$. Large $\tilde{\chi}$ indicates a thin flame and small $\tilde{\chi}$ indicates a broad flame [86, 89]. Correspondingly, we define $\delta_t = \tilde{\chi}^{-1}$ as the local turbulent flame width. Figure 4.4 shows that for both the mixture-averaged and multicomponent models, the presence of turbulence thins the flame overall, which is expected in the thin-flame regime. Consistent with the contours shown in Figs. 4.1 and 4.2, we define the separation between the preheat and reaction zones based on the $T_u = T + T_{\text{peak}} - 300\,\text{K}$ isosurface. Both flames have similar width in the preheat zone while the multicomponent flame is slightly thinner in the reaction zone. The value of $\langle \delta_t | T \rangle / \delta_L$ in Figure 4.4 has a second minimum at $\sim$1600 K corresponding to the super-adiabatic region of the flame. At these high temperatures the mixture-averaged flame is notably broader, consistent with the observed differences in viscous dissipation in Fig. 4.3. Values of $\langle \delta_t | T \rangle / \delta_L$ can be greater than one since $\delta_L \ (dT/dx)^{-1}_{L,max}$ corresponds to the minimum local width of the laminar

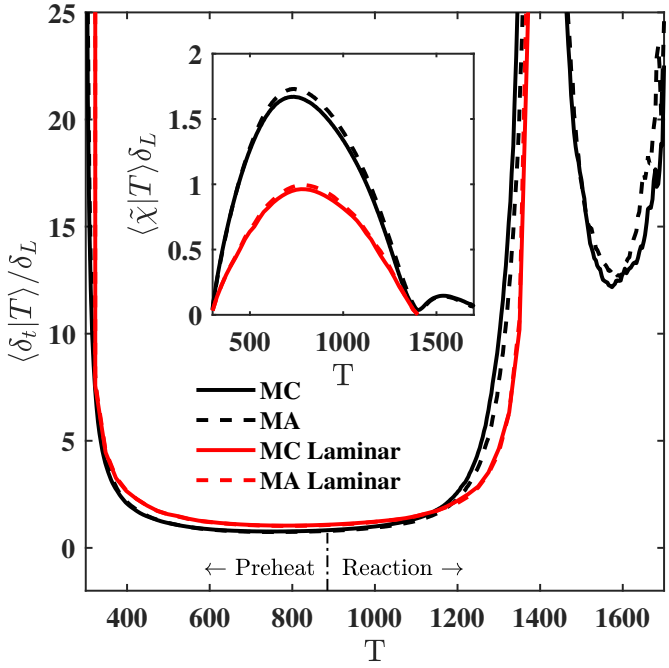

Figure 4.4: Conditional means of the local flame width $\langle \delta_t | T \rangle \equiv \langle \tilde{\chi}^{-1} | T \rangle$ normalized using the laminar flame thickness, δ_L. The inset shows $\langle \tilde{\chi} | T \rangle$ normalized by δ_L.

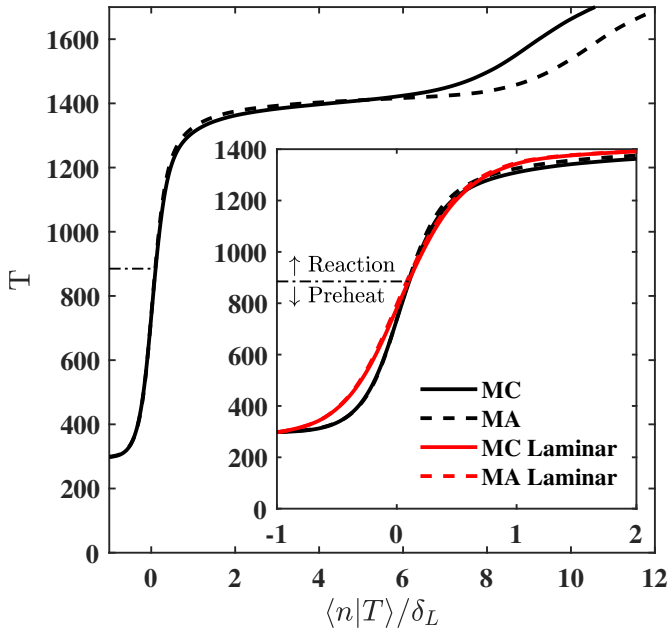

Figure 4.5: Average local flame structure reconstructed using $\langle\tilde{\chi}^{-1}|T\rangle$ from Fig. 4.4 and Eq. (4.13) for the turbulent and laminar flames with multicomponent and mixture-averaged mass diffusion. We chose $\langle n|T = T_{\mathrm{ref}}\rangle = 0$ in Eq. (4.13) by requiring that $\langle n|T_{\mathrm{ref}}\rangle/\delta L = 0$ for all cases, where $T_{\mathrm{ref}} = T_{\mathrm{peak}} - 300\,\mathrm{K}$ and $\langle n|T\rangle/\delta L > 0$ are locations closer to reactants and $\langle n|T\rangle/\delta L < 0$ are locations closer to products. The inset highlights the flame front to facilitate comparison with the average local laminar flame structure.

flame, and both the turbulent and laminar widths exceed this at most locations.

Using the distributions of $\langle \delta_t | T \rangle$ in Fig. 4.4, we reconstruct the average local internal structure of the turbulent flames using the procedure outlined by Hamlington et al. [86]. The average flame-normal coordinate, $\langle n | T \rangle$, is calculated from $\langle \tilde{\chi}^{-1} | T \rangle / \delta_L$ as

$$\langle n | T \rangle = \langle n | T = T_{\text{ref}} \rangle + \int_0^T \langle \tilde{\chi}^{-1} | \eta \rangle d\eta \, , \tag{4.13}$$

where $\langle n | T = T_{\text{ref}} \rangle$ is the location corresponding to $T_{\text{ref}} = T_{\text{peak}} - 300\,\text{K}$, taken as the transition between the preheat and reaction zones for the present flames. Integration of Eq. (4.13) gives profiles of T as a function of $\langle n | T \rangle$, which approximate the internal structure of the turbulent flame.

The resulting profiles in Fig. 4.5 show that the preheat zone thins for the turbulent flames and confirms that the multicomponent flame is slightly broader in the reaction zone. Moreover, Fig. 4.5 shows the super-adiabatic regions of the mixture-averaged flame are as much as 18 % broader than in the multicomponent flame. This large difference in flame structure indicates that mixture-averaged diffusion may not fully capture the complex interaction between diffusion and turbulent transport in high-temperature regions of the flame where steep gradients in the scalar field are present.

4.4 Conclusions

In the present study, we assessed the impact of mixture-averaged and multicomponent species diffusion models on turbulent dissipation and average local flame structure for three-dimensional, premixed, high-Karlovitz, lean hydrogen air flames. We observed small differences, (i.e. differences of 20 % or less) when comparing the total vorticity magnitude for the two flames, suggesting that the mixture-averaged diffusion assumption may not fully model the physical mass transport of the full multicomponent case.

Additional time- and spatially averaged analyses of the enstrophy transport equation in both flames demonstrated significant differences in viscous dissipation between the two models. Specifically, we observed a 50 % difference in the viscous dissipation term of the enstrophy budget between the super-adiabatic regions of the mixture-averaged and multicomponent flames. This large difference seems to contribute to significant broadening of the mixture-averaged flame relative to the multicomponent flame in these

regions. Thus, although the mixture-averaged diffusion model may adequately reproduce full multicomponent mass diffusion in the preheat and reaction zones, it may fail to appropriately model mass transport in high-temperature, thermally unstable regions of the flame.

4.5 Acknowledgements

This material is based upon work supported by the National Science Foundation under Grant Nos. 1314109-DGE and CBET-1761683. This research used resources of the National Energy Research Scientific Computing Center, a DOE Office of Science User Facility supported by the Office of Science of the U.S. Department of Energy under Contract No. DE-AC02-05CH11231.

Chapter 5: Conclusions

This chapter briefly summarizes the proposed numerical algorithm and results reported in this study. The summary focuses on overall trends and differences observed between the mixture-averaged and multicomponent diffusion models for the three studies presented. The chapter finishes with a discussion of the general conclusions reached and highlight their significance to the broader combustion and computational fluid dynamics communities.

5.1 Summary of Results

This dissertation presents a fast, memory-efficient, and stable semi-implicit scheme for implementing multicomponent mass diffusion in reacting-flow DNS. I show the proposed method to be second-order accurate in time, and verify it against one-dimensional premixed, flat, laminar hydrogen flames simulated in Cantera. The proposed scheme is computationally cost-efficient for chemical kinetic models of up to 100 species. Moreover, as demonstrated in Chapter 3, the proposed method is only marginally more expensive than the mixture-averaged diffusion model and its performance could be further improved by replacing the CHEMKIN II [50] call with a more-efficient method for calculating the multicomponent diffusion coefficient matrix.

Using the proposed multicomponent algorithm, Chapter 3 compares the relative impact and accuracy of the mixture-averaged diffusion model against the multicomponent mass diffusion model for premixed two-dimensional, unsteady hydrogen/air and three-dimensional, turbulent flames, considering hydrogen, n-heptane, and toluene fuel/air mixtures. Comparing the relative angle of the flux vectors produced by the two models to their respective species gradient vectors, the mixture-averaged diffusion model accurately reproduces the relative direction of diffusion for a wide range of chemical species and flame configurations. However, when comparing the magnitudes of the flux vectors, I observed average errors on the order of 20 % for the mixture-averaged model relative to multicomponent diffusion. Furthermore, I observed peak errors on the order of 30–

50 % for the turbulent flames at moderate to high Karlovitz numbers (i.e., Ka $\geq$ 150). Evaluating the impact of these differences on the a posteriori global flame statistics such as the turbulent flame speed and mean fuel source term, the observed errors in mixture-averaged diffusion appear to cause up to 20 % difference in the normalized turbulent flame speed and up to 10 % difference in the conditional means of fuel source term for the three turbulent flames considered.

Chapter 4 assesses the impact of the mixture-averaged and multicomponent diffusion models on the turbulent transport and local flame structure in three-dimensional, premixed, lean, high-Karlovitz hydrogen/air flames. I observed small differences of 20 % or less when comparing fields of vorticity magnitude, even after only one time-step. Comparing the time- and spatially-averaged enstrophy transport between the two models, mixture-averaged underpredicts viscous dissipation in the reaction zone by 10 % and overpredicts viscous dissipation by as high as 50 % in super-adiabatic regions of the flame when compared to the multicomponent model. Evaluating the impact of these difference on the local average flame structure, the observed differences in viscous dissipation seems to contribute to a 5 % difference in the conditional means of local flame width. These minor differences in local flame transport correspond to thinning of the average flame structure in the reaction zone and significant broadening of the average flame structure, on the order of 18 %, in the super-adiabatic regions of the mixture-averaged flame.

5.2 Conclusions

The proposed algorithm successfully reduces the computational and memory costs associated with implementing full multicomponent mass diffusion in reacting-flow DNS. This algorithm enabled a thorough assessment of the accuracy and appropriateness of the mixture-averaged diffusion approximation against full multicomponent mass diffusion for a wide range of fuels and flame configurations. Based on the results of that assessment, I reached four primary conclusions:

1. Mixture-averaged diffusion results in significant errors—as high as 50 %—in the magnitude of diffusion flux vectors produced in regions of high flame curvature. As shown in Equation (2.7), the mixture-averaged diffusion flux is strictly defined by its own species gradient. Alternatively, as shown in Equation (2.11) the multicomponent flux depends on the sum of the remaining species gradients. In regions of

high flame curvature the species gradients are steep and locally vary. The strict alignment of the mixture-averaged diffusion flux with its own gradient may overvalue the impact of that gradient and, as a result, overpredict mass flux in these regions.

2. Mixture-averaged diffusion alters the turbulent flame speed by modifying the averaged fuel source term for flames in the moderate-to-high Karlovitz number regime. As demonstrated, the mixture-averaged model overpredicts mass diffusion fluxes in regions of high flame curvature. These overpredictions increase fuel mass transport, locally modifying the equivalence ratio in such regions and resulting in small-scale changes in the average fuel source term. These differences in the averaged fuel source term may affect flame dynamics sufficiently to impact the turbulent flame speed by increasing or decreasing fuel consumption rates, depending on the fuel.

3. Mixture-averaged diffusion significantly impacts viscous dissipation of lean, premixed, high Karlovitz number hydrogen/air flames. The observed differences in viscous dissipation are attributed to overprediction by the mixture-averaged model in regions of high flame curvature. Mass and momentum transport through a flame are coupled, and, as a result, increased mass transport through the flame front may also increase the transport of turbulent kinetic energy. This is consistent with the observed decrease in viscous dissipation in the reaction zone and subsequent increase in viscous dissipation in super-adiabatic regions of the flame. It is plausible that increased mass flux into super-adiabatic regions of the flame caused by overprediction of the mixture-averaged model causes a similar overprediction of turbulent kinetic energy transport into these regions, effectively re-distributing viscous dissipation in the domain.

4. Mixture-averaged diffusion results in significant flame broadening in super-adiabatic regions of the flame. This is attributed to increased mass and momentum flux into these regions, consistent with the observed differences in viscous dissipation between the mixture-averaged and multicomponent flames. At small-enough length scales, turbulence can lead to flame broadening by locally impacting the internal flame structure and increasing turbulent dissipation. Increased mass and momentum flux into these super-adiabatic regions may increase both the local concentration of fuel

and turbulent kinetic energy within the flame, causing the flame to broaden to maintain momentum and species conservation.

Overall, my findings raise questions on the accuracy and appropriateness of the mixture-averaged diffusion assumption in DNS of three-dimensional, premixed, turbulent flames at moderate-to-high Karlovitz numbers (i.e., Ka $\geq$ 150). However, these results are limited in their scope and as such additional study is needed to fully evaluate the limitations of the mixture-averaged diffusion assumption.

5.3 Significance and Future work

This dissertation presents a novel method for implementing full multicomponent mass diffusion efficiently in DNS of reacting flows. This method can be adapted to a wide range of finite-difference solvers to facilitate further investigation on the impact of multicomponent mass diffusion regardless of flow configurations. Moreover, the proposed low-memory algorithm has broad applications in finite-differences methods beyond numerical combustion. The method "simply" rearranges the floating-point operations in a memory-efficient way and does not alter the underlying mathematics, and can be applied to any finite-difference scheme to reduce memory requirements and improve efficiency. However, it is most applicable to high-order finite-difference schemes with large stencil sizes, which can be prone to cache misses and as a result would benefit from reduced calls to memory.

To fully take advantage of the efficiency of the presented method, future work should focus on integrating this code with an improved method for calculating the multicomponent diffusion coefficient matrix, such as EGlib [29]. While I have already demonstrated the presented method is only marginally more expensive than mixture-averaged diffusion schemes, calculating the diffusion coefficient matrix faster would sufficiently speed up the code so that multicomponent diffusion would cost nearly the same as mixture-averaged diffusion.

This dissertation also presents the first assessment of the accuracy and appropriateness of mixture-averaged diffusion for use in DNS of reacting flows. Moreover, my results suggest that the mixture-averaged diffusion model may not be appropriate for the DNS of turbulent flames in the moderate-to-high Karlovitz number regime. The large errors observed in the mixture-averaged diffusion fluxes clearly impact local mass transport,

resulting in fundamental changes to the local flame structure. While these results do not invalidate previous studies using the mixture-averaged diffusion assumption, they do warrant further investigation and re-evaluation of previous mixture-averaged results. These future efforts should focus on:

1. Improving our understanding of the interaction between mass diffusion and chemistry in turbulent, premixed flames. While turbulence-chemistry interaction has been studied for years, diffusion assessments have been limited to Lewis number comparisons evaluating the relative impact of thermal and mass diffusion. However, my results indicate that flames with similar turbulence and fuel Lewis numbers (i.e., *n*-heptane and toluene) may have different sensitivities to differential diffusion. These differences suggest additional sensitivities to fuel reactivity and small-scale interaction between mass diffusion and chemistry and warrant further investigation.

2. Evaluating the impact of full multicomponent mass diffusion on rich turbulent premixed and turbulent non-premixed flames. My results demonstrate that differential mass diffusion may be important for turbulent premixed flames where mass diffusion effects are small relative to large-scale turbulent transport. Similar or larger sensitivities may be observed in flames where mass diffusion dominates more, such as in rich premixed and non-premixed flames. Additionally, using the proposed method to investigate these flames in detail may provide insight on the impact of mass diffusion on chemistry.

3. Implementing the presented memory algorithm to improve additional aspects of DNS. While the presented semi-implicit preconditioning scheme is limited to diffusion, the memory algorithm has wide applications in evaluating differential equations in numerical simulations. Implementing this method throughout a finite difference code could reduce the costs associated with DNS and other simulations, and facilitate the simulation of larger or more complex flames.

Finally, in light of the computational efficiency of the proposed method, these conclusions raise questions on the continued use of the mixture-averaged and other diffusion assumptions for the DNS of reacting flows.

Bibliography

[1] SB Pope, *Turbulent flows* (Cambridge University Press, Cambridge, UK, 2000).

[2] H Tennekes and JL Lumley, *A first course in turbulence* (MIT Press, Cambridge, Massachusetts, USA, 1972).

[3] N Peters, *Turbulent combustion* (Cambridge University Press, Cambridge, UK, Aug. 2001).

[4] CK Law, "Combustion at a crossroads: status and prospects", Proceedings of the Combustion Institute **31**, 1–29 (2007) 10.1016/j.proci.2006.08.124.

[5] W Yuan, Y Li, and F Qi, "Challenges and perspectives of combustion chemistry research", Science China Chemistry **60**, 1391–1401 (2017) 10.1007/s11426-017-9066-9.

[6] F Egolfopoulos, N Hansen, Y Ju, K Kohse-Höinghaus, C Law, and F Qi, "Advances and challenges in laminar flame experiments and implications for combustion chemistry", Progress in Energy and Combustion Science **43**, 36–67 (2014) 10.1016/j.pecs.2014.04.004.

[7] AJ Fillo, "The Global Consumption Speeds of Premixed Large-Hydrocarbon Fuel/Air Turbulent Bunsen Flames", https://ir.library.oregonstate.edu/concern/graduate_thesis_or_dissertations/1544br581, MS Thesis (Oregon State University, 2016).

[8] ER Hawkes, R Sankaran, JC Sutherland, and JH Chen, "Direct numerical simulation of turbulent combustion: fundamental insights towards predictive models", Journal of Physics: Conference Series **16**, 65–79 (2005) 10.1088/1742-6596/16/1/009.

[9] T Poinsot, S Candel, and A Trouvé, "Applications of direct numerical simulation to premixed turbulent combustion", Progress in Energy and Combustion Science **21**, 531–576 (1995) 10.1016/0360-1285(95)00011-9.

[10] P Moin and K Mahesh, "Direct numerical simulation: a tool in turbulence research", Annual Review of Fluid Mechanics **30**, 539–578 (1998) 10.1146/annurev.fluid.30.1.539.

[11] A Abbà, A Cercignani, and L Valdettaro, "Analysis of subgrid scale models", Computers and Mathematics with Applications **46**, Turbulence Modelling and Simulation, 521–535 (2003) https://doi.org/10.1016/S0898-1221(03)90014-9.

[12] MP Martín and GV Candler, "Subgrid-scale model for the temperature fluctuations in reacting hypersonic turbulent flows", Physics of Fluids **11**, 2765–2771 (1999) 10.1063/1.870135.

[13] S Poroseva, B Kaiser, J Sillero, and S Murman, "Validation of a closing procedure for fourth-order rans turbulence models with dns data in an incompressible zero-pressure-gradient turbulent boundary layer", International Journal of Heat and Fluid Flow **56**, 71–79 (2015) 10.1016/j.ijheatfluidflow.2015.06.010.

[14] C Rosales and C Meneveau, "Linear forcing in numerical simulations of isotropic turbulence: physical space implementations and convergence properties", Physics of Fluids **17**, 095106 (2005) 10.1063/1.2047568.

[15] PL Carroll and G Blanquart, "A proposed modification to Lundgren's physical space velocity forcing method for isotropic turbulence", Phys. Fluids **25**, 105114 (2013) 10.1063/1.4826315.

[16] KE Niemeyer, CJ Sung, and MP Raju, "Skeletal mechanism generation for surrogate fuels using directed relation graph with error propagation and sensitivity analysis", Combustion and Flame **157**, 1760–1770 (2010) 10.1016/j.combustflame.2009.12.022.

[17] KE Niemeyer and CJ Sung, "Accelerating moderately stiff chemical kinetics in reactive-flow simulations using GPUs", Journal of Computational Physics **256**, 854–871 (2014) 10.1016/j.jcp.2013.09.025.

[18] J Schlup and G Blanquart, "Validation of a mixture-averaged thermal diffusion model for premixed lean hydrogen flames", Combustion Theory and Modelling **22**, 264–290 (2018) 10.1080/13647830.2017.1398350.

[19] V Giovangigli, "Multicomponent transport in laminar flames", Proceedings of the Combustion Institute **35**, 625–637 (2015) 10.1016/j.proci.2014.08.011.

[20] RB Bird, WE Stewart, and EN Lightfoot, *Transport Phenomena* (John Wiley & Sons, Inc., New York, 1960).

[21] G Dixon-Lewis, "Flame structure and flame reaction kinetics. II. transport phenomena in multicomponent systems", Proceedings of the Royal Society of London A: Mathematical, Physical and Engineering Sciences **307** (1968) 10.1098/rspa.1968.0178.

[22] S Lapointe and G Blanquart, "Fuel and chemistry effects in high Karlovitz premixed turbulent flames", Combustion and Flame **167**, 294–307 (2016) 10.1016/j.combustflame.2016.01.035.

[23] N Burali, S Lapointe, B Bobbitt, G Blanquart, and Y Xuan, "Assessment of the constant non-unity Lewis number assumption in chemically-reacting flows", Combust. Theor. Model. **20**, 632–657 (2016) 10.1080/13647830.2016.1164344.

[24] KE Niemeyer and CJ Sung, "On the importance of graph search algorithms for DRGEP-based mechanism reduction methods", Combustion and Flame **158**, 1439–1443 (2011) 10.1016/j.combustflame.2010.12.010.

[25] S Luca, AN Al-Khateeb, A Attili, and F Bisetti, "Comprehensive Validation of Skeletal Mechanism for Turbulent Premixed Methane–Air Flame Simulations", Journal of Propulsion and Power **34**, 153–160 (2018) 10.2514/1.B36528.

[26] C Law, *Combustion Physics*, 1st (Cambridge University Press, New York, 2006), pp. 84–140.

[27] JO Hirschfelder, CF Curtiss, and RB Bird, *Molecular Theory of Gases and Liquids* (Wiley, New York, 1954).

[28] T Poinsot and D Veynante, *Theoretical and numerical combustion* (RT Edwards, Inc., 2005).

[29] A Ern and V Giovangigli, "Fast and accurate multicomponent transport property evaluation", Journal of Computational Physics **120**, 105–116 (1995) 10.1006/JCPH.1995.1151.

[30] A Ern and V Giovangigli, "Thermal diffusion effects in hydrogen-air and methane-air flames", Combust. Theor. Model. **2**, 349–372 (1998) 10.1088/1364-7830/2/4/001.

[31] A Ern and V Giovangigli, "Impact of detailed multicomponent transport on planar and counterflow hydrogen/air and methane/air flames", Combustion Science and Technology **149**, 157–181 (1999) 10.1080/00102209908952104.

[32] S Ambikasaran and K Narayanaswamy, "An accurate, fast, mathematically robust, universal, non-iterative algorithm for computing multi-component diffusion velocities", Proc. Combust. Inst. **36**, 507–515 (2017) 10.1016/j.proci.2016.05.055.

[33] O Desjardins, G Blanquart, G Balarac, and H Pitsch, "High order conservative finite difference scheme for variable density low Mach number turbulent flows", J. Comput. Phys. **227**, 7125–7159 (2008) 10.1016/j.jcp.2008.03.027.

[34] B Savard, Y Xuan, B Bobbitt, and G Blanquart, "A computationally-efficient, semi-implicit, iterative method for the time-integration of reacting flows with stiff chemistry", Journal of Computational Physics **295**, 740–769 (2015) 10.1016/j.jcp.2015.04.018.

[35] J Warnatz, "Calculation of the Structure of Laminar Flat Flames I: Flame Velocity of Freely Propagating Ozone Decomposition Flames", Berichte der Bunsengesellschaft für physikalische Chemie **82**, 193–200 (1978) 10.1002/bbpc.197800010.

[36] ME Coltrin, RJ Kee, and JA Miller, "A Mathematical Model of Silicon Chemical Vapor Deposition", Journal of The Electrochemical Society **133**, 1206 (1986) 10.1149/1.2108820.

[37] TP Coffee and JM Heimerl, "Transport algorithms for premixed, laminar steady-state flames", Combust. Flame **43**, 273–289 (1981) 10.1016/0010-2180(81)90027-4.

[38] J Warnatz, "Influence of transport models and boundary conditions on flame structure", in *Numerical methods in laminar flame propagation*, Vol. 6, edited by N Peters and J Warnatz, Notes on Numerical Fluid Mechanics (Vieweg+Teubner Verlag, Wiesbaden, 1982), pp. 87–111, 10.1007/978-3-663-14006-1_8.

[39] H Bongers and LPH De Goey, "The effect of simplified transport modeling on the burning velocity of laminar premixed flames", Combust. Sci. Technol. **175**, 1915–1928 (2003) 10.1080/713713111.

[40] Y Xin, W Liang, W Liu, T Lu, and CK Law, "A reduced multicomponent diffusion model", Combust. Flame **162**, 68–74 (2015).

[41] M Faghih, W Han, and Z Chen, "Effects of Soret diffusion on premixed flame propagation under engine-relevant conditions", Combustion and Flame **194**, 175–179 (2018) 10.1016/j.combustflame.2018.04.031.

[42] J De Charentenay and A Ern, "Multicomponent transport impact on turbulent premixed H_2/O_2 flames", Combust. Theor. Model. **6**, 439–462 (2002) 10.1088/1364-7830/6/3/304.

[43] SB Dworkin, MD Smooke, and V Giovangigli, "The impact of detailed multicomponent transport and thermal diffusion effects on soot formation in ethylene/air flames", Proceedings of the Combustion Institute **32**, 1165–1172 (2009) 10.1016/j.proci.2008.05.061.

[44] T Lu and CK Law, "Toward accommodating realistic fuel chemistry in large-scale computations", Progress in Energy and Combustion Science **35**, 192–215 (2009) 10.1016/j.pecs.2008.10.002.

[45] G Borghesi and J Bellan, "*A priori* and *a posteriori* investigations for developing large eddy simulations of multi-species turbulent mixing under high-pressure conditions", Phys. Fluids **27**, 035117 (2015) 10.1063/1.4916284.

[46] E Masi, J Bellan, KG Harstad, and NA Okong'o, "Multi-species turbulent mixing under supercritical-pressure conditions: modelling, direct numerical simulation and analysis revealing species spinodal decomposition", Journal of Fluid Mechanics **721**, 578–626 (2013) 10.1017/jfm.2013.70.

[47] CF Curtiss and JO Hirschfelder, "Transport properties of multicomponent gas mixtures", J. Chem. Phys. **17**, 550–555 (1949) 10.1063/1.1747319.

[48] JF Grcar, JB Bell, and MS Day, "The Soret effect in naturally propagating, premixed, lean, hydrogen-air flames", Proceedings of the Combustion Institute **32**, 1173–1180 (2009) 10.1016/j.proci.2008.06.075.

[49] J Schlup and G Blanquart, "A reduced thermal diffusion model for H and H_2", Combustion and Flame **191**, 1–8 (2018) 10.1016/j.combustflame.2017.12.022.

[50] R Kee, F Rupley, and J Miller, *Chemkin-II: a Fortran chemical kinetics package for the analysis of gas-phase chemical kinetics*, Sandia National Laboratories Report SAND89-8009, 1989.

[51] Y Xuan, G Blanquart, and ME Mueller, "Modeling curvature effects in diffusion flames using a laminar flamelet model", Combustion and Flame **161**, 1294–1309 (2014) 10.1016/j.combustflame.2013.10.028.

[52] Y Xuan and G Blanquart, "Effects of aromatic chemistry-turbulence interactions on soot formation in a turbulent non-premixed flame", Proceedings of the Combustion Institute **35**, 1911–1919 (2015) 10.1016/j.proci.2014.06.138.

[53] Y Xuan and G Blanquart, "Two-dimensional flow effects on soot formation in laminar premixed flames", Combustion and Flame **166**, 113–124 (2016) 10.1016/j.combustflame.2016.01.007.

[54] S Verma, Y Xuan, and G Blanquart, "An improved bounded semi-Lagrangian scheme for the turbulent transport of passive scalars", Journal of Computational Physics **272**, 1–22 (2014) 10.1016/j.jcp.2014.03.062.

[55] ME Mueller and H Pitsch, "LES model for sooting turbulent nonpremixed flames", Combustion and Flame **159**, 2166–2180 (2012) 10.1016/j.combustflame.2012.02.001.

[56] F Bisetti, G Blanquart, ME Mueller, and H Pitsch, "On the formation and early evolution of soot in turbulent nonpremixed flames", Combustion and Flame **159**, 317–335 (2012) 10.1016/j.combustflame.2011.05.021.

[57] B Savard and G Blanquart, "Broken reaction zone and differential diffusion effects in high Karlovitz n-C_7H_{16} premixed turbulent flames", Combustion and Flame **162**, 2020–2033 (2015) 10.1016/j.combustflame.2014.12.020.

[58] M Herrmann, G Blanquart, and V Raman, "Flux corrected finite volume scheme for preserving scalar boundedness in reacting large-eddy simulations", AIAA Journal **44**, 2879–2886 (2006) 10.2514/1.18235.

[59] C Pierce, "Progress-variable approach for large-eddy simulation of turbulent combustion", PhD thesis (Stanford University, 2001).

[60] L Shunn, F Ham, and P Moin, "Verification of variable-density flow solvers using manufactured solutions", Journal of Computational Physics **231**, 3801–3827 (2012) 10.1016/j.jcp.2012.01.027.

[61] RD Falgout and UM Yang, "hypre: A Library of High Performance Preconditioners", in *Computational science — iccs 2002*, edited by PMA Sloot, AG Hoekstra, CJK Tan, and JJ Dongarra (Springer, Berlin, Heidelberg, 2002), pp. 632–641, 10.1007/3-540-47789-6_66.

[62] HA van der Vorst, "Bi-CGSTAB: a fast and smoothly converging variant of bi-CG for the solution of nonsymmetric linear systems", SIAM Journal on Scientific and Statistical Computing **13**, 631–644 (1992) 10.1137/0913035.

[63] M Frigo and S Johnson, "The design and implementation of FFTW3", Proceedings of the IEEE **93**, 216–231 (2005) 10.1109/jproc.2004.840301.

[64] LF Richardson, "The approximate arithmetical solution by finite differences of physical problems involving differential equations, with an application to the stresses in a masonry dam", Philosophical Transactions of the Royal Society of London A: Mathematical, Physical and Engineering Sciences **210** (1911) 10.1098/rsta.1911.0009.

[65] F Perini, E Galligani, and RD Reitz, "A study of direct and Krylov iterative sparse solver techniques to approach linear scaling of the integration of chemical kinetics with detailed combustion mechanisms", Combustion and Flame **161**, 1180–1195 (2014) 10.1016/j.combustflame.2013.11.017.

[66] Z Hong, DF Davidson, and RK Hanson, "An improved H_2/O_2 mechanism based on recent shock tube/laser absorption measurements", Combust. Flame **158**, 633–644 (2011) 10.1016/j.combustflame.2010.10.002.

[67] KY Lam, DF Davidson, and RK Hanson, "A shock tube study of $H_2 + OH \rightarrow H_2O + H$ using OH laser absorption", International Journal of Chemical Kinetics **45**, 363–373 (2013) 10.1002/kin.20771.

[68] Z Hong, KY Lam, R Sur, S Wang, DF Davidson, and RK Hanson, "On the rate constants of $OH + HO_2$ and $HO_2 + HO_2$: a comprehensive study of H_2O_2 thermal decomposition using multi-species laser absorption", Proc. Combust. Inst. **34**, 565–571 (2013) 10.1016/j.proci.2012.06.108.

[69] DG Goodwin, H Moffat K., and RL Speth, *Cantera: an object-oriented software toolkit for chemical kinetics, thermodynamics, and transport processes*, 2017, 10.5281/zenodo.170284.

[70] S Lapointe, B Savard, and G Blanquart, "Differential diffusion effects, distributed burning, and local extinctions in high Karlovitz premixed flames", Combust. Flame **162**, 3341–3355 (2015) 10.1016/j.combustflame.2015.06.001.

[71] FA Williams, *Combustion theory* (Benjamin/Cummings, 1985).

[72] M Day, J Bell, P Bremer, V Pascucci, V Beckner, and M Lijewski, "Turbulence effects on cellular burning structures in lean premixed hydrogen flames", Combust. Flame **156**, 1035–1045 (2009) 10.1016/j.combustflame.2008.10.029.

[73] AJ Aspden, MS Day, and JB Bell, "Turbulence-flame interactions in lean premixed hydrogen: Transition to the distributed burning regime", J. Fluid Mech. **680**, 287–320 (2011) 10.1017/jfm.2011.164.

[74] A Aspden, M Day, and J Bell, "Turbulence-chemistry interaction in lean premixed hydrogen combustion", Proc. Combust. Inst. **35**, 1321–1329 (2015) 10.1016/j.proci.2014.08.012.

[75] G Blanquart and H Pitsch, "Thermochemical properties of polycyclic aromatic hydrocarbons (PAH) from g3mp2b3 calculations", The Journal of Physical Chemistry A **111**, 6510–6520 (2007) 10.1021/jp068579w.

[76] G Blanquart, P Pepiot-Desjardins, and H Pitsch, "Chemical mechanism for high temperature combustion of engine relevant fuels with emphasis on soot precursors", Combustion and Flame **156**, 588–607 (2009) 10.1016/j.combustflame.2008.12.007.

[77] K Narayanaswamy, G Blanquart, and H Pitsch, "A consistent chemical mechanism for oxidation of substituted aromatic species", Combust. Flame **157**, 1879–1898 (2010) 10.1016/j.combustflame.2010.07.009.

[78] Y He, B Cook, J Deslippe, B Friesen, R Gerber, R Hartman-Baker, A Koniges, T Kurth, S Leak, WS Yang, Z Zhao, E Baron, and P Hauschildt, "Preparing NERSC users for Cori, a Cray XC40 system with Intel many integrated cores", Concurrency and Computation: Practice and Experience **30**, e4291 (2017) 10.1002/cpe.4291.

[79] AJ Fillo, J Schlup, G Beardsell, G Blanquart, and KE Niemeyer, *Figures, plotting scripts, and data for "A fast, low-cost, and stable memory algorithm for implementing multicomponent transport in direct numerical simulations" [dataset]*, Zenodo, 2019, 10.5281/zenodo.3519910.

[80] AJ Fillo, J Schlup, G Beardsell, G Blanquart, and KE Niemeyer, *Direct numerical simulation results for turbulent hydrogen/air flame: multicomponent diffusion model [dataset]*, Oregon State University, 2019, 10.7267/2f75rf80s.

[81] AJ Fillo, J Schlup, G Beardsell, G Blanquart, and KE Niemeyer, *Direct numerical simulation results for turbulent hydrogen/air flame: mixture-averaged diffusion model [dataset]*, Oregon State University, 2019, 10.7267/c247f0072.

[82] AJ Fillo, J Schlup, G Beardsell, G Blanquart, and KE Niemeyer, *A fast, low-memory, and stable algorithm for implementing multicomponent transport in direct numerical simulations*, arXiv:1808.05463 [physics.flu-dyn], 2019.

[83] F Yang, C Law, C Sung, and H Zhang, "A mechanistic study of Soret diffusion in hydrogen–air flames", Combust. Flame **157**, 192–200 (2010) 10.1016/j.combustflame.2009.09.018.

[84] Y Xin, CJ Sung, and CK Law, "A mechanistic evaluation of Soret diffusion in heptane/air flames", Combust. Flame **159**, 2345–2351 (2012) 10.1016/j.combustflame.2012.03.005.

[85] B Savard, B Bobbitt, and G Blanquart, "Structure of a high Karlovitz n-C_7H_{16} premixed turbulent flame", Proc. Combust. Inst. **35**, 1377–1384 (2015) 10.1016/j.proci.2014.06.133.

[86] PE Hamlington, AY Poludnenko, and ES Oran, "Interactions between turbulence and flames in premixed reacting flows", Physics of Fluids **23**, 125111 (2011) 10.1063/1.3671736.

[87] N Chakraborty, I Konstantinou, and A Lipatnikov, "Effects of lewis number on vorticity and enstrophy transport in turbulent premixed flames", Physics of Fluids **28**, 015109 (2016) 10.1063/1.4939795.

[88] B Bobbitt, S Lapointe, and G Blanquart, "Vorticity transformation in high karlovitz number premixed flames", Phys. Fluids **28**, 015101 (2016) 10.1063/1.4937947.

[89] SH Kim and H Pitsch, "Scalar gradient and small-scale structure in turbulent premixed combustion", Physics of Fluids **19**, 115104 (2007) 10.1063/1.2784943.

[90] T Lu and CK Law, "Toward accommodating realistic fuel chemistry in large-scale computations", Progress in Energy and Combustion Science **35**, 192–215 (2009) 10.1016/j.pecs.2008.10.002.

[91] T Turányi and AS Tomlin, *Analysis of kinetic reaction mechanisms* (Springer Berlin Heidelberg, 2014), 10.1007/978-3-662-44562-4.

[92] KE Niemeyer and CJ Sung, "Reduced chemistry for a gasoline surrogate valid at engine-relevant conditions", Energy Fuels **29**, 1172–1185 (2015) 10.1021/ef5022126.

[93] R Hilbert, F Tap, H El-Rabii, and D Thévenin, "Impact of detailed chemistry and transport models on turbulent combustion simulations", Progress in Energy and Combustion Science **30**, 61–117 (2004) 10.1016/J.PECS.2003.10.001.

[94] S Lapointe, B Bobbitt, and G Blanquart, "Impact of chemistry models on flame–vortex interaction", Proceedings of the Combustion Institute **35**, 1033–1040 (2015) 10.1016/J.PROCI.2014.06.091.

[95] G Blanquart and H Pitsch, "Thermochemical Properties of Polycyclic Aromatic Hydrocarbons (PAH) from G3MP2B3 Calculations", (2007) 10.1021/JP068579W.

[96] J Towns, T Cockerill, M Dahan, I Foster, K Gaither, A Grimshaw, V Hazlewood, S Lathrop, D Lifka, GD Peterson, R Roskies, JR Scott, and N Wilkens-Diehr, "XSEDE: accelerating scientific discovery", Computing in Science & Engineering **16**, 62–74 (2014) 10.1109/mcse.2014.80.

[97] T Bajarin, "Maker Faire: Why the Maker Movement Is Important to America's Future", Time Magazine (2014).

[98] J Cummins, "Immersion Education for the Millennium : What We Have Learned from 30 Years of Research on Second Language Immersion", Second Katoh Gakuen International Symposium on Immersion and Bilingual Education **1**, 34–47 (1998).

[99] DA Muller, "Designing Effective Multimedia for Physics Education", PhD thesis (University of Sydney Australia, 2008).

[100] Corvallis-Benton County Public Library and AJ Fillo, *LIB LAB Library Laboratory Pilot Episode: make your own rocket & learn about propulsion*, https://youtu.be/H96Xr0Efelk, Mar. 2017.

[101] Corvallis-Benton County Public Library and AJ Fillo, *Lib Lab episode 2: solar eclipse*, https://youtu.be/yTN3BRoxY00, Apr. 2017.

[102] Corvallis-Benton County Public Library and AJ Fillo, *Lib Lab episode 3: soft robots*, https://youtu.be/WD69JmuNT7k, May 2017.

[103] Corvallis-Benton County Public Library and AJ Fillo, *Lib Lab episode 4: vortices*, https://youtu.be/0odYvE4k9Eg, June 2017.

[104] Corvallis-Benton County Public Library and AJ Fillo, *Lib Lab episode 5: 5 ways to watch the eclipse safely!*, https://youtu.be/oS6cxcqFGsw, Aug. 2017.

APPENDICES

Assessing the impact of chemical kinetic model reduction on premixed turbulent flame characteristics

Aaron J. Fillo and Kyle E. Niemeyer

Proceedings of the 2018 Spring Meeting of the Western States Section of the Combustion Institute
Bend, Oregon, USA. 26–27 March 2018.

Appendix A: Assessing the impact of chemical kinetic model reduction on premixed turbulent flame characteristics

A.1 Abstract

Using large, detailed chemical kinetic models in simulations of turbulent flames poses prohibitive computational expense, so typical approaches rely on reduction methods to generate reduced/skeletal models. Current best practice for the development of reduced models involves matching homogeneous ignition delay times, perfectly stirred reactor temperature response curves, and laminar burning parameters such as flame speed and thickness with predictions from the detailed chemical kinetic models. Prior studies using reduced models implicitly assume that matching the homogeneous and one-dimensional, steady laminar combustion behavior of the detailed model in a single-dimensional case will result in similar behavior for multi-dimensional laminar and turbulent simulations. However, this assumption has not been tested. Recent experimental studies demonstrated that real jet fuels with similar chemistry and laminar burning parameters exhibit different sensitivities to multi-dimensional effects such as flame stretch. This questions the validity of current best practices for developing reduced chemical kinetic models for turbulent flame simulations. This study will investigate the validity of using homogeneous and one-dimensional, steady phenomena to generate reduced models by comparing predictions of models at multiple levels of fidelity in three-dimensional DNS of premixed, turbulent, mid- to high-Karlovitz number flames. Combustion parameters will be compared between calculations using two reduced models from the CaltechMech model; these include flame speed, flame thickness, and conditional means of the fuel mass fraction and source term with respect to peak flame temperature. Reduced models will be generated using the directed relation graph with error propagation (DRGEP) method. Based on the results, we will make recommendations for the community.

A.2 Introduction

In this study we evaluate the impact of chemical kinetic model reduction on the premixed turbulent flame characteristics of simulated high-Karlovitz n-heptane/air flames. The motivation of this work is to asses the appropriateness of chemical kinetic model reduction for use in numerical simulation of turbulent reacting flows. Chemical kinetic model reduction is commonly used to reduce numerical expense and to facilitate three-dimensional turbulent simulations of these flows [90, 91]. Typically, model reductions are performed by sampling thermochemical state data in homogeneous, steady, and/or laminar combustion phenomena (e.g., autoignition, perfectly stirred reactor, one-dimensional laminar flame), and then evaluating model fidelity using the same [90, 92]. Occasionally, reduced models are further validated via comparison with experimental results, but generally reduced models are applied to more complex—and computationally expensive—problems such as turbulent combustion simulations, and the model fidelity is assumed to extend from that in simpler phenomena.

Several studies have examined the impact of chemical kinetic model reduction on small hydrocarbon and hydrogen flames [22, 25, 93]. Lapoint et al. [94] observed that changes in the chemistry model used in DNS simulations of turbulent premixed hydrogen/air flames could result in large discrepancies between simulations. Specifically, they observed that choice of reduced model could affect flame thickness. Differences in the flame thickness resulted in changes to local flame structure and interaction with large slow turbulence on the order on the flame front or greater; these discrepancies where larges when one-step chemistry was used, relative to the detailed model. Conversely, Luca et al. [25] demonstrated that reduced models of GRI-Mech 3.0 are appropriate for use in three-dimensional turbulent methane/air flames and negligibly impact the turbulent statistics relative to the original detailed model. Finally, as Hilbert et al. [93] reviewed, several studies have examined the impact of reduced chemistry in three-dimensional, unsteady turbulent phenomena such as ignition delay for n-heptane; but, to the authors' best knowledge, no detailed investigations have been performed on the impact or appropriateness of chemical kinetic model reduction for use in three-dimensional turbulent simulation of large-hydrocarbon flames. Thus, the ability of these chemical kinetic model reduction to properly simulate the turbulence-chemistry interactions present in practical flames may be limited.

This paper presents a preliminary investigation on the impact of chemical kinetic model reduction on the direct numerical simulation (DNS) of three-dimensional, premixed, high-Karlovitz n-heptane/air flames in the broadened reaction zone regime. We generated and investigated the performance of two reduced models from the 174-species, 1896-reaction CaltechMech model [75–77]. As a preliminary assessment of the impact of model reduction on turbulent flame characteristics the turbulent flame speeds and conditional means of the fuel mass fraction and source term as evaluated. This is done to asses the relative impact of these reductions on the turbulent-chemical interactions present in high-Karlovitz turbulent flames. The preliminary results indicate that relative error in the turbulent statistics is on the order of quantified error in ignition delay time and laminar flame speed; however, additional simulations are needed to confirm these results.

Here, we first describe the chemical kinetic model reductions used as the bases for comparison. We then present the numerical approach and governing equations, with a brief discussion of the three-dimensional flow configuration used. Finally, we present preliminary results evaluating the impact of these chemical kinetic model reductions on the accuracy of the turbulence characteristics of simulated premixed, high-Karlovitz, n-heptane/air flames.

A.3 Model reduction

The Model Automatic Reduction Software (MARS) package developed by Niemeyer et al. [16, 17, 24, 92] is used to reduce CaltechMech in this study. Here we used the directed relation graph with error propagation (DRGEP) reduction method, which has been described in detail in prior publications. DRGEP determines the importance of each species to the production/consumption of important, user-selected target species (in this case, we chose n-heptane, oxygen, and nitrogen; the latter was to prevent its removal). MARS automatically selects the cutoff threshold used to eliminate unimportant species (and their participating reactions) based on the The reduction used thermochemical state data sampled using the full, detailed kinetic model in homogeneous autoignition and perfectly stirred reactor simulations over initial temperatures of 800–1600 K, pressures of 1–20 atm, and equivalence ratios of 0.7–1.4. In addition, the error of candidate reduced models was based on comparison of predicted quantities over the same range of conditions with those of the detailed model.

For this investigation we generated two reduced chemical kinetic models from the 174 species, 1896 reaction CaltechMech [76, 77, 95], to maximum allowable errors of 1 % and 20 % in the ignition delay time and perfectly stirred reactor simulations. Figure A.1 presents the relative error in the ignition delay time and laminar flame speeds at 1 atm for both reduced models. The 1 %-error model has 76 species with 509 reactions and maximum errors of 0.5 % in the ignition delay time and 0.9 % in the laminar flame speed; alternatively, the 20 %-error model with 49 species and 233 reactions exhibits maximum errors of 10.6 % and 11.6 %, respectively.

A.4 Numerical approach

In this section, a description of the reacting flow equations is given. The three-dimensional flow configurations used is also presented.

A.4.1 Governing equations

The variable-density, low Mach number, reacting flow equations are solved using the finite-difference code NGA [33, 34]. The conservation equations are

$$\frac{\partial \rho}{\partial t} + \nabla \cdot (\rho \mathbf{u}) = 0 \,, \tag{A.1}$$

$$\frac{\partial \rho \mathbf{u}}{\partial t} + \nabla \cdot (\rho \ \mathbf{u} \otimes \mathbf{u}) = -\nabla p + \nabla \cdot \boldsymbol{\tau} + \mathbf{f} \,, \tag{A.2}$$

$$\frac{\partial \rho T}{\partial t} + \nabla \cdot (\rho \mathbf{u} T) = \nabla \cdot (\rho \alpha \nabla T) + \rho \dot{\omega}_T + \frac{\rho \alpha}{c_p} \nabla c_p \cdot \nabla T \,, \tag{A.3}$$

$$\frac{\partial \rho Y_i}{\partial t} + \nabla \cdot (\rho \mathbf{u} Y_i) = -\rho \dot{\omega}_i \,, \tag{A.4}$$

where ρ is the mixture density, $\mathbf{u}$ is the velocity, p is the hydrodynamic pressure, $\boldsymbol{\tau}$ is the viscous stress tensor, $\mathbf{f}$ represents volumetric forces, T is the temperature, α is the mixture thermal diffusivity, $c_{p,i}$ is the constant-pressure specific heat of species i, c_p is the constant-pressure specific heat of the mixture, and Y_i and $\dot{\omega}_i$ are the mass fraction and production rate of species i, respectively. In Eq. (A.3), the temperature source term

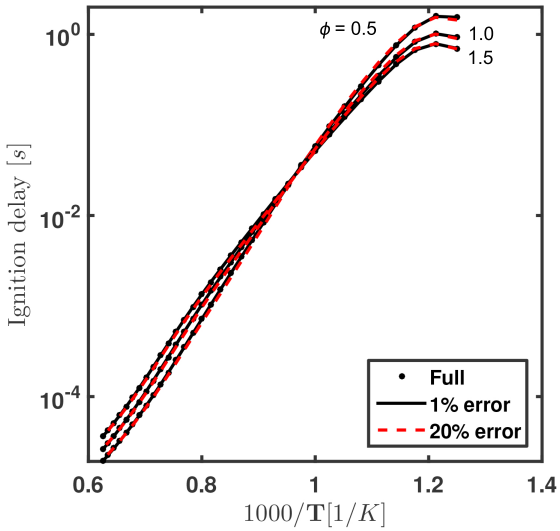

(a) Ignition delay

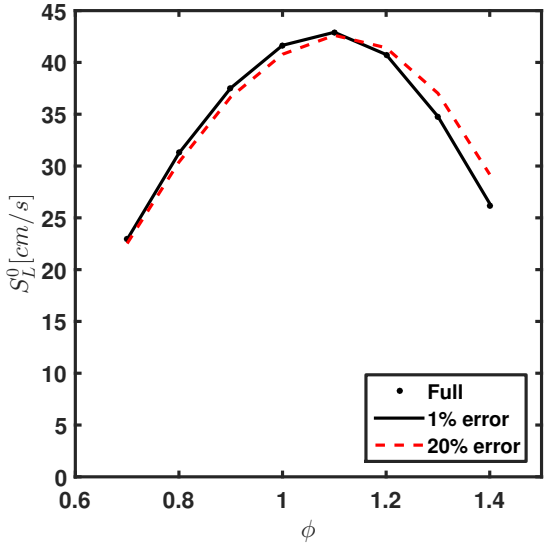

(b) Laminar flame speed

Figure A.1: Performance comparison of reduced n-heptane models with the detailed model for (a) ignition delay as a function of normalized temperature and (b) unstretched one-dimensional laminar flame speed as a function of equivalence ratio at 1 atm. The models perform similarly at 20 atm.

is given by

$$\dot{\omega}_T = -c_p^{-1} \sum_i h_i(T)\dot{\omega}_i \ , \tag{A.5}$$

where $h_i(T)$ is the specific enthalpy of species i as a function of temperature. The density is determined from the ideal gas equation of state.

A.4.2 Flow configuration

The three-dimensional flow configuration use in this work is a periodic domain in the y- and z- directions, and is used to study three-dimensional statistically stationary flames [18, 22, 23]. Both simulations discussed in this study are in the high-Karlovitz broadened reaction front regime. This configuration has been used in previous studies; only a brief overview is provided here.

Two reduced models for CaltechMech [76, 77, 95] are used in this study; both simulations use the same n-heptane/air mixture and three-dimensional configuration. The first model has a 0.5 % error in the laminar flame speed and ignition delay times relative to the full CaltechMech and contains 76 species and 509 reactions. The second model has a 10.6 % error in the laminar flame speed and ignition delay times and contains 49 species and 233 reactions.

The computational domain consists of inflow and convective outflow boundary conditions in the streamwise direction, with periodic boundaries in the two spanwise directions. An isotropic flow field provides a turbulent inflow condition, which we generated a priori using the canonical turbulence-in-a-box configuration. Each spanwise plane of the inflow corresponds to a time step for the inlet; to ensure that the flame front remains within the computational domain, the inflow velocity is scaled in situ to the mean turbulent flame speed. Since the flame mean turbulent flame speed is not known a priori, we used an approximate, user defined, flame speed based on previous n-heptane/air flame simulations. This allows the flame front to drift slightly within the domain but keeps the flame statistically stationary such that turbulent statistics can be collected over an arbitrarily long run time. Table A.1 also gives details of these computational domains. In the absence of mean shear, we use a linear turbulence forcing method [14, 15] to maintain the production of turbulent kinetic energy through the flame.

The unburnt temperatures and pressures for each case are 298 K and 1 atm, respec-

tively. The definitions of the Karlovitz number, Ka_u, and turbulent Reynolds number, Re_t, are also given in Table A.1, where $\tau_F = l_F/S_L$ is the flame time scale and $\tau_\eta = (\nu_u/\epsilon)^{1/2}$ is the Kolmogorov time scale of the incoming turbulence.

Table A.1: Parameters of the simulations. Δx is the grid spacing, η_u is Kolmogorov length scale in the unburnt gas, Δt is the simulation time step, ϕ is the equivalence ratio, T_{peak} is the temperature at peak fuel consumption rate in the one-dimensional laminar flame, S_L is the laminar flame speed, $l_F = (T_b - T_u) \,/\, |\nabla T|_{\mathrm{max}}$ is the laminar flame thickness, $l = u'^3/\epsilon$ is the integral length scale, u' is the turbulence fluctuations, ϵ is the turbulent energy dissipation rate, Ka_u is the Karlovitz number in the unburnt mixture, Re_t is the turbulent Reynolds number in the unburnt mixture, and ν_u is the unburnt kinematic viscosity.

	n-$\mathrm{C_7H_{16}}$ (1 %)	n-$\mathrm{C_7H_{16}}$ (20 %)
Domain	$11L \times L \times L$	
L	$128\Delta x$	
Grid	$1408 \times 128 \times 128$	
Δx [mm]	1.8×10^{-5}	
η_u [m]	9.0×10^{-6}	
Δt [s]	6×10^{-7}	
ϕ	0.9	
T_{peak} [K]	1270	
S_L [m/s]	0.375	0.367
l_F [mm]	0.383	0.395
l/l_F	1.12	1.09
u'/S_L	16.8	17.2
$\mathrm{Ka}_u = \tau_F/\tau_\eta$	202	213
$\mathrm{Re}_t = (u'l)/\nu_u$	190	

A.5 Results and Discussion

To assess the agreement between the two chemical model reductions, we performed two turbulent flame simulations using each model respectively. Simulations were performed using the Extreme Science and Engineering Discovery Environment (XSEDE) [96] Stampede resource at the Texas Advanced Computing Center (TACC); both cases were run across 1024 cores for 24 hours. For this analysis, the flames were allowed to develop in a

turbulent flow field, and statistics were computed after removing the initial transients of the input flow and scalar fields. Each simulation was run for at least 15 eddy turnover times ($\tau_{\text{eddy}} = k/\epsilon$, where k is the turbulent kinetic energy) to collect turbulent statistics. The a posteriori analysis presented here corresponds the last seven eddy turnover times. This is done to ensure the simulations have passed any initial transient behavior; due to this limited number of eddy turnover times, these results are only preliminary.

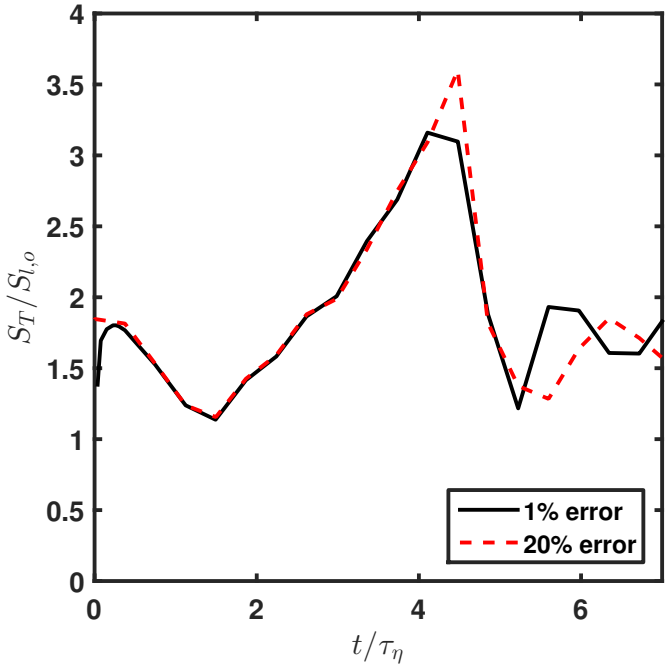

Figure A.2: Early time-history of the normalized turbulent flame speed from the turbulent hydrogen/air configuration for both diffusion models.

Figure A.2 shows the early time-history of the turbulent flame speed, S_T, calculated using

$$S_T = -\frac{\int_V \rho \dot{\omega}_{\text{F}} dV}{\rho_u Y_{\text{F},u} L} \,, \tag{A.6}$$

and normalized by S_L. The two simulations files were started with the same initial flame profile, and produce similar flame speeds to approximately 5 τ_{eddy} before diverging. Even after the models diverge, the two flame speeds oscillate around similar mean turbulent flame speeds of $\overline{S_T}/S_L \approx 1.848$ and 2.01 for the 1 % and 20 % reduction models, respec-

tively. However, since the turbulent flame speed will continue to develop for several eddy turnover times, this behavior should be interpreted as a preliminary result. A minimum of 25 τ_{eddy} is needed to draw any firm conclusions on the similarities of the turbulent flame speeds.

Figure A.3 presents the means of the fuel mass fractions and consumption rates, conditioned on temperature and normalized by their respective adiabatic flame temperatures of one-dimensional flames, T_{ad}. The calculated conditional means of the fuel mass fractions differ by negligible amounts, and the peak fuel consumption rates differ slightly (6.6%). For both simulations, the conditional means of the fuel mass fraction and source terms agree extremely well.

These three-dimensional turbulent flame results demonstrate that the calculated error in the ignition delay times and laminar flame speeds that occur from reduction of the chemical model do not notably impact the local quantities of the flame structure within the simulated high-Karlovitz number flames. In the simulated regime, turbulence is a smaller order than the flame thickness and as a result interacts the flame and broadens the reaction zone; it is interesting that the two models exhibit similar levels of agreement in the turbulent simulations compared with those in the laminar flame simulations. The community relies on evaluating the error of reduced models using homogeneous and steady, laminar phenomena, so these preliminary results are encouraging since they suggest that model agreement in turbulent flames may indeed be bounded by agreement in simpler phenomena. However, longer simulation times may result in these trends diverging, so the simulations need to be run longer to draw firm conclusions.

A.6 Summary

This article presents an a posteriori assessments of the impact of chemical kinetic model reduction on premixed three-dimensional, turbulent *n*-heptane/air flames. Small statistical differences were quantified in the turbulent flame speed and conditional mean of the normalized fuel source term as a function of normalized flame temperature. Based on the simulations presented here, these results suggest the impact of chemical kinetic model reduction on turbulent flame statistics is negligible for DNS of three-dimensional, premixed turbulent flames in a high-Karlovitz number regime. The level of fidelity of a reduced model determined with homogeneous and steady, laminar phenomena holds

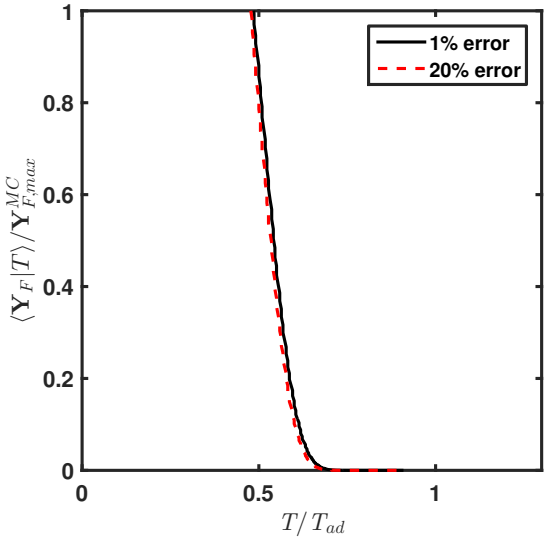

(a) Fuel mass fraction

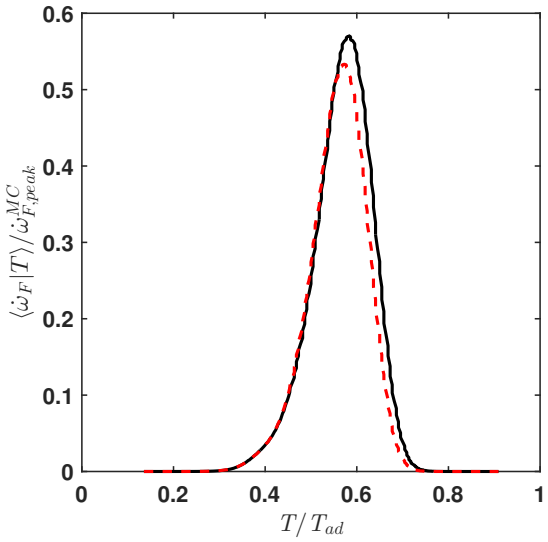

(b) Source term

Figure A.3: Turbulent flame structure for two reduced models of n-heptane, showing conditional means of (a) fuel mass fraction and (b) source term as functions of flame temperature normalized by T_{ad}. All plots are normalized by their peak multicomponent values from one-dimensional flat flames.

when extended outside those conditions to (steady) turbulent flames. However, these results are preliminary and not conclusive; longer simulations are needed to ensure the statistical significance of these results. For phenomena that are more sensitive to changes in chemistry, such as the unsteady turbulent ignition reviewed by Hilbert et al. [93], turbulence could exacerbate the differences between models of different fidelity, resulting in larger disagreement in turbulent statistics than predicted based on a priori model evaluations in simpler cases. Finally, additional simulations with different levels of turbulence are needed to fully evaluate the impact on chemical kinetic model reduction on the turbulence–chemistry interactions present in moderate-to-high Karlovitz number flames.

Acknowledgments

This material is based upon work supported by the National Science Foundation under Grant No. 1314109-DGE. This work used the Extreme Science and Engineering Discovery Environment (XSEDE), which is supported by National Science Foundation grant number ACI-1548562.

LIB LAB the Library Laboratory: hands-on multimedia science communication

Aaron J. Fillo and Kyle E. Niemeyer

Proceedings of the 2018 Spring Meeting of the Western States Section of the Combustion Institute
Bend, Oregon, USA. 26–27 March 2018.

Appendix B: LIB LAB the Library Laboratory: hands-on multimedia science communication

B.1 Abstract

Teaching scientific research topics to a K-12 audience in an engaging and meaningful way does not need to be hard; with the right insight and techniques it can be fun to encourage self-guided STEAM (science, technology, engineering, arts, and mathematics) exploration. LIB LAB, short for Library Laboratory, is an educational video series produced by Aaron J. Fillo at Oregon State University in partnership with the Corvallis–Benton County Public Library targeted at K-12 students. Each episode explores a variety of scientific fundamentals with playful experiments and demonstrations. The video lessons are developed using evidence-based practices such as dispelling misconceptions, and language immersion. Each video also includes directions for a related experiment that young viewers can conduct at home. In addition, science kits for these at-home experiments are distributed for free to students through the public library network in Benton County, Oregon. This talk will focus on the development of multimedia science education tools for communicating combustion fundamentals and several techniques that scientists can use to engage with a broad audience more effectively. Using examples from the LIB LAB YouTube Channel and collection of hands-on science demonstrations and take-home kits, this talk will present STEAM education in action.

B.2 Introduction

LIB LAB, short for Library Laboratory, is a hands-on multimedia educational video series focused on STEAM (science, technology, engineering, arts, and mathematics) communication. The focus on STEAM rather than STEM (science, technology, engineering, and mathematics) is a similar philosophy to the makers movement [97], which attempts to engage kids in scientific and engineering fields by highlighting their creative aspects. To accomplish this goal, LIB LAB utilizes hands-on experiments and demonstrations to

explore fundamental scientific principles. Every episode includes directions for a do-at-home science kit to enable viewers to follow along and explore on their own. Finally, to further break down barriers for engagement, free LIB LAB kits are distributed at the Corvallis–Benton County Public Library youth circulation desk.

B.3 Education Philosophy

To maximize educational impact, LIB LAB teaches through immersion, using hands-on experiments, and by dispelling common misconceptions. First, LIB LAB employs immersion teaching techniques commonly used in language education [98]. The philosophy is that science, technology, engineering, and mathematics are languages used to communicate complex ideas efficiently. Thus, every LIB LAB episode includes appropriate jargon and mathematical equations used in context, followed by a simple-English definition. This process of first using a word or equation in proper scientific context followed by a common language discussion provides viewers firsthand examples of the language in use, providing them the language skill necessary to ask follow-up questions and pursue further self-guided investigation.

Second, the do-at-home science kits included with every episode of LIB LAB enable viewers to interact with each lesson in person regardless of location. The kits are designed to cost around $1 and are made from common household objects to ensure accessibility and engagement for all viewers regardless of their socioeconomic background. These kits provide a component of ownership for viewers, increasing confidence in the material and facilitating further self-guided exploration at home.

Third, as highlighted by Derek Muller [99], dispelling common misconceptions can provide a safe, common ground to facilitate learning and retention. By first presenting a misconception and accepting it as a common and reasonable, if flawed, explanation, you acknowledge the viewers' understanding as a legitimate perspective. This acknowledgement demonstrates respect and empathy, helping the viewer to feel understood, which puts them in an emotional state conducive to learning retention and provides a safe foundation to teach the correct understanding of the misconception.

B.4 Episodes

There are currently six LIB LAB episodes available via YouTube, with an additional 10 LIB LAB Extras: shorter videos that investigate viewer questions and follow up ideas from previous episodes. These episodes cover a range of STEAM topics, including research topics from several of Oregon State University's current research labs. These episodes include:

- "LIB LAB Library Laboratory Pilot Episode: Make your own rocket & learn about propulsion" [100]: The Pilot episode of LIB LAB investigates the concepts of combustion chemistry, flame speeds, and propulsion. The associated kit is a small alka-seltzer rocket to provide a safe analog for chemical propulsion at home.

- "Lib Lab Episode 2: Solar Eclipse" [101]: Episode 2 explores the science of a total solar eclipse with directions on how to build a pinhole viewer to watch an eclipse safely.

- "Lib Lab Episode 3: Soft Robots" [102]: Episode 3 showcases the research of the Oregon State University Soft Robotics Lab and discusses the design of a soft robotic snake. The included science kit provides directions to build a simple soft-robot grabber.

- "Lib Lab Episode 4: Vortices" [103]: Episode 4 showcases a performance by the Oregon State University Drum-line and investigates the science of vortex rings with directions on how to construct a simple vortex shooter.

- "LIB LAB Episode 5: 5 ways to watch the Eclipse Safely!" [104]: Episode 5 presents direction on five ways to watch a total solar eclipse safely and encourages viewers to take time to experience the event first hand.

- "Explosive Fundamentals of Pressure" (LIB LAB/FYFD Crossover): The premier episode of LIB LAB season 2 is the start of a six-part collaboration produced in partnership with Nicole Sharp of FYFD[1]. This episode explores the fundamentals of pressure and the history of Blaise Pascal and includes direction on constructing a Cartesian diver. The episode concludes by recreating Pascal's famous barrel

[1] http://fyfluiddynamics.com

bursting experiment, and bursting a five-gallon glass carboy with gravitational head pressure.

- "Under Pressure at the Aquarium" (FYFD/LIBLAB Crossover): Part 2 of the LIB LAB/FYFD crossover, this episode examines pressure as a function of height by taking house hold items to the bottom of a 26-foot aquarium tank to show how they compress. This episode will be hosted on the FYFD channel.

B.5 Summary

This document presents an introduction to the YouTube STEAM education series LIB LAB, produced by Aaron J. Fillo. LIB LAB is a hands-on, demonstration-based multimedia education tool with accompanying do-at-home science kits. To ensure impact education and learning retention LIB LAB works to dispel misconceptions and teach through immersion to provide a safe and productive learning environment. Finally, LIB LAB is free and openly accessible through YouTube, which enables viewers from around the world to learn and engage with a variety of STEAM subjects in a comfortable, self-paced manner.

Acknowledgments

This material is based upon work supported by the National Science Foundation under Grant No. 1314109-DGE.

Appendix C: Method verification

To verify the method implementation, we generated an artificial species profile where the direction and relative magnitudes of the flux vectors could be predicted a priori to remain independent of any differential diffusion effects that may exist in a physical system. Specifically, we created a two-dimensional V-shaped species profile with a central angle of 45° and projected it into three dimensions as shown in Figure C.1a.

Such a profile results in flux vectors that are constant in the y-direction, are of equal magnitude and opposite sign in the z-direction reflected over the x-y-plane, and vary in magnitude but remain constant in sign matching the initial input profile in the x-direction. These predictions should be consistent independent of chemical species or other scalar value for the artificial input profile. We ran the algorithm for one "complete" set of sub-iterations to convergence and normalized the resulting diffusion flux vectors to ensure the relative magnitudes and direction were consistent with our expectations.

Figure C.1 shows the results of this artificial test case. The resulting normalized flux vectors agree with expectation and have equal magnitudes in the x- and z-directions corresponding to the 45° artificial flame angle. This result indicates proper functionality of the proposed method.

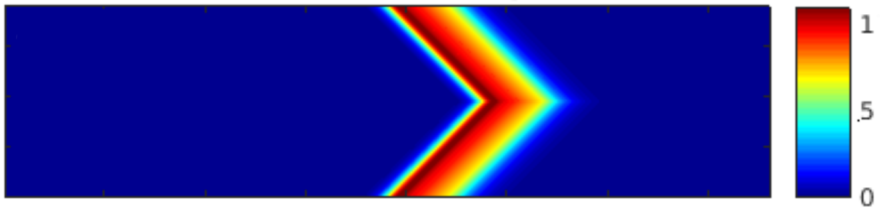

(a) Input species profile

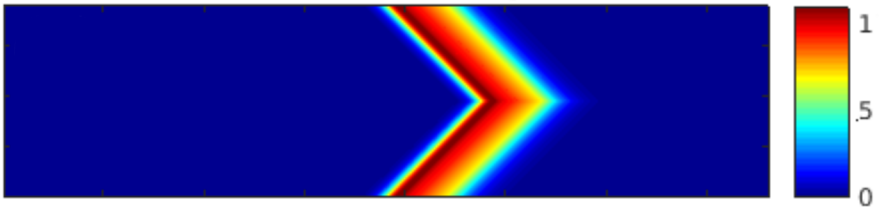

(b) x-component of mass flux

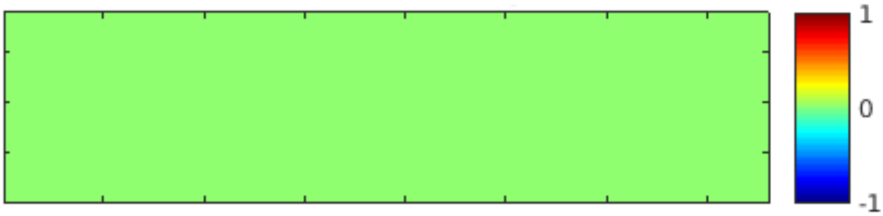

(c) y-component of mass flux

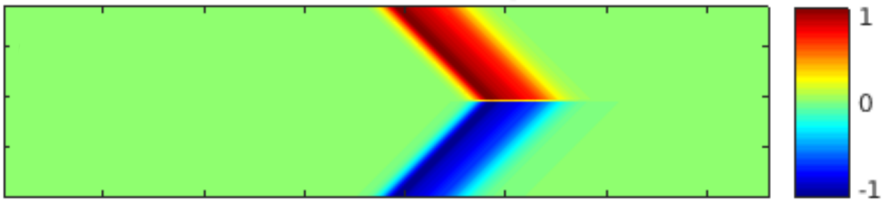

(d) z-component of mass flux

Figure C.1: Normalized flux vectors resulting from an artificial species profile after one full iteration of semi-implicit multicomponent diffusion calculation.